technische universität
dortmund

JÜLICH
Forschungszentrum

Ion Behavior Near Liquid/Solid Interface in Nanowire FET Biosensors

Vorgelegt in der Fakultät Physik der Technische Universität
Dortmund zur Erlangung des akademischen Grades eines Doktors
der Naturwissenschaften

Von

Master of Engineering

Yongqiang Zhang
aus Anhui, China

2025

Erstgutachter: Prof. Svetlana Vitusevich

Zweitgutachter: Prof. Ilya Akimov

Abgabedatum: 26. June 2025

Table of Contents

Contents

Abstract

This thesis analyzes valuable signals at the liquid/solid interface in nanosized transistor devices, which reflect the behavior of charge carriers and are promising for many useful and important biosensing applications. Advanced liquid gate-all-around (LGAA) silicon (Si) nanowire (NW) field-effect transistor (FET) biosensors were fabricated to study the effects at the liquid/solid interface in a liquid environment, including the charge inversion phenomenon, space-charge-limited-current (SCLC) effect, and the random telegraph signal (RTS) linked to single trap phenomena (STP) via transport and noise characterizations.

To study the charge inversion phenomena, noise spectroscopy, including an estimation of the dimensionless Hooge parameter (α_H) and equivalent input noise (S_U), was analyzed as effective indicators of ion behavior on the surface of the nanowire. The measurement results exhibited two distinct turning points at $MgCl_2$ concentrations of 10^{-4} M and 10^{-1} M for the peaks and valleys of α_H and S_U, respectively.

These two turning points effectively displayed the transformation trend caused by ion behavior in solutions with varying concentrations of $MgCl_2$. Interestingly, upon further investigation of the LGAA NW FET devices in 1 mM PBS at pH = 7.4, we revealed the SCLC effect. The linear relationship between drain current, I_{DS}, and drain voltage, V_{DS}, transforms to super linear behavior as the voltage increases, which reflects the formation of the SCLC effect. Additionally, time trace measurements revealed a two-level RTS phenomenon occurring within the voltage range where the SCLC effect was observed in the I-V characteristics.

This RTS, which is linked to STP, provides valuable insights into the SCLC effect in LGAA NW FETs. These discoveries are significant for the advancement of single-trap-based nanotransistor structures, particularly in the research field of biosensor applications. To study our hypothesis of enhancing the sensitivity of the FET biosensor, a gold bowtie antenna was fabricated on the nanowire surface. By carefully adjusting the light intensity, we induced single-center excitation and the RTS phenomenon without breaking down the dielectric layer. LGAA FETs with this antenna were tested under 940 nm LED excitation in 1 mM PBS at pH = 7.4. Our results show that the Lorentzian peaks in the noise spectra correspond to the occurrence of the RTS under illumination, with RTS fluctuations increasing in amplitude with higher infrared intensity.

These findings highlight the significant potential of the gold antenna for utilizing the plasmonic effect and RTS to boost biosensor sensitivity. The investigated signals at the liquid/solid interface coupled with the evolved FET device architecture thus underline a significant breakthrough in biosensor technology, setting the stage for the next era of highly sensitive bioelectronic sensors.

Zusammenfassung

In dieser Arbeit werden die wertvollen Signale an der Flüssigkeits-Festkörper-Grenzfläche in nanoskaligen Transistorbauelementen analysiert. Diese Signale spiegeln das Verhalten von Ladungsträgern wider und sind für viele nützliche und wichtige Biosensoranwendungen vielversprechend. Es wurden fortschrittliche Flüssigkeit-Gate-All-Around (LGAA) Silizium- (Si) Nanodraht- (NW) Feldeffekttransistor- (FET)-Biosensoren hergestellt, um die Effekte an der Flüssigkeits-Festkörper-Grenzfläche in einer flüssigen Umgebung zu untersuchen. Hierbei wurden das Ladungsinversionsphänomen, der raumladungsbegrenzte Strom-Effekt (SCLC-Effekt) und das zufällige Telegraphensignal (RTS), das zu einzelnen Fallenphänomenen (STP) verknüpft mittels Transport- und Rauschcharakterisierungen untersucht.

Zur Untersuchung der Ladungsinversionsphänomene wurde die Rauschspektroskopie, einschließlich der Schätzung des dimensionslosen Hooge-Parameters (α_H) und des äquivalenten Eingangsrauschens (S_U), als wirksame Indikatoren für das Ionenverhalten auf der Oberfläche des Nanodrahtes analysiert. Die Messergebnisse zeigten zwei deutliche Wendepunkte bei $MgCl_2$-Konzentrationen von 10^{-4} M und 10^{-1} M für die Spitzen und Täler von α_H bzw. S_U.

Diese beiden Wendepunkte zeigten effektiv den durch das Ionenverhalten in Lösungen mit unterschiedlichen $MgCl_2$-Konzentrationen verursachten Transformationstrend. Interessanterweise haben wir bei der weiteren Untersuchung der LGAA-NW-FET in 1 mM PBS bei pH = 7.4 den SCLC-Effekt entdeckt. Die lineare Beziehung zwischen Drain-Strom, I_{DS}, und Drain-Spannung, V_{DS},

verwandelt sich mit steigender Spannung in ein superlineares Verhalten, was die Entstehung des SCLC-Effekts widerspiegelt. Darüber hinaus ergaben Zeitspurenmessungen ein zweistufiges RTS-Phänomen, das in dem Spannungsbereich auftritt, in dem der SCLC-Effekt in den I-U-Kennlinien beobachtet wurde.

Dieses RTS, das mit STP verknüpft ist, liefert wertvolle Erkenntnisse über den SCLC-Effekt in LGAA-NW-FET. Diese Entdeckungen sind von Bedeutung für die Weiterentwicklung von Nanotransistorstrukturen auf der Basis von Einzelfallen, insbesondere im Forschungsbereich der Biosensorik. Zur Untersuchung unserer Hypothese, die Empfindlichkeit des FET-Biosensors zu erhöhen, wurde eine goldene Bowtie-Antenne auf der Oberfläche der Nanodrähte hergestellt. Durch sorgfältiges Einstellen der Lichtintensität konnten wir die Anregung eines einzelnen Zentrums und das RTS-Phänomen induzieren, ohne die dielektrische Schicht zu zerstören. LGAA-FET mit dieser Antenne wurden unter 940 nm LED-Anregung in 1 mM PBS bei pH = 7.4 getestet. Unsere Ergebnisse zeigen, dass die Lorentz-Peaks in den Rauschspektren dem Auftreten von RTS unter Beleuchtung entsprechen, wobei die Amplitude der RTS-Fluktuationen mit höherer Infrarot-Intensität zunimmt.

Diese Ergebnisse unterstreichen das erhebliche Potenzial der Goldantenne für die Nutzung des plasmonischen Effekts und des RTS zur Steigerung der Empfindlichkeit von Biosensoren. Die untersuchten Signale an der Flüssigkeits-Festkörper-Grenzfläche in Verbindung mit der weiterentwickelten FET-Bauelement-Architektur stellen einen bedeutenden Durchbruch in der Biosensorik dar und bilden die Grundlage für hochempfindliche bioelektronische Sensoren der nächsten Generation.

Acknowledgments

The time is so fast that four years abroad for my Ph.D. study plan is gradually approaching the end. During this period, I experienced a lot, and it will also be the most unforgettable aspect of my life. I am grateful to all people who provided me with advice and assistance along the way.

First, I would like to express my sincere gratitude to my scientific supervisor **Prof. Dr. Svetlana Vitusevich** for giving me the opportunity to study in her group. She, with her profound knowledge and experience, is always patient and answers the questions I encounter tirelessly. I feel happy that I can continue my research topic in her teamIn addition, I would like to thank **Prof. Dr. Andreas Offenhäusser** Institutsleiter at the **Institute of Biological Information (IBI-3)**, who created a conducive atmosphere for our research endeavors. I enjoyed working with you.

I would like to express my sincere gratitude to **Prof. Dr. Ilya Akimov** for his academic guidance and invaluable support, which have been instrumental in the successful completion of my doctoral dissertation. Additionally, his insightful feedback and generous help have greatly contributed to the quality and progress of my research.

Dr. Mykhailo Petrychuk is the person surrounding me who is closest to the 'Nobel Prize' in my mind. Whenever I discuss the data with him, he never fails to impress me with his insights into noise analysis, deriving formulas, and establishing physical models. In addition, I am grateful to the technical staff of **the Helmholtz Nano Facility (HNF)** of **Forschungszentrum Jülich** for their assistance with biosensor fabrication.

I am also grateful to all my colleagues and group members for their friendliness and support. In particular, I would like to thank **Denys Pustovyi** for selfless and assistance during daily experiments. In my eyes, **Dr. Nazarii Boichuk** is both a colleague and a ‘teacher’ who always patiently discusses experimental plans, parameters, and analyzes and summarizes experimental data with me. I learned a lot from you. In particular, thanks my reliable colleagues **Dr. Zhi Jiang**, **Dr. Kai Li**, **Dr. Yangyan Guo**, **Dr. Dmytro Zhulai**, **Valeriia Chekubasheva**, and **Hanlin Long** for being always selfless supportive and warm hard ready to put in a good amount of hard work.

I sincerely thank my good friend **Che Leng** for his valuable support in facilitating the progress of my doctoral dissertation.

I am also very grateful for receiving a research grant (No. 202108360085) from the China Scholarship Council (CSC). The CSC funding covers my daily living costs to support me in finishing my Ph.D.

Finally, I would like to express my gratitude to my family members for their silent dedication and support behind the scenes, helping me complete my doctoral journey. In conclusion, these words do not fully convey my profound gratitude. I will never forget grateful to the people who helped me.

1.1 Motivation and background

1. Introduction

1.1 Motivation and background

As science and technology continue to advance, there is a growing need to explore the unknown, both in our immediate surroundings and the wider world. Fortunately, various sensors are available to assist in sensing and recording environmental changes across all domains. For instance, electrical sensors can convert stimuli into signals that can then be processed by computers to derive meaningful and actionable insights. Temperature sensors play a crucial role in monitoring changes in the surrounding temperature and offer valuable information about environmental conditions or bodily changes. Similarly, light sensors serve as vital components in light-sensitive switches, enabling the control of lighting devices based on the ambient light levels. Biosensors are designed to detect specific receptors using biomolecules as target chemicals, which holds significant promise for disease prevention and detection efforts. Many machines and equipment rely heavily on various sensors for normal operation. In other words, advancements in sensor technology can not only improve the efficiency and quality of daily life, but also enhance productivity and enable more accurate forecasting capabilities.

Advances in nanoscience and nanotechnology have unlocked the potential for nanosized systems to execute a wide array of tasks, spanning electrical, biological, chemical, and beyond. As structures shrink to the nanometer scale, they exhibit markedly different properties compared to their macroscopic counterparts, opening new avenues for exploration. Among the diverse range of nanomaterial structures, silicon nanowires (NWs) are highly functional entities characterized by their unique one-dimensional properties. In particular, the conductivity of nanowires can be modulated by the presence of biochemical substances adsorbed on their surfaces.

This unique attribute has spurred the development of nanostructured devices with enhanced sensing capabilities by leveraging the distinctive properties of nanowires. Through the precise manipulation and engineering of nanowire-based structures, novel sensing platforms with improved sensitivity and selectivity have been realized, promising advancements in various fields of application.

Nanowire structures have found applications in various domains, including environmental monitoring, industrial processes, and medical diagnostics. By integrating nanowires into testing devices, the sensitivity to target analytes is significantly enhanced. Biosensors offer numerous advantages, such as rapid response, compact size, high sensitivity, portability, and a high signal-to-noise ratio. Moreover, for effective detection of biological and chemical molecules, biosensors should demonstrate outstanding sensitivity, label-free detection capability, and real-time response. Nanowire-based devices fulfill these criteria and have been deployed in diverse sensing applications ranging from gas detection to biological and light sensing. As researchers continue to explore this burgeoning field, sensors are poised to offer even greater promise in the future, with advancements likely to expand their capabilities and applications further.

1.2 Fundamentals of liquid-gate (LG) field effect transistors (FETs)

A conventional metal oxide semiconductor field effect transistor (MOSFET) is controlled by applying a gate voltage, leading to the change the current flows of the nanowire channel at definite applied drain-source voltage. Typically, the channel possesses the opposite charge carriers to the main doping atom charge and in working state so colled inversion layer is formed. When the MOSFET device is in an open state, the carriers in the inversion layer accumulate predominantly at the surface of the channel. Figure 1.1 illustrates a schematic of MOSFET devices for both P-type and N-type nanowire.

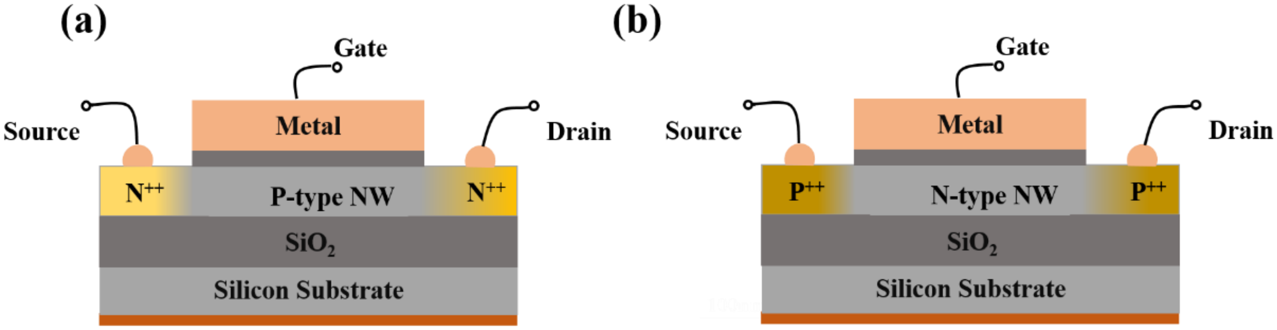

Figure 1.1 Schematic representation of MOSFET for (a) P-type NW and (b) N-type NW.

In this thesis, we focus on an ion-sensitive field effect transistor (ISFET) controlled using a liquid gate. The ISFET and MOSFET operate in a similar way, with the distinction that the ISFET requires the use of an electrolyte solution instead of a metal gate. In our group, the two main channel configurations with different doping concentrations are N^{++}-P-N^{++} and P^{++}-P-P^{++}, as shown in Figure 1.2. In the case of the ISFET, the liquid gate is controlled by applying a bias to the AgCl/Ag reference electrode immersed in a bioliquid solution. In addition, ISFET devices can be also controlled by a back gate by bias applied to the substrate, which serves as in a function of the back-gate electrode.

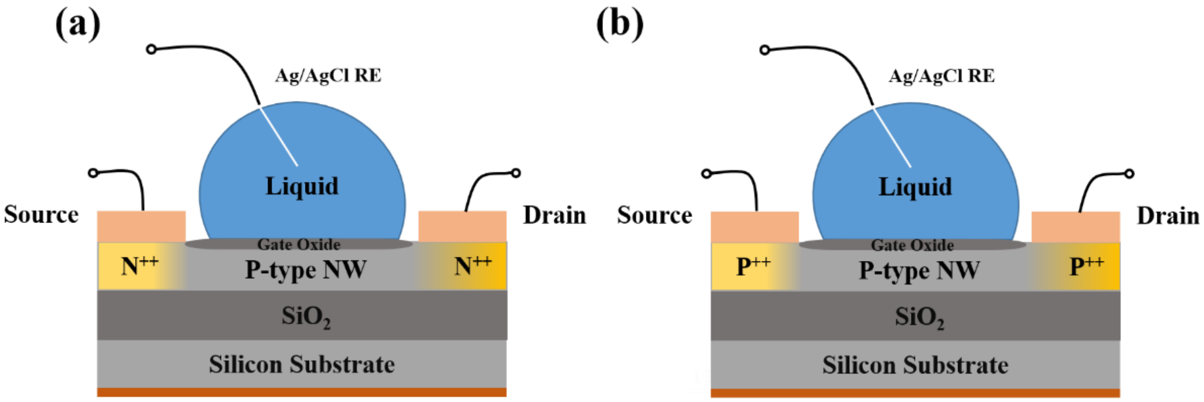

Figure 1.2 Schematic representation of nanowire (NW) ISFETs of (a) N^{++}-P-N^{++} NW and (b) P^{++}- P- P^{++} types of conductivity in NW channels.

Figure 1.3 shows the traditional dependence of the drain source current (I_{DS}) on the liquid gate voltage (V_{LG}) and drain source voltage (V_{DS}), which are called transfer and output curves, respectively. To avoid leakage currents, a 20 nm SiO_2 oxide layer was used to cover the surface of the nanowire, enabling the operation nanowire channel in a liquid without leakage current during current flow of I_{DS} from the drain to the source. Simultaneously, the active sensing area of the ISFET device is defined by the gate oxide SiO_2 layer, which is exposed to the liquid during detection.

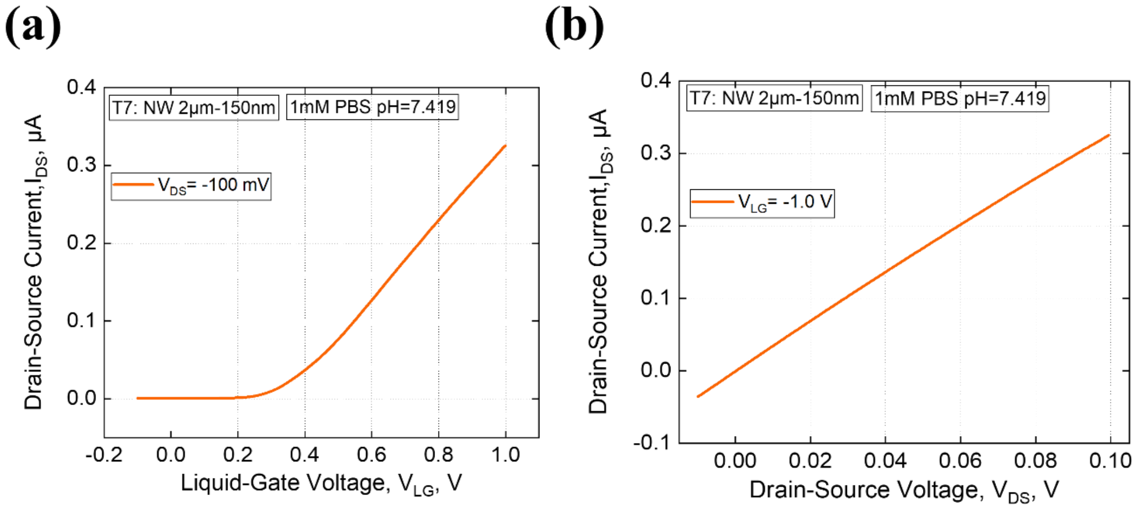

Figure 1.3 (a) Typical transfer characteristics of I_{DS}-V_{LG} for a nanowire FET with a PBS solution of 1 mM pH = 7.4 at V_{DS} = -100 mV. (b) The traditional output curve of I_{DS}-V_{DS} is observed for a FET device with a PBS solution of 1 mM pH = 7.4 at V_{DS} = -1.0 V.

During the measurements, the surface of the 20 nm dielectric oxide layer was activated to excite negatively charged hydroxyl groups (OH^-). It is important to note that when the dielectric layer surface comes into contact with the tested solution of definite pH, the surface charge changes through a protonation/deprotonation process involving surface groups.[1] These alterations significantly affect the flow of charge carriers in the channel owing to modifications in the surface potential distribution. This phenomenon holds significant importance for every ISFET device, as it is directly related to the electrostatic control field effect and the operational principle of FET-based devices. Bergveld and colleagues first discovered and discussed this effect in the 1970s.[1] Since then, the ISFET device has emerged as one of the most valuable electronic sensors capable of capturing useful electrical signals from chemical reactions through the electrostatic control field effect.

This thesis represent results of studies of liquid-gate nanowire FET biosensors with p-type channel conductivity: P^{++}-P-P^{++}, similar to the conventional ISFET. [2-4] The liquid-gated FETs offer the advantage of efficiently converting biochemical reactions near the liquid/solid interface into measurable and valuable electronic signals for further analysis. This efficiency is attributed to the high surface-to-volume ratio and nano size of the nanowires, which facilitate the rapid accumulation/depletion of charge carriers. A specialized surface functionalization process was employed to coat the nanowire with analyte receptor molecules, ensuring precise selectivity and high sensitivity to the target-tested biomolecules. Figure 1.4 illustrates the schematic structure of a liquid-gate transistor covered with a specially functionalized receptor layer, so called recognition layer for the precise and selective detection of target biomolecules. Typically, proteins, DNA, and antigens can serve as target molecules dissolved in the tested solution. When a charged molecule covalently binds to the corresponding receptor attached to the surface of the gate oxide layer, it initiates a biomolecular recognition reaction, resulting in a change in the surface potential.[5] This alteration in the surface potential influences the charge-transport properties of the biosensor. Indeed, the change in the surface potential varies based on the concentration of charged target biomolecules in the electrolyte solution, and this change can be measured. Consequently, almost all FET-based devices adhere to the sensing principle, with detailed information regarding the detection process provided to highlight the recognition of receptors and target-charged biomolecules.

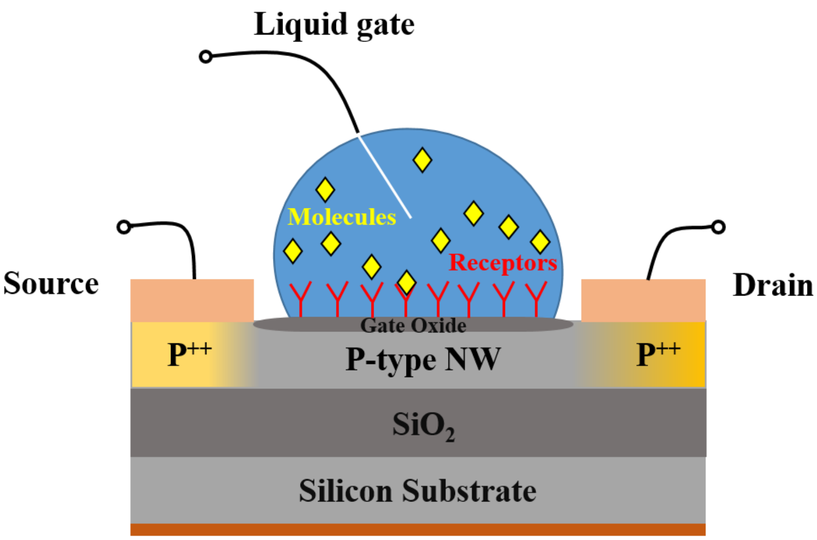

Figure 1.4 Schematic structure of the biosensor device. On the top surface of the 20 nm SiO_2 gate oxide layer, a functionalization layer was applied to attach receptors to the solid surface in a liquid for selective binding of the tested molecules.

Up to now, the advantageous technology of FET-based devices has been used in a wide range of applications including pH measurements [2, 6] and ion sensing measurements,[2, 3, 6] and even more in various biological events such as antigen-antibody binding,[7-9] protein-protein interaction,[10, 11] enzyme-substrate reaction, [10, 12] and genome sequencing.[13] It is worth mentioning that operating and sensing of biosensors in solution still pose challenges. In particular, the tested ions or valuable charged species that exist in physiological fluids, including blood, saliva, and sweat, often limit the response of biosensors to the analyte. These charged species act as electrical screens, reducing the sensitivity of the biosensors during detection. [8, 14, 15] In fact, only the charged molecules located within the electrical double layer can be successfully tested using a transistor. In other words, for reliable and effective sensing results with high sensitivity, it is preferable for the receptor molecules on the surface of the nano-channel to not exceed the Debye screening length when binding target molecules.[9] Thus, in order to fabricate FET biosensors with high properties, the optimization process of the recognition layer should be carefully considered. Usually, the approach is to optimize the surface structure of the recognition layer, which includes selecting shorter receptors and modifying linker molecules.[16] In our group, we applied aptamers- short single-stranded DNAs (ssDNA) as a recognition layer to enhance the properties of the biosensor, enabling precise selectivity and high sensitivity for target charged molecules such as cardiac troponin proteins (cTnl) and amyloid-beta 40 (Aβ 40). [17, 18] Meanwhile, the 20 nm SiO_2 gate oxide layer of the biosensor can ensure the stable immobilization of aptamers on the surface using a chemical functionalization protocol. However, an optimized surface structure of the recognition layer helps to reduce unnecessary specific binding and enhances charge transfer between the biosensor and the target analyte, leading to improved properties and sensitivity of FET devices with enhanced selectivity. At the same time, the charge transfer process during the measurements still strongly relies on the intrinsic electrical performance of biosensors. In fact, the noise characteristics of the transistor play a crucial role in determining the sensitivity of biosensors to detect the smallest change in signal in analyte concentrations. Therefore, as discussed in later sections of this thesis, noise spectroscopy serves as a valuable method to characterize the ion behavior at the solid-liquid interface and improve the sensitivity of biosensors during detection. Furthermore, the promising performance of FET devices is significant for clinical diagnosis and human health monitoring.

Generally, the biosensor mechanism resembles that of a conventional MOSFET device and can be elucidated using energy-band diagrams, as depicted in Figure 1.5. This figure illustrates four distinct cases: accumulation, flat-band, depletion, and inversion. In this context, the energy band schematic delineates the variation in the electron energy with respect to its position. Each energy-band diagram in Figure 1.5 comprises four distinct energy levels: conduction band (E_C), intrinsic energy band (E_i), Fermi energy (E_F), and valence band (E_V). Notably, the region between the top of the conduction band and the bottom of the valence band is known as the forbidden band (E_G), where no permissible states exist for electrons. At absolute zero temperature, all electrons are confined to the lowest energy state. Moreover, under absolute zero-temperature conditions, the Fermi level represents the maximum energy level that electrons can occupy. However, in intrinsic semiconductors, E_F aligns with E_i and both are positioned in the middle of the forbidden gap. Consequently, electrons transition from the valence band to the conduction band owing to the random thermal motion of atoms under non-zero absolute temperature conditions. In an ideal scenario, assuming a uniform material and neglecting the difference in work function between the metal and semiconductor, E_C and E_V are flat, and the Fermi level remains constant throughout the system when no bias is applied to the gate. Thus, the surface potential signifies the total voltage drop across the semiconductor structure, which is zero in this instance, as illustrated in Figure 1.5 (b). This scenario is defined as the "flat band voltage" mode.

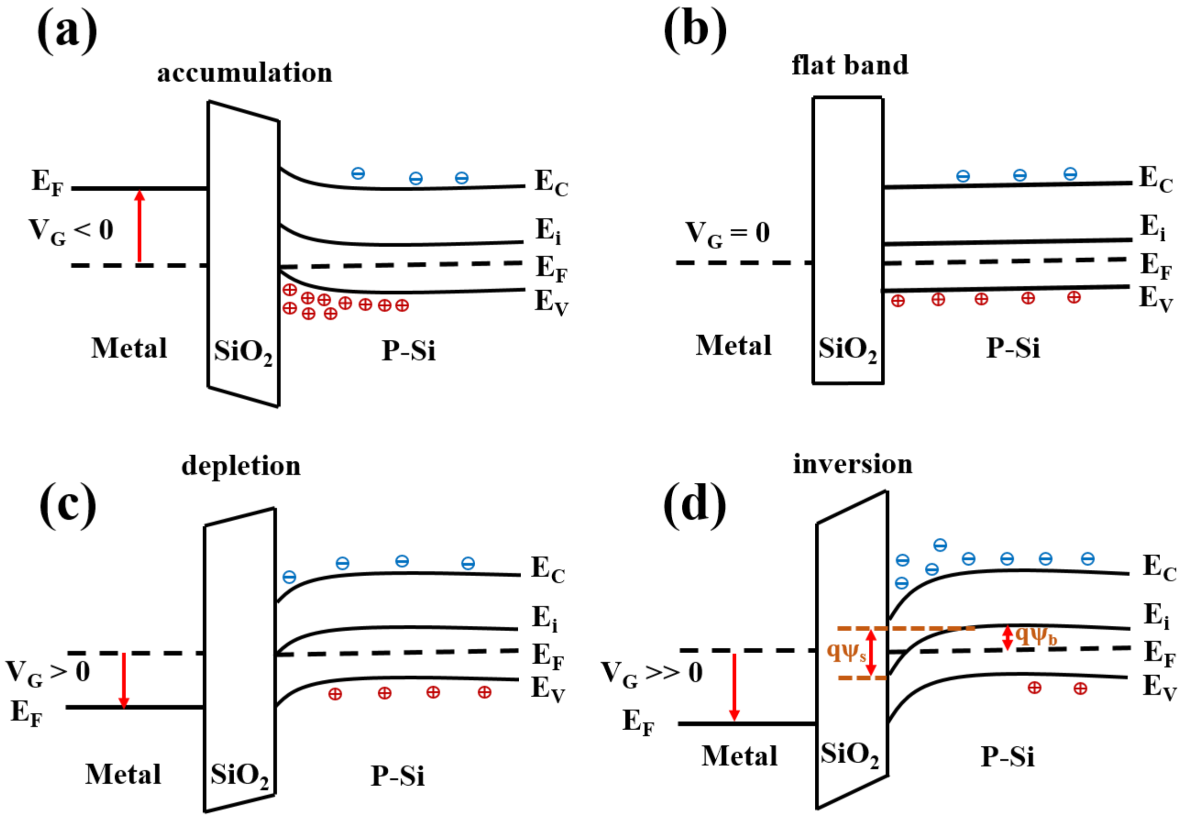

Figure 1.5 Schematic of the energy band of a classic P-type MOS structure with a metal gate under different voltages: (a) accumulation mode, (b) flat band voltage mode, (c) depletion mode, and (d) inversion mode.

To elucidate the detection process with a P-type structure, wherein the majority of carriers are holes, it is notable that these holes accumulate near the interface between the semiconductor and insulator when a negative voltage is applied to the gate electrode. Concurrently, the increased concentration of holes at the Si/SiO$_2$ interface causes the E_V to bend upward towards the E_F. This operational principle explains the functioning of all P-type conductive FET devices in the accumulation mode. In simpler terms, when a positive voltage is applied to the gate of a P-type structure, the holes are repelled from the interface, resulting in a phenomenon known as depletion. As illustrated in Figure 1.5 (c), downward bending of energy near the interface occurs, primarily influenced by the negatively charged acceptor impurities, leading to a space charge primarily consisting of holes.

Meanwhile, owing to the downward bending of the energy bands, the concentration of electrons gradually increased at the interface. However, with the continued increase in the positive bias applied to the gate, the bending of the energy bands becomes more pronounced, resulting in a higher concentration of electrons compared to the concentration of holes at the SiO_2/Si interface. In this inversion mode, as depicted in Figure 1.5 (d), the number of electrons at the interface exceeds the number of holes, making them the majority carriers, which is similar to the behavior of an N-type semiconductor. Remarkably, good agreement with the operational principle was observed when a P-type transistor device exhibited N-type conductivity in the inversion regime. Mathematical equation (1.1) is commonly employed to describe the inversion mode.[19]

$$\psi_s = 2\psi_b \tag{1.1}$$

where ψ_b represents the difference between the intrinsic Fermi level (E_i) in the bulk and the real Fermi level (E_F) of the doped semiconductor, ψ_s is the surface potential.

$$\psi_b = \frac{KT}{q} \ln\left(\frac{N_A}{n_i}\right) \tag{1.2}$$

where K, T, and q are Boltzmann constant, absolute temperature, and elementary charge, respectively. Meanwhile, the n_i represents the intrinsic carrier density in a semiconductor. And the N_A is the density of the acceptors in a P-type structure. Hence, optimizing the inversion regime is an effective way to achieve different doping levels using FET devices.

Equations (1.3) and (1.4) indicate the relationship between the hole concentration and surface potential, as well as the electron concentration as a function of the surface potential, respectively.

$$p_s = N_A \cdot e^{-\frac{q\psi_s}{KT}} \tag{1.3}$$

and

$$n_s = \frac{n_i^2}{p_s} = n_{p0} \cdot e^{-\frac{q\psi_s}{KT}} \tag{1.4}$$

where n_{p0} represents the equilibrium concentration of the minority carriers in the bulk and ψ_s represents the surface potential.

The relationship between ψ_s and the gate voltage (V_G) is given by the formula (1.5).

$$V_G = \psi_s + V_{ox} \tag{1.5}$$

where V_{ox} is the potential drop across the gate oxide layer. The value of the applied V_G is one of the key parameters for changing the concentration of charge carriers and the conductivity of the nanochannel. Therefore, considering the previously described MOSFET structure diagram, equation (1.6) is derived to describe I_{DS} in three different operational regimes corresponding to various ranges of V_G.

$$I_{DS} = \begin{cases} 0, & V_G \le V_{TH}; \\ C_{ox}\mu\frac{W}{L}\left[(V_G - V_{TH})V_{DS} - \frac{1}{2}V_{DS}^2\right], & V_G > V_{TH}, V_{DS} \le V_G - V_{TH}; \\ \frac{1}{2}C_{ox}\mu\frac{W}{L}(V_G - V_{TH})^2[1 + \lambda(V_{DS} - V_{DSsat})], & V_G > V_{TH}, V_{DS} > V_G - V_{TH}. \end{cases} \tag{1.6}$$

where W and L are the width and length of the nanowires, respectively. V_{TH}, also known as the threshold voltage, is an initial value of V_G that enables I_{DS} to flow through the nanochannel. where μ is electron mobility. λ represents the channel-length modulation parameter. V_{DSsat} is V_{DS} under the saturation condition. Meanwhile, the C_{ox} represents the unit area capacitance of the gate-oxide layer in a MOSFET device, and its calculation formula (1.7) is as follows：

$$C_{ox} = \frac{\epsilon_0 \epsilon_{ox}}{t_{ox}} \tag{1.7}$$

where ϵ_0 and ϵ_{ox} are the permittivity of vacuum and the dielectric oxide, respectively. t_{ox} is the thickness of the gate oxide layer in the FET structure.

Based on the classical transfer curve depicted in Figure 1.3 (a) and current formula (1.6), it is apparent that the FET device operates in three distinct gate voltage regimes. The first regime occurs when the gate voltage (V_G) is less than the threshold voltage (V_{TH}), and is denoted as $V_G < V_{TH}$. In this regime, the conductive nano-channel between the drain and source of the transistor has not yet been formed, resulting in what is commonly referred to as the "off-state." The second regime occurred when V_G was greater than V_{TH}, as indicated by $V_G > V_{TH}$. In this scenario, the drain and source are effectively connected through the nanochannel, leading to a rapid increase in the current as the gate voltage is increased. The final regime occurs when V_G is significantly larger than V_{TH}. In this case, the behavior of the transistor resembles that of a regular resistor, wherein the drain-source current (I_{DS}) increases linearly with increasing V_G.

The interaction between surfaces and various liquids is crucial in the field of bioelectronics, as it determines the fundamental properties of interaction processes.When an object comes into contact with a fluid, an electrical double layer is established at the interface between the two materials. For example, the object may be represented by a surface composed of a metal electrode or a nanowire coated with a dielectric material.The electrical double layer (EDL) denotes the spatial separation of charge at the interface between two phases. The generation of charge on a solid surface may result from ion absorption on the surface, dissociation of surface compounds, or redistribution of electron density. The EDL is formed at the interface between a solid substrate and an electrolyte in the context of biosensors (see Figure 1.6).

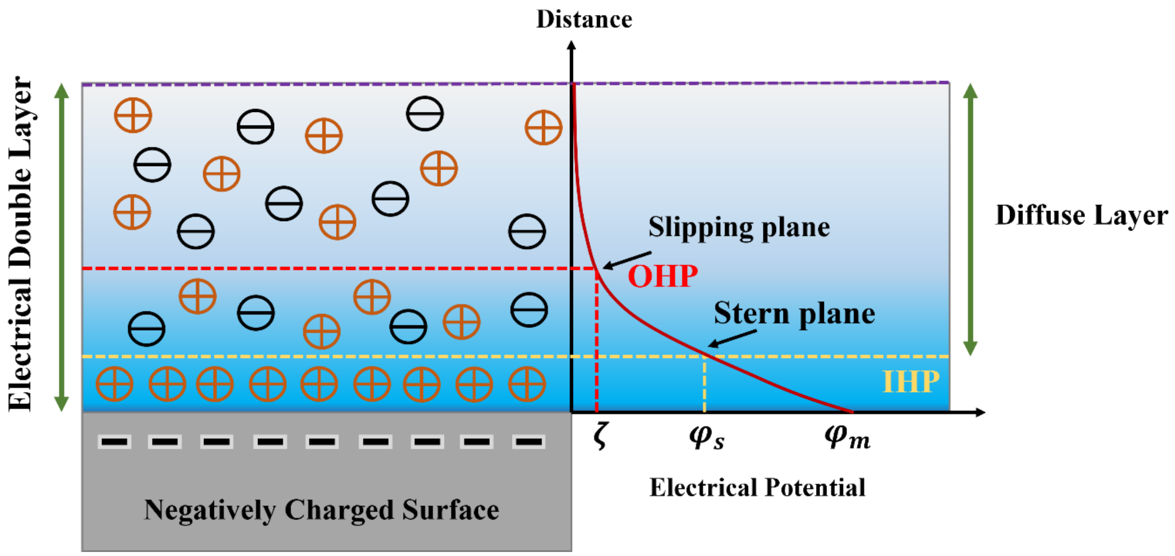

Figure 1.6 When a liquid comes into contact with a solid surface, charge redistribution occurs within the liquid, leading to the formation of an electrical double layer, characterized by spatially separated charges of opposite signs. Ions adsorbed onto the surface form a rigid Stern layer, within which the potential decreases linearly, analogous to the behavior observed in a parallel plate capacitor. The slipping plane delineates mobile ions from those affixed to the surface. Due to an excess of positive charge, the potential within this plane decreases to what is referred to as the ζ potential. In the diffuse layer, ion concentration adheres to the Boltzmann distribution, resulting in an exponential decrease in potential. Conversely, in the bulk liquid, ions are uniformly distributed.

In this configuration, the adsorption of ions of a specific type and charge is more advantageous. These ions are referred to as "potential determining ions" because they are directly bonded to the surface and consequently determine its charge. The layer of absorbed co-ions is characterized by a high density and maintains a constant thickness comparable to the radius of an atom. The presence of charges on the solid surface at the interface with a liquid generates an electrical potential, which can be determined using the Nernst equation:

$$\varphi = \frac{RT}{Fz} \ln \frac{\alpha(\text{surface})}{\alpha(\text{solution})} \tag{1.8}$$

where F is the Faraday constant, z is the ion charge, T is the temperature, R is the universal gas constant, and α(surface) and α(solution) refer to the ion activities adjacent to the surface and within the bulk fluid, respectively. The activity of ions can be expressed in relation to their physical concentration, C(ion), as α(ion) = γ(ion)C(ion), where γ(ion) represents the activity coefficient of a specific ion type. At low concentrations, the activity coefficient approaches unity, allowing it to be substituted with simple concentration values. The charged surface exerts electrostatic forces that attract ions of the opposite charge from the solution. These ions are referred to as "counter ions." The system's configuration resembles that of a parallel plate capacitor and has been generalized within the framework of the Helmholtz model. The surface charge is counterbalanced by the counter ions, which are positioned at a distance from the surface equivalent to the ion's radius. The surface potential decreases linearly from the surface to the location of the counterions. Nevertheless, this remains a preliminary estimation, as the methodology assumes the presence of rigid layers of opposite charges, which does not accurately reflect natural conditions. Due to thermal motion, the mobile counter ions diffuse into the electrolyte until this tendency is counteracted by the opposing potential. The thickness of the diffusion layer that forms is influenced by the kinetic energy associated with ion motion. Gouy and Chapman independently developed the concept of the diffuse double layer, wherein the distribution of counter ions' concentration near the surface adheres to the Boltzmann distribution:

$$ɳ = ɳ_0 e^{-\frac{\mathrm{ze\varphi}}{\mathrm{KT}}} \tag{1.9}$$

where $ɳ_0$ is the bulk ion concentration, z is the charge of the ion, e is the charge on a proton, k is the Boltzmann constant, and φ is the electrical potential. This interpretation is appropriate for describing the behavior of a bulk solution, assuming that the activity is equivalent to the molar concentration. When approaching a charged surface, it is essential to consider the volume charge density in the analysis of Coulombic interactions. The volume charge density can be calculated as:

$$\rho_i = \sum_i z_i \, \mathrm{e} \, \eta_i \tag{1.10}$$

The Coulombic interactions on a planar surface can be described using the Poisson equation:

$$\frac{d^2\varphi}{dx^2} = -\frac{4\pi\rho}{d} \tag{1.11}$$

where φ varies from φ_m at the surface to 0 in the bulk solution. Solving the equation yields the potential distribution as a function of the distance from the surface. The thickness of the diffusive layer is determined to be:

$$\lambda_{double} = \left[{\varepsilon_\gamma KT}\Big/{(4\pi e^2 \textstyle\sum_i \eta_{i0} \, z_i^2)} \right]^{1/2} \tag{1.12}$$

The thickness of the double layer, as derived from the equation, is contingent upon the ion valence and concentration. The theory proposed by Gouy and Chapman effectively elucidates the interactions within the system comprising a rigid charged surface and oppositely charged ions from the solution, known as the diffuse double layer. The experimentally determined thickness of the double layer was found to be slightly greater than the predictions of the model. Stern subsequently proposed a further modification to the theory by positing that ions should not be considered as point charges, as previously assumed. Due to steric constraints, ions cannot approach the surface more closely than a certain distance б, which is approximately equal to their ionic radius and generally falls within a range of a few nanometers. Consequently, it was hypothesized that certain ions may be adsorbed onto the surface within the region currently identified as the Stern Layer. The potential drop

$(\varphi_0 - \varphi_6)$ is expected to occur across the rigid layer of a "molecular capacitor" (Helmholtz Plane), with the remainder of the potential drop occurring over the diffuse layer. The φ_6 is referred to as zeta (ζ) potential. The presence of the electrical double layer is fundamentally important for a wide range of applications. Notably, it plays a critical role in biosensors, where target charged molecules are screened by the double layer.

For studies of the liquid/solid interface, a site-binding model can be emploid to elucidate the interactions occurring at this interface. The Gouy-Chapman-Stern model includes the primary factors contributing to the formation of the electric double layer. It establishes a relationship between the charge accumulated at the electrochemical interface and the applied potential. Although the model accurately describes electrostatic interactions, it does not incorporate any chemical interactions. Chemical reactions occurring at the interface may result in the presence of a net charge at the insulator's boundary. This section examines the site-binding model, which facilitates the inclusion of chemical processes at the insulator interface in the analysis. The regular double layer model's failure to accurately predict the net charge density in the electrolyte underscores the necessity of incorporating chemical reactions at the interface through the site-binding model.

In contrast to electrostatic forces, which operate over extended distances, chemical reactions occur only at molecular proximities. Consequently, the hypothesis that chemical reactions are feasible exclusively within the Outer Helmholtz Plane (OHP) is adopted. Initially, ionic species derived from the dissolved salt are surrounded by a hydration shell, preventing them from approaching the interface closer than the Outer Helmholtz Plane (OHP). Consequently, these ions do not participate in chemical reactions at the insulator interface, assuming the absence of specific adsorption of salt ions. Secondly, the substantially smaller hydrogen ions are not obstructed by the OHP due to their significantly reduced ionic radius and absence of hydration. They can approach the interface sufficiently closely to facilitate chemical reactions. As illustrated in Figure 1.7, the surface of an insulator contains a substantial number of unsaturated bonds.

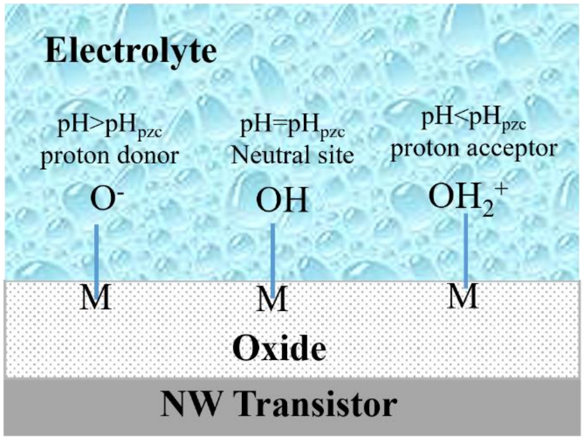

Figure 1.7 The surface of the insulator presents open binding sites due to the absence of bonding partners at the surface. These binding sites may exhibit negative, positive, or neutral charges, contingent upon the properties of the liquid that covers the surface.

Disregarding non-specific adsorption, the only ions capable of bonding to these sites are hydrogen and hydroxyl ions, as they are not shielded by water layers. The subsequent chemical reactions are in a state of dynamic equilibrium within the membrane, predicated on the assumption of thermal equilibrium and the absence of any net reaction (1.13):

$$M\text{-}OH_2^+ \rightleftharpoons M\text{-}OH + H^+, \tag{1.13}$$

$$M\text{-}OH \rightleftharpoons MO^- + H^+.$$

The symbol M represents the insulating material, such as SiO_2. The initial reaction typically results in a positive charge on the oxide surface, whereas the subsequent reaction generally induces a negative charge on the insulator surface. The ultimate charge density on the surface of the insulator is determined by the quantity of initial bonding sites, also referred to as amphoteric sites, as well as the local concentration of hydrogen ions. The chemical reactions can be expressed through the application of the law of mass action as follows:

$$K_a = \frac{[M\text{-}OH][H^+]}{[NH_2^+]}, \tag{1.14}$$

$$K_b = \frac{[M^-][H^+]}{[M\text{-}OH]}.$$

When calculating the surface charge as indicated in equation (1.14), it is essential to avoid using the bulk hydrogen concentrations. Given that the surface potential differs from the bulk potential and that chemical reactions occur directly at the surface, it is anticipated that the ionic charge distribution of hydrogen at the surface will also differ from the bulk hydrogen concentration. Consequently, the activity of hydrogen should be prioritized over the bulk hydrogen concentration.

1.3 Ultra high sensitive FET biosensors

With the advancements in semiconductor nanotechnology, FET devices demonstrate superior characteristics while scaling down in size. Additionally, transistors have played a significant role not only in traditional logic digital circuits in chips, but also in the exploration of life sciences. By combining the nanofabrication techniques of transistors with biochemical methods, it is possible to achieve more sensitive detection and analysis of the signals. This opens new opportunities for the development of transistors in the future. Such an FET-based device can be used to study biochemical processes, enable biological and optical detection, and achieve extremely high-sensitivity biological excitation. These transistors have different electrical properties (e.g., conductive transport) owing to their chemical or biological gates, which directly impact the surface potential of the channel. Meanwhile, a change in the surface potential can effectively adjust the concentration of the carrier in the nanochannel. Therefore, this type of transistor can be used as a new-generation sensor. In short, FET devices can not only be used as new-generation biological or chemical sensors but can also play an important role in optoelectronics and bioelectronics, as shown in Figure 1.6.

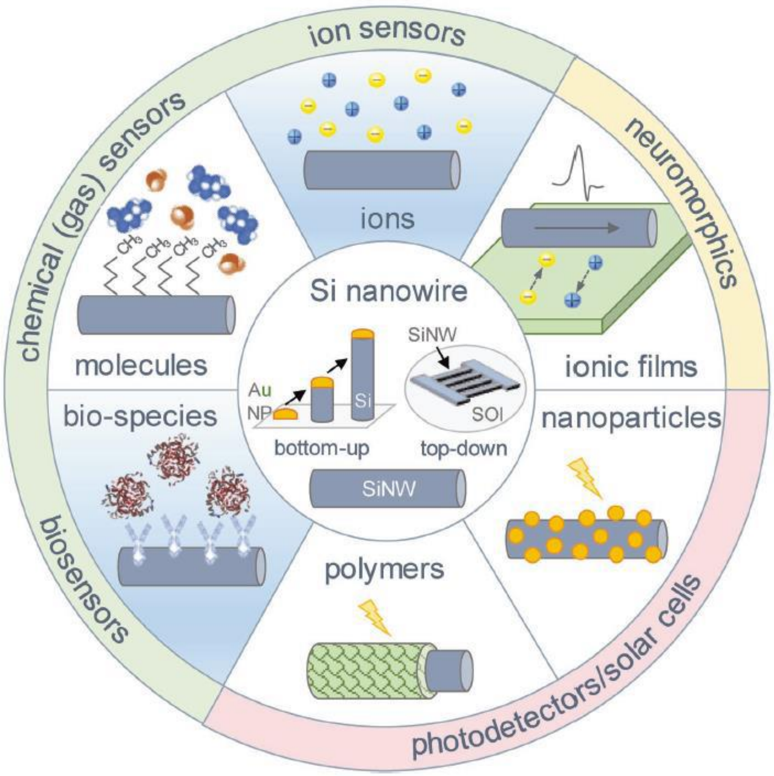

Figure 1.6 Application of nanowire transistors in different fields. (Reproduced from [20])

One-dimensional nanostructures, particularly FET-based nanostructures with silicon nanowires, have garnered widespread attention over the past decade as valuable components for transistor elements. This is mainly due to their highly complementarity and high surface area to volume ratio.[20] Currently, both commercial transistors and advanced examples use silicon as the substrate for fabricating the nano-channel.[21-24] However, it is important to note that the technology and knowledge regarding other related materials are still required for numerous experiments, and these materials cannot be considered as complete replacements for Si. In addition, owing to the high stability of silicon under various conditions, integrated nanowire transistors can potentially be used as a new generation of potentiometric sensors in the near future. In traditional MOSFET devices, the gate must be in direct contact with a dielectric oxide layer that covers the nanochannel. With the development and modification of FET structures, ion-sensitive field-effect transistors (ISFET) with a liquid gate have been successfully fabricated. In ISFET devices, the charged ion present in the detection solution is a complete replacement for the typical gate.[25] In 1970, Bergveld et al. were the first to utilize transistors for sensing purposes.[1] Therefore, the application of nanowires to sensors has a significant impact on the technology of ISFET. However, the revolutionary change in ISFET originated from the replacement of flat silicon with a one-dimensional structure of silicon.[26, 27]

In 2001, Lieber et al. from the Department of Biochemistry at Harvard University achieved a great contribution by successfully utilizing boron-doped silicon nanowire FET devices as biosensors for pH, biotin, and other high-sensitivity, label-free, real-time monitoring applications, as shown in Figure 1.7.[28] In particular, numerous experiments have provided evidence that the picomolar concentration range of streptavidin can be precisely and sensitively detected in solution. However, and more importantly, Lieber et al. reported that silicon nanowire biosensors can be utilized to detect individual viruses[29] and femtomolar concentrations of protein markers.[30] Inspired by these valuable reports, more and more scientists around the world began to focus on silicon nanowire transistors as sensors for various application fields. Next, we provide a brief overview of the key research findings regarding the exploration of the applications and functional diversity of silicon nanowire transistors.

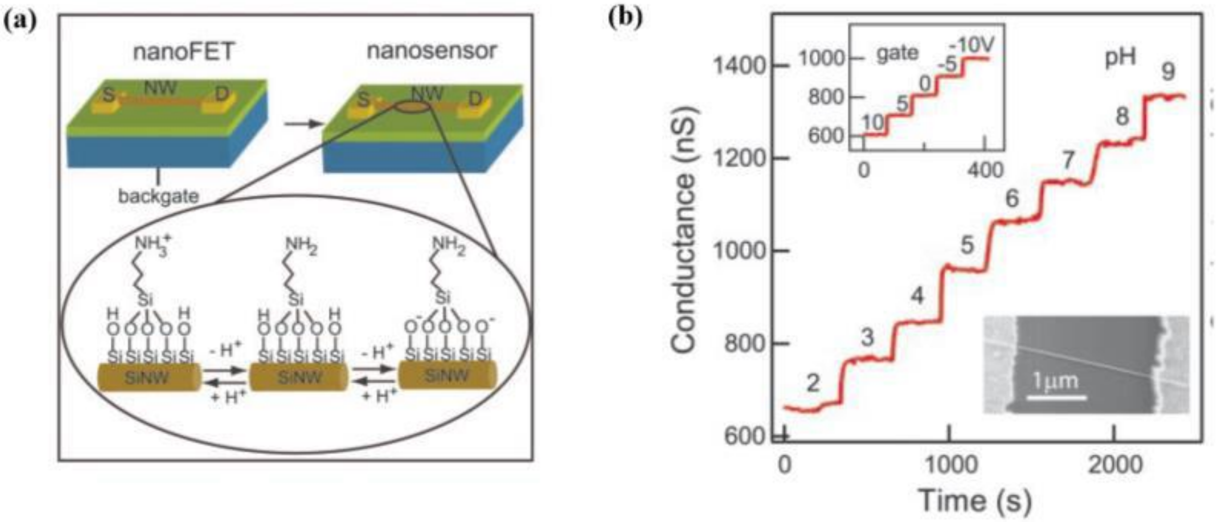

Figure 1.7 Nanowire transistors utilized as pH detection.(Reproduced from [28])

In 2016, Schütt et al. from the Technical University of Dresden designed and utilized the microfluidic channel integrated into silicon nanowire FETs, enabling the specific detection of enzymatic reactions through the pH value investigation, as shown in Figure 1.8.[31] During this detection process, the enzyme catalyzes the oxidation of glucose to gluconolactone. Gluconolactone is then spontaneously hydrolyzed, releasing protons that acidify the surrounding medium. This acidification allows for direct observation of the conversion rate of the enzyme-catalyzed reaction using this silicon nanowire FET device.

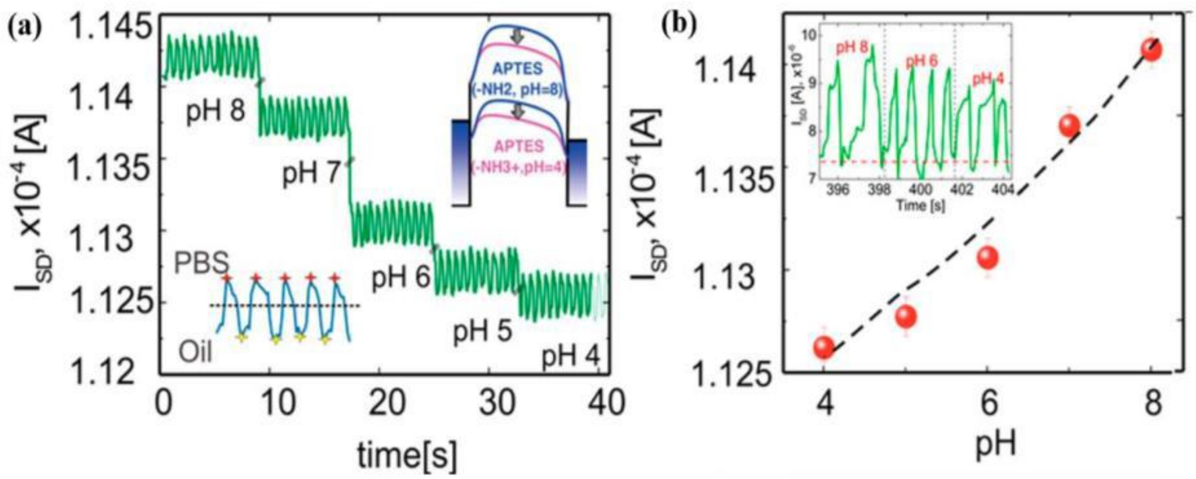

Figure 1.8 Sensitivity tests of nanowire transistors with respect to different pH.(Reproduced from [31])

Nanowire transistors function as biosensors, except for the basic detection of pH in solutions, which can also detect other components. Hsu et al. successfully fabricated a nanowire structure by using the top-down method and further performed functional treatment by binding glucose oxidase onto the surface of the nano-channel, as shown in Figure 1.9.[32] This approach enabled the investigation of the different concentrations of glucose. Numerous experiments have demonstrated that this type of reusable biosensor exhibits a very low detection concentration of 0.003 mg/dL, thus meeting the requirements for clinical use.

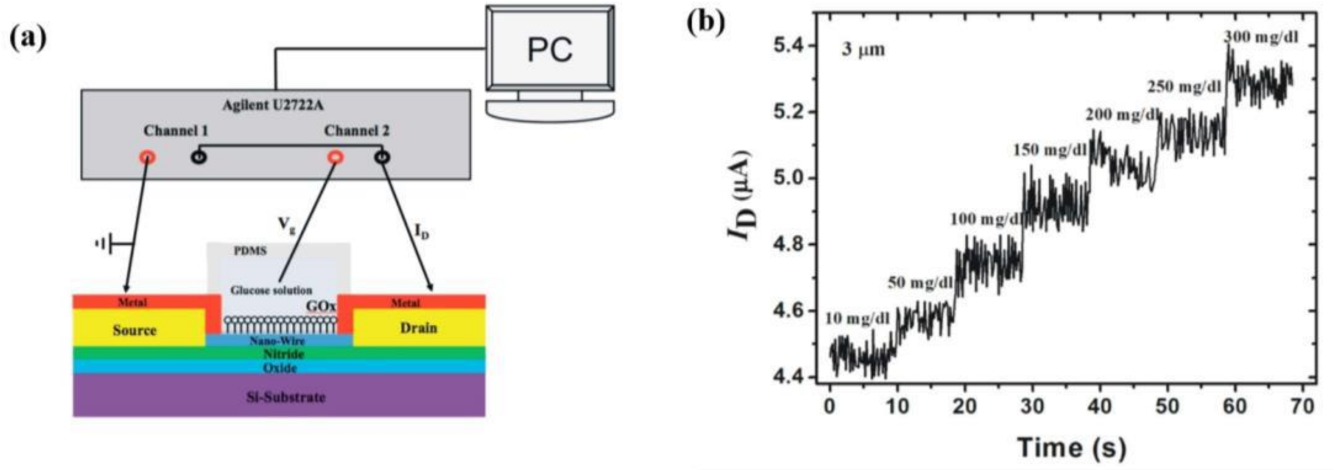

Figure 1.9 Silicon nanowire transistor sensor for detecting glucose concentration.(Reproduced from [32])

In 2018, Sivakumarasamy et al. from the University of Lille discovered that the small size of silicon nanowire transistors enables the adsorption of the divalent cations onto the surface of the channel, where serves as deprotonation sites.[33] The results of the experiments indicated a detection sensitivity that surpassed the Nernst limit by more than 230%. This improvement in sensitivity was originally due to electrostatic interactions and non-Coulombic interactions because of the built-in potential formed by the adsorbed cations floating at the stern layer. However, each cation has a distinct effect that allows for the generation of selective blood ionograms without the need for a functionally selective layer. As shown in Figure 1.10, Na^+, K^+, Ca^{2+}, and Mg^{2+} were used to build a model of the serum ions. This is an important milestone in the field of short-channel nanowire FET devices, serving as biosensors for the development of versatile and durable chemical and blood diagnostic tools.

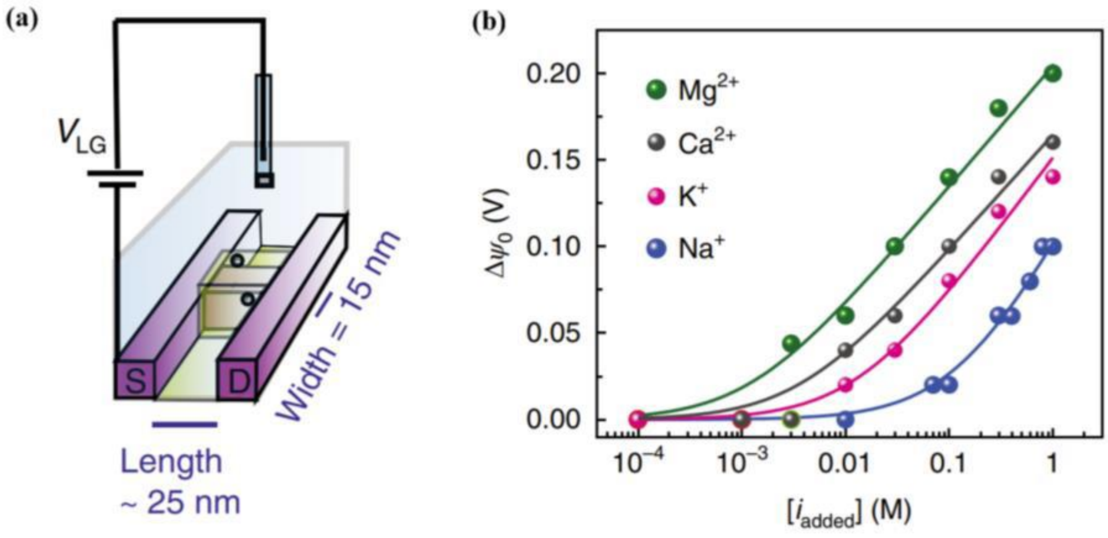

Figure 1.10 Nanowire transistor with 25 nm long channel for detecting different ionic solution concentrations.(Reproduced from [33])

In addition to being able to perform quantitative measurements of static biochemical liquids, silicon nanowire FET devices also exhibit an outstanding ability to investigate dynamic biochemical processes in real time. Peretz-Soroka et al. from Tel Aviv University employed silicon nanowire transistors with modification treatment of the surface to detect acidification processes, caused by glucose depletion and proton production in Jurkat leukemia cells, as presented in Figure 1.11.[34] This is a photovoltaic sensing nanostructured device with self-calibration. It features a surface modified by a photosensitive switchable molecular recognition layer, which induces self-calibration activation under 405 nm irradiation. The device can induce a change in current in response to a change in pH. Such transistors can serve as promising detectors for monitoring extra-and intracellular metabolic activities, enabling further studies of single cells and tissues in the future.

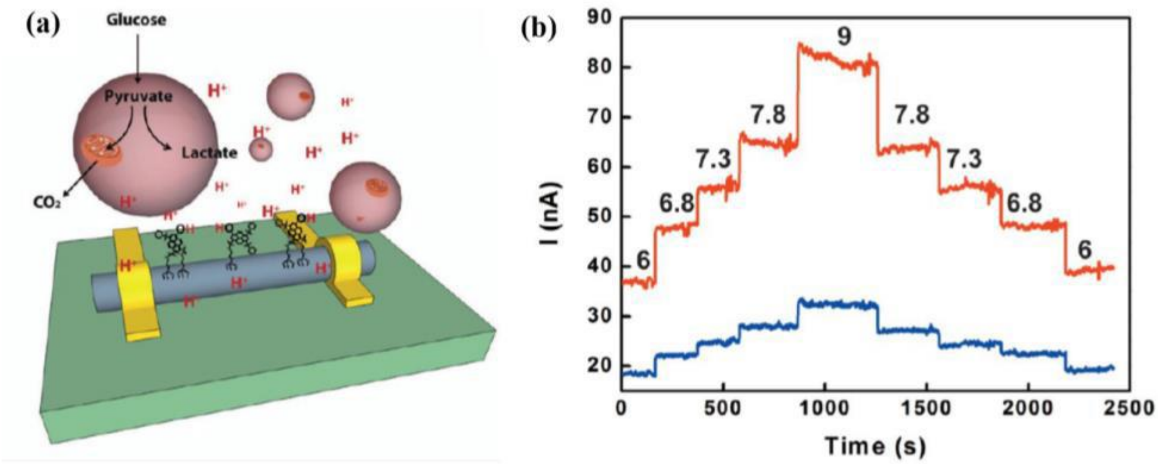

Figure 1.11 Silicon nanowire biosensor for detecting metabolic activity.(Reproduced from [34])

In 2017, Ibarlucea et al. from Technical University of Dresden reported that a honeycomb shape of silicon nanowire transistor can be used to measure bacterial growth and antibiotic reactions in microbe-associated nutrient media, as Figure 1.13.[35] However, the metabolic process and growth kinetics of Escherichia coli cells in an undiluted medium were determined via quantification of changes in I_{DS} due to different values of pH. Furthermore, the distinct effects of bacteriostatic drugs and non-solubilizing bactericidal drugs were determined using the electrical method, which was initially verified by measuring the changes in pH over time in bacterial cultures treated with antibiotics. In short, compared with the conventional optical method, this type of FET device has wide prospects for investigating microbial metabolic activities and stress reactions without being tracked in a label-free manner.

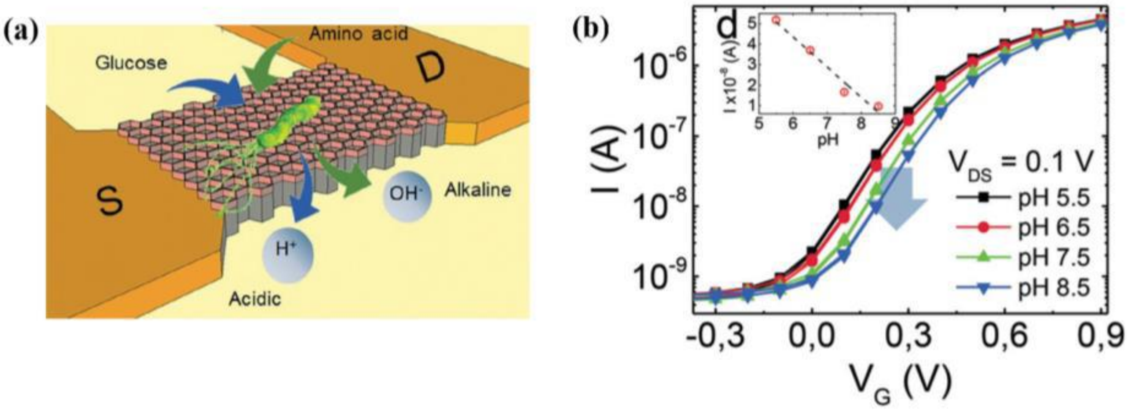

Figure 1.12 Silicon nanowire biosensor for detecting bacterial growth.(Reproduced from [35])

Because the FET is essentially an electrical sensor, it is also an ideal candidate for detecting the behavior of electrically active cells (e.g., neurons and cardiomyocytes). Generally, neurons are placed on top of the biosensor to form nanowire neuronal junction arrays, which can be utilized for monitoring, stimulating, and inhibiting neuronal signal transmission. At the same time, several silicon nanowire FTE devices were used to align long axons, enabling real-time tracking of the transmission of action potentials across the axon.[36] If cardiac cells were placed instead of long axons, it would also be possible to monitor their action potentials. In this case, to distinguish between signal dynamics related to inward and outward currents of Na^+, Ca^{2+}, and K^+ through each respective channel, it is also possible to detect intracellular signals by using a suitable nanowire structure, as shown in Figure 1.13.[37]

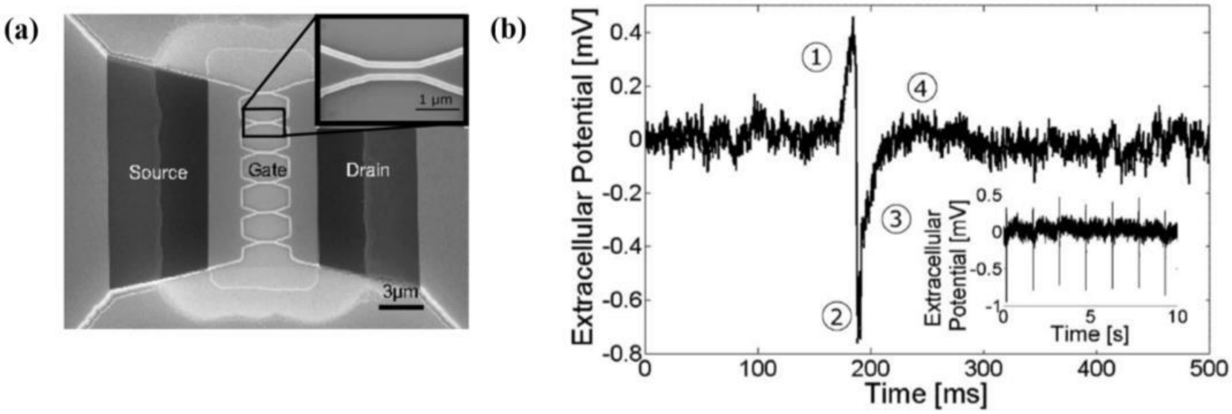

Figure 1.13 Silicon nanowire biosensor for detecting action potentials in heart cells.(Reproduced from [36])

FET-based devices are sensitive and precise sensors that enable the measurement of a wide range of applications including biological enzyme proteins, pH levels, ion concentrations, nerve cells, cardiomyocytes, and other organisms. They can also be used to detect antibodies that are classical biological receptors. Typically, such antibodies bind to a charged antigen, which affects the conductivity of the FET device, as shown in Figure 1.14. Jin et al. employed a silicon nanowire device via the technologies of electron beam lithography and immobilized monoclonal antibody to detect cTnl.[8] Such a device achieved a detection limit of 5 pg/mL, which sensitivity is one order of magnitude higher than the traditional detection method. The results demonstrate the promising prospects of FEF-based devices for future applications, enabling the provision of precise and sensitive measurements for the detection of cardiovascular diseases.

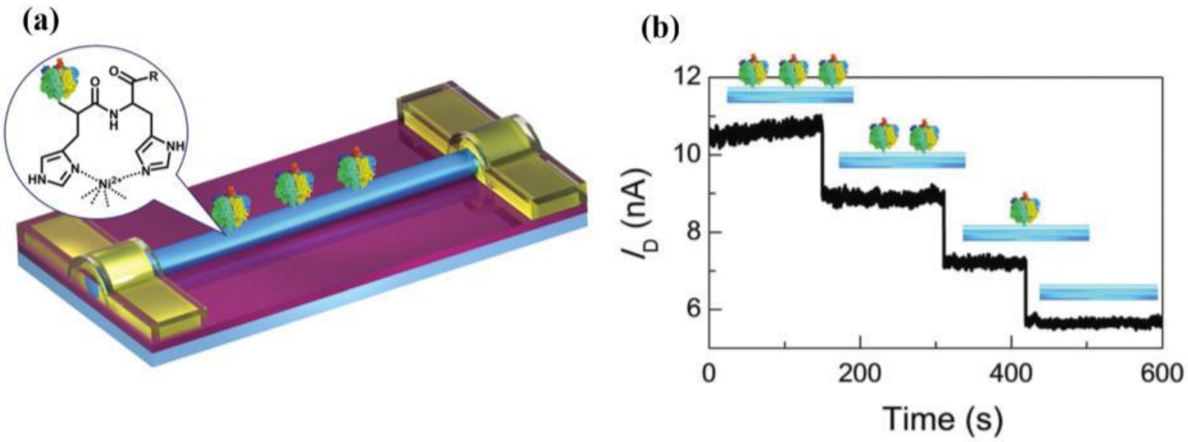

Figure 1.14 Silicon nanowire biosensor for antibody virus detection .(Reproduced from [8])

Tran et al. from University of South Australia designed and built an intraoperative biosensing platform based on silicon nanowire transistors, enabling quantified detection of disseminated tumor cells (DTC) in each lymph node and circulating tumor cells in peripheral blood within 1 h.[38] In Figure 1.15, the transistors fabricated the nanowire using electron beam lithography and then performed additional treatment for immobilized anti-cytokeratin antibody onto the surface of the nanowire. Notably, both DTC and circulating tumor cells (CTC) play an important role in the status of the patient's health. Such an FET-based platform showed superior sensitivity and fast response compared to conventional methods for pathologic examination of tissue sections. Meanwhile, it is possible that obtaining a precise and sensitive analysis of DTC presentations within the surgery timeframe could avoid unnecessary secondary surgeries for patients with cancer. Therefore, this can help reduce morbidity, improve mental health, and save money during treatment in the hospital. This valuable research strongly indicates the great potential of FET device technology in clinical cancer diagnosis in the near future.

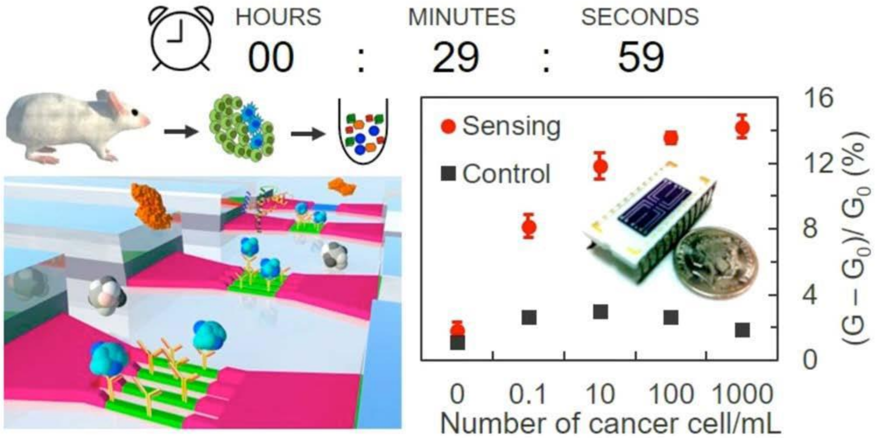

Figure 1.15 Silicon nanowire biosensor for tumor cell detection.(Reproduced from [38])

Wang et al. fabricated biosensors with single-molecule sensitivity and precise selectivity using a wet etching method involving HF/NH_4 to create a nanowire structure similar to an antibody. This enabled the real-time and label-free detection of influenza virus (H1N1).[39] In Figure 1.16, more details of the fabrication process are as follows: a nano-channel was utilized to immobilize an antibody against the H1N1 avian influenza virus (AIV) through chemical hydrosilanation. The remaining area of the nanowire surface was passivated with unreactive octadecyltrichlorosilane (OTS). As a result, integration of a single H1N1 hemagglutinin antigen with a microfluidic channel was demonstrated. Such biosensors offer a promising platform for exploring the dynamics of random processes in biological systems and obtaining information from genomics to proteomics.

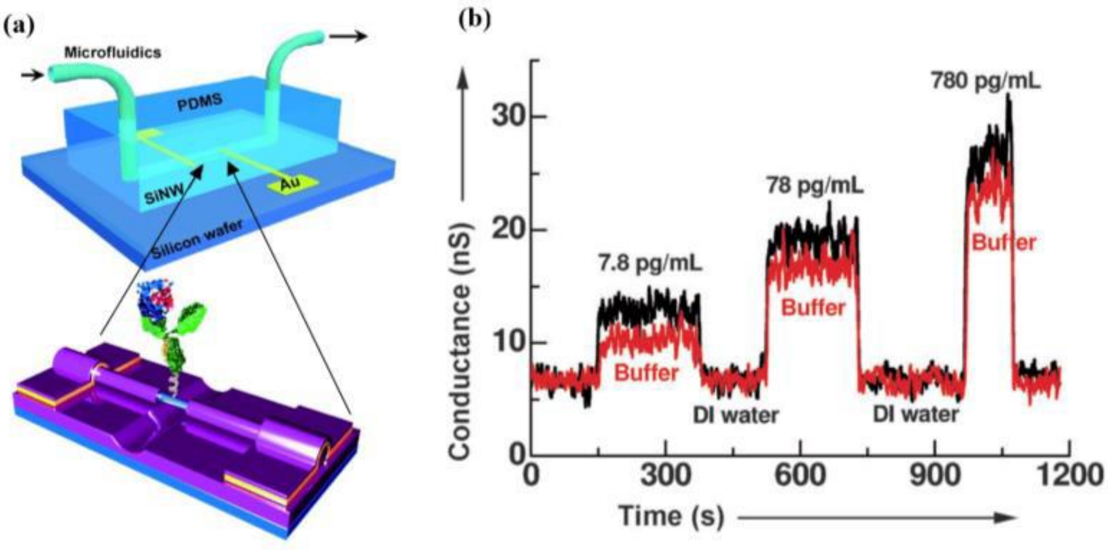

Figure 1.16 Microfluidic silicon nanowire biosensor for H1N1 influenza virus detection.(Reproduced from [39])

In addition, Gao et al. fabricated biosensors with a 20 nm width of silicon nanowire via wet etching, which enabled high specificity in the recognition of single base mismatch recognition during measurements.[40] Numerous experiments confirmed that such biosensors can rapidly and sensitively measure DNA at very low concentrations, even more 1 fM, as shown in Figure 1.17. Furthermore, a covalent DNA probe was used to modify the surface of the nanochannel, resulting in a highly sensitive and precise biosensor concentration as a function of electrical conductance changes that respond to specific target DNA sequences. The simultaneous measurement of two pathogenic viral DNA sequences at the same time was demonstrated using a proof-of-concept for multiplexed assays. To consider the advanced ability of real-time and label-free detection processes as well as the potential for commercially fabricated CMOS-compatible devices. Thus, silicon nanowire FET devices have a wide range of applications for real-time biological detection.

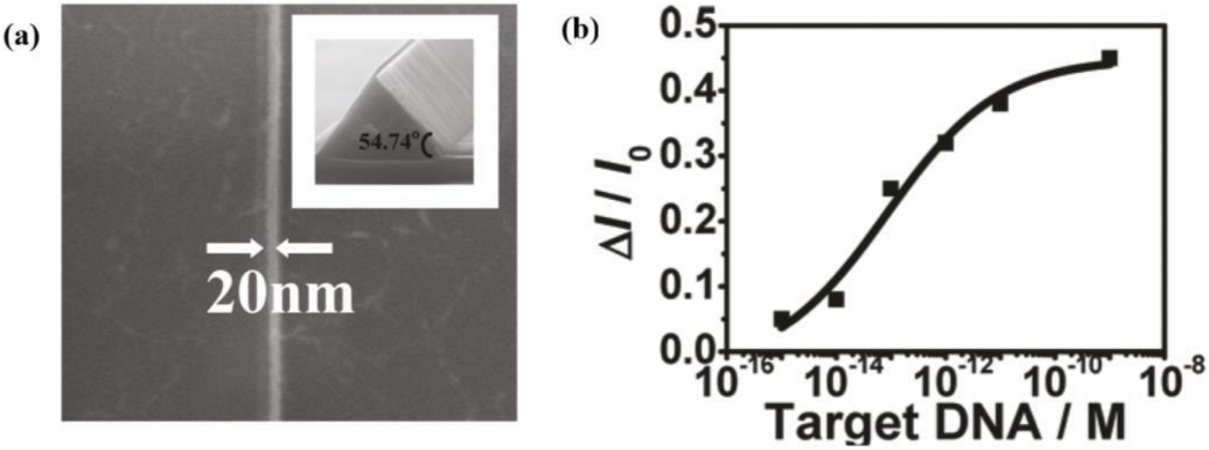

Figure 1.17 Silicon nanowire biosensor for DNA detection.(Reproduced from [40])

1.4 Noise spectroscopy theory

In any electronic device, there are intrinsic spontaneous fluctuations in the voltage or current; however, the mechanisms of these random fluctuations may differ depending on the type of device. Therefore, the development of high-precision and reliable biosensors enables high sensitivity and real-time detection of target analytes. In short, the noise characteristics are important factors to consider. The next section briefly describes the basics of noise.

Because silicon nanowire FET devices are complex systems, they typically have several noise sources caused by various spatial locations and different physical mechanisms. The different types of noise power spectral density (PSD) as a function of the frequency in a device (Figure 1.18) include thermal, shot, 1/f noise, and generation-recombination noises. Usually, it is noted that the various noises are not correlated, resulting in the PSD spectrum of the noise fluctuations being the summation of the individual noise components.

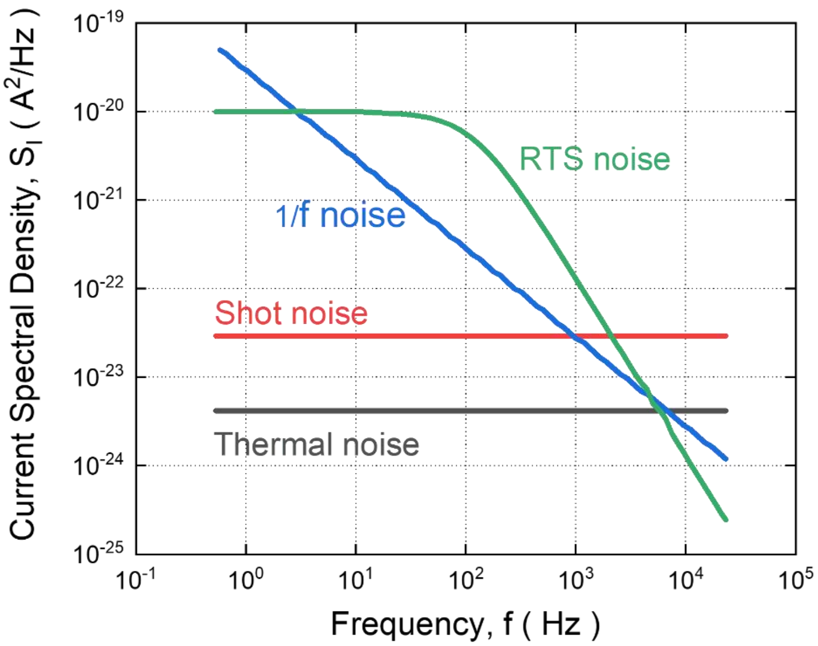

Figure 1.18 Schematic diagram of different noise power spectra of FET devices.

A. Thermal noise

Thermal noise is one of the most basic types of noise, and is caused by the thermal motion of electrons inside the device. It should be noted that the power spectral density as a constant does not depend on the frequency and belongs to white noise. However, thermal noise exists in all devices due to the thermal motion of free electrons inside the semiconductor structure, which occurs when the temperature is higher than absolute zero.[41] In general, the spectrum of thermal noise for a wide range of frequencies (i.e., GHz) is independent. Therefore, this is why thermal noise is also called white noise. Owing to the mechanism of thermal noise and its presence in all devices, the materials exhibit a constant value of resistance (R) at a certain temperature (T). Hence, the lowest value of noise in any electrical semiconductor device is dependent on the thermal noise. Simultaneously, the noises coming from other sources usually show higher noise levels than thermal noise. The formula for the current fluctuation of thermal noise is as follows:

$$S_I(f) = \frac{4KT}{R} \tag{1.15}$$

where K is the Boltzmann constant, and R is the differential resistance of the sample calculated by the equation $R = dV/dI$. However, the PSD of the thermal noise was not determined by the current or DC resistance of the sample. For different applications, thermal noise is widely utilized in the analysis of the effective carrier temperature and finite number of carriers interacting with scattered particles in fluctuation statistics.

B. Shot noise

In electron tube and semiconductor equipment, shot noise is caused by random fluctuations of carriers, as well as one type of white noise. Shot noise usually occurs in places with a potential barrier (e.g., P-N junctions and Schottky barrier). Then, the formation of shot noise when the carrier, electron, and hole cross the potential barrier.[42] Equation (1.9) for calculating the PSD of shot noise is given:

$$S_I(f) = 2qI \tag{1.16}$$

where q and I represent the elementary charge and direct current (DC) across the barrier, respectively. It should be noted that shot noise requires more attention at low temperatures. In this case, the level of thermal noise is sufficiently low, enabling the detection of a finite number of particles with PSD fluctuations.

C. Flicker noise

Flicker noise, which is also named pink noise, results from defects on the surface of the semiconductor.[43] It should be noted that 1/f noise also can represent

Flicker noise owing to its PSD being negatively dependent on frequency. Furthermore, its PSD is more easily observed in the low-frequency range, and this phenomenon exists even at extremely low frequencies. This type of noise is related to the material, shape, and type of operation. The equation for the PSD of Flicker noise is given by:

$$S_I(f) \sim \frac{1}{f^r} \tag{1.17}$$

where r is a parameter close to 1. For metal and nanowire semiconductor devices, r is usually between 0.7 of 1.3. Flicker noise is a major component of the low-frequency noise spectrum of FET-based devices and is affected by the quality of the nanowire in a complete transistor. In addition, the frequency range of the flicker noise ranges from 1 Hz to 10 Hz. One advantage of this noise is that it can effectively reflect the fluctuation of the conductance in the nanochannel of the biosensor. It is known that conductance is positively dependent on the free carrier concentration (n) and mobility (μ). Therefore, two theoretical models were introduced for the analysis of the flicker noise. The first theory involves a correlation with n; in this case, the charged carriers near the interface of the semiconductor or dielectric layer can be captured by the trap, resulting in PSD fluctuations. The other theory involves correlation with μ, where the charged carriers interact with the lattice, causing a scattering phenomenon that leads to fluctuations in the carrier mobility due to phonon scattering in the lattice.

1. Number fluctuation model

The number fluctuation model for carriers is aimed to explain the flicker noise formation in the nano-channel of the transistor.[44] In 1957, scientist McWhorter introduced this model to indicate the capture and emission process of charged carriers with the traps that exist in the Si/SiO_2 interface or in the gate oxide layer.

The carriers will create a noise fluctuation in the current or voltage owing to the random exchange of carriers between the traps and the nanochannel. However, the behavior of carriers to and from traps is called the thermally activated tunneling process, which depends on the nature of the traps and working conditions.

As discussed above, the interaction between charge carriers and a single trap can result in the introduction of a noise component with a Lorentzian shape in the PSD, which is called generation (G-R) noise. Therefore, assuming that a sufficiently large FET transistor might have several traps at the Si/SiO$_2$ interface, the summation of all the Lorentzian shape noise components caused by the single trap will eventually result in a total 1/f noise spectrum, while ignoring the effect of interactions between the traps. Following McWhorter's model, the PSD of the dielectric layer gate for 1/f noise can be defined as:

$$S_{V_G}(f) = \frac{q^2 N_t}{C_{ox}^2 A f} \tag{1.18}$$

where q represents the elementary charge, N_t represents the density of the oxide trap or other charge-trapping sources, and C_{ox} is the capacitance of the gate oxide layer per unit surface area, calculated as $C_{ox} = \frac{\varepsilon_0 \varepsilon_{ox}}{t_{ox}}$. The A and f represent the gate area and frequency, respectively. Hence, the current transport process in FET-based transistors is usually sensitive to the traps located in the gate oxide layer or the interface between the dielectric layer and the nanochannel. The study of the noise mechanism for McWhorter's model has been discussed in detail in other types of devices.[45-47] As found in numerous reports, this noise model is caused by traps that are typically better suited for application to transistors with an inversion mode. The conductive nanochannel of inversion-mode transistors is confined under the dielectric layer, also called the surface of the channel. In this case, both charge carriers tunnel into the trap from the nanowire, and the opposite tunneling process probably occurs. Therefore, the level of flicker noise depends on the quality of the Si/SiO_2 interface in the nanowire FET transistor device.

The McWhorter model is in good agreement with the results from the large gate area ($A > 1\ \mu m^2$) inversion mode transistor device in the measurement. However, this model does not fit all cases. First, this model could not offer a good explanation for FET devices working in the accumulation mode. Second, a transistor with an ultrathin gate oxide 1-2 nm SiO_2 layer will encounter several problems with this model owing to the rapid tunneling process of carriers to the traps near the Si/SiO_2 interface. To answer these questions, various theories have been proposed and studied, such as the mobility-fluctuation model.

2. Mobility fluctuation model

Both the mobility fluctuation model and the Hooge noise model show that 1/f noise in a conductive homogeneous bulk material is caused by fluctuation in charge carriers' mobility during the different scattering processes (e.g., phonon scattering).[48] Such fluctuations in PSD create Hooge noise and the formula is defined:

$$S_I(f) = I^2 \frac{\alpha_H}{Nf} \tag{1.19}$$

where N represents the number of charge carriers and α_H represents the dimensionless Hooge parameter. It should be noted that α_H is usually utilized for the quantitative assessment and comparison of the different levels of noise in various structures and devices. Initially, scientists considered α_H to be a constant value close to 2×10^{-3}. However, further studies have found that various scattering mechanisms depend on different parameters, such as the position of the nanochannel and the direction of the electric field. At the same time, α_H was employed to represent the level of noise, which depends not only on the fabrication process but also on the quality of the crystal and the bias added to the transistors. In general, the range of 10^{-2} to 10^{-6} for fluctuation in Hooge's noise depends on the operation mode and material properties in devices that use a silicon substrate.

Generally, the α_H parameter successfully describes fluctuations in 1/f noise with P-type transistors under the accumulation mode. It has also been confirmed that it exhibits volume conductivity rather than surface conductivity. Furthermore, a deviation from the expected behavior of noise for P-type transistors has also been frequently observed, such as in the regimes of subthreshold.[49, 50] In this case, modifications were proposed to improve the mobility noise model, especially the different scattering mechanisms that affect the different magnitudes of the fluctuation in the charge carrier mobility. Therefore, a lower value of the Hooge parameter can be predicted that the transistor operation is more likely in subthreshold regimes caused by a strong Coulomb scattering mechanism.[51] Usually, it is similar to the carrier number fluctuation, the fluctuation in mobility is very sensitive to traps, G-R centers, and defects located at the interface between the dielectric layer and the nano-channel. Although the precise source of mobility fluctuation in PSD is still not fully understood, the Hooge parameter still plays an important role in explaining noise in FET-based and metal-based semiconductor devices.

D. Generation-recombination noise

Generation-recombination noise is the result of discrete and random generation and recombination of charge carriers between traps and allows bands in the bandgap of the semiconductor. Such behavior, as described above, often induces fluctuations in the current by adjusting the resistance, and the PSD is calculated using the following equation:

$$S_I(f) = I^2 \frac{N_t}{N^2} \frac{\tau}{1 + (2\pi f\tau)^2} \qquad (1.20)$$

where N_t represents the number of traps, N is the total number of free electrons in the device under a given bias, I denotes the transistor drain current, and τ is the effective time constant for the capture and emission processes. Usually $\tau = 1/2\pi f_0$ is the fluctuation in the relaxation time constant, and f_0 is the corner frequency of the spectrum with a Lorentzian shape. However, the G-R noise exhibited a stable PSD until the frequency reached f_0, and a clear inverse square trend was observed when the frequency was larger than f_0. In short, the study of the PSD of G-R is necessary because it helps us understand the density of the traps and the level of energy.

1.5 Summary

Developments in nano-fabrication technology have led to significant improvements in the quality and properties of electronic devices, as well as reductions in cost and device size. One of the most unique examples is FET transistors. Since the first transistor was successfully designed and fabricated, it took only a few decades for billions of nanoscale transistors to be utilized in the fabrication of individual chip integrations for digital electronics. Simultaneously, the collaboration between nanotechnology and biochemical and biological sciences offers a new approach to nanodevices. It should be noted that these devices can be employed to further study biochemical processes and detect biological or optical signals. In this field, the new generation of sensitive and precise biosensors plays a critical role.

In the past decade, one-dimensional (1D) nanostructures, particularly silicon nanowire transistors, have gained considerable attention owing to their compliance with the process of complementary metal oxide semiconductors. Silicon nanowire transistors are typically manufactured with a high surface-area-to-volume ratio.

1. Introduction

P-type silicon nanowire FET-based sensors undergo changes in the accumulation region and conductance caused by external excitation of light, gases, liquids, and biological or chemical materials. However, some problems still exist that require scientists to solve in the investigation and development of sensors. For example, how to manufacture liquid gate biosensors with high properties, observing the behavior of ions near the solid-liquid interface during detection, and how to improve the sensitivity and precision of the biosensors.

In this thesis, the operation principles of advanced liquid-gated nanowire FET transistors are studied, the advanced technologies involved in the fabrication of biosensor processes are developed and described in detail, electrical and noise characterization methods are employed to investigate the performance of the biosensor. The chapters of this thesis are organized as follows:

Chapter 1 provides an introduction to the basic principles of operations of silicon nanowire transistors and their applications in different fields, including biosensors as well as an illustration of various noise components and suggested models for their description.

Chapter 2 presents conventional fabrication techniques for silicon nanowires, and also shows a series of processes in detail, including the design of the pattern, lithography, electron beam exposure, dry etching, wet etching, thermal evaporation, and encapsulation. In addition, homemade equipment including an electrical system (I-V and C-V) and a noise system were introduced.

Chapter 3 reveals that the Hooge parameter (α_H) and equivalent input noise (S_U) serve as effective indicators of the ion behavior on the surface of the nanowire. Notably, the noise curves exhibited two distinct turning points at concentrations of 10^{-4} M and 10^{-1} M for the peaks and valleys of α_H and S_U, respectively. These turning points reveal the conductivity transformation trend induced by ion behavior in solutions with varying concentrations of $MgCl_2$. These findings demonstrate that noise characteristics serve as a potent method for observing charge dynamic processes in the realm of biosensors.

Chapter 4 investigates liquid gate-all-around (LGAA) silicon nanowire (NW) field-effect transistor (FET) biosensors in 1 mM phosphate-buffered saline (PBS) at pH = 7.4. Our experimental findings reveal that the transistor current comprises the typical FET current component ($I \sim V^M$), where M equals 1, alongside the space-charge-limited-current (SCLC)-induced current components where M is greater than 1. Specifically, the SCLC-induced current, observed at $| V_{DS} | > 0.6$ V, was systematically analyzed in LGAA NW FETs using measured I-V curves, noise spectroscopy, and random telegraph signal (RTS) fluctuations attributed to trap states.

Chapter 5 proposes and illustrates the potential applications of the gold-bowtie antenna in biosensor technology. Through careful modulation of the light source intensity, we successfully triggered the excitation of a single center at the interface, inducing the RTS phenomenon without compromising the integrity of the dielectric layer. LGAA FETs with a gold bowtie antenna were fabricated and examined in a 1 mM PBS solution at pH = 7.4, employing infrared 940 nm LED excitation. Our electrical experiments revealed that the I-V curves shifted proportionally to the LED intensity, indicating the generation of photocurrent. Notably, we observed a distinct Lorentzian-shaped noise solely when the LGAA NW FET was illuminated by the LED. Our findings demonstrate a correlation between Lorentzian peaks in the noise spectra and the occurrence of RTS following the illumination treatment. Furthermore, the amplitude of the fluctuation associated with the two-level RTS exhibited a notable increase with increasing infrared intensity. These outcomes underscore the considerable potential of the gold antenna in harnessing single trap phenomena (STP) to leverage RTS for enhancing biosensor sensitivity.

In Chapter 6, we provide a summary of the various sections of this thesis as well as an outlook for the LGAA NW FET device in terms of future applications in the biosensing field, reflecting the importance of continuing to increase the focus and research in this area.

2. Fabrication and Characterization of LG FET biosensors

2.1 Design and fabrication of LG Nanowire FET devices

There are two classic methods for manufacturing nanowire biosensors: bottom-up and top-down methods.[52] Usually, the bottom-up approach is used to deposit high-quality nanowires on a silicon substrate. Therefore, while most grown nanowires have a cylindrical shape, the bottom-up way has a chance to modify the cross-sectional shape of nanowires, resulting in triangular, rectangular, and circular structures. Chemical vapor deposition (CVD) was employed to grow silicon nanowires during the fabrication process.[7] It should be noted that the mechanism of growing nanowires via catalytic reactions in the chamber of CVD system is vapor-liquid-solid (VLS) process.[53] Next, the silicon nanowire suspended in an ethanol solution is deposited onto a silicon substrate. Subsequently, the resist was spin coated to cover the surface of the substrate. Then, the metal electrode patterning was obtained by a further process. The bottom-up fabrication of nanowires requires passivation and surface modification owing to the propensity of nanowire surfaces to form isolation layers upon exposure to air or oxygen environments. Additionally, the bottom-up approach is accompanied by random orientation of nanowires, leading to lower uniformity and yield of nanowire biosensors. In short, this approach is not compatible with standard CMOS fabrication processes, making it unsuitable for commercial manufacturing of nanowire devices.

The difference between top-down and bottom-up methods is that silicon on insulator (SOI) or single-crystal silicon (SCS) should be chosen as the substrate. These nanowires are compatible with standard CMOS processes and can be manufactured using a top-down approach. The FET device preparation process starts from the top silicon layer of the SOI substrate with a low doping concentration of boron or arsenic. Subsequently, ion implantation is employed to define the source and drain regions of the nanowire after reactive ion etching (RIE) creates suitably sized source and drain electrodes. Next, nanowires of different sizes were exposed by E-beam lithography (EBL) between the drain and source, and metal feeding lines were deposited via thermal evaporation. Finally, necessary passivation or surface modification was performed on the surface of the sample. The properties of nanowires fabricated through a top-down approach are stable and reproducible and have great potential for large-scale manufacturing in factories. However, the nanowire size is typically larger than that of nanowires fabricated via the bottom-up method. Additionally, the fabrication equipment required in a cleanroom is expensive.

In this thesis, we adopt a top-down approach to fabricate GAA nanowire FET devices for advanced biosensing applications. The length of the nanowires produced using this method was 2 μm and the width ranged from 100 to 300 nm.

2.1.1 Layout design

Clewin 4 Layout Editor software was used to design the structure of the transistors. Figure 2.1 shows a schematic of the designed chip.

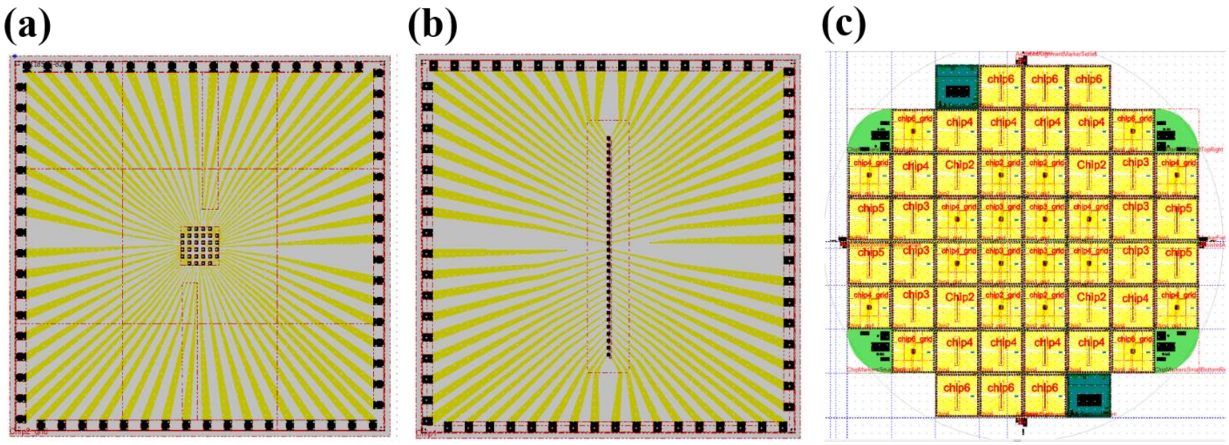

Figure 2.1 Schematic diagram of (a) grid distribution, (b) linear distribution of transistors, and (c) wafer layout.

We designed two different layouts for GAA FET sensors. One is a grid array distribution, where all transistors are arranged in a grid pattern at the center of the entire chip. The other is a linear layout, in which the nanowire FET devices are spatially distributed along a straight line in the middle of the chip. Both the linear and grid array layouts had 32 transistors in one chip sample. The linear layout is suitable for microfluidics, whereas the grid array layout is critical for cell measurements, distinguishing the difference between the two.

2.1.2 Major steps in the manufacturing process of FET device

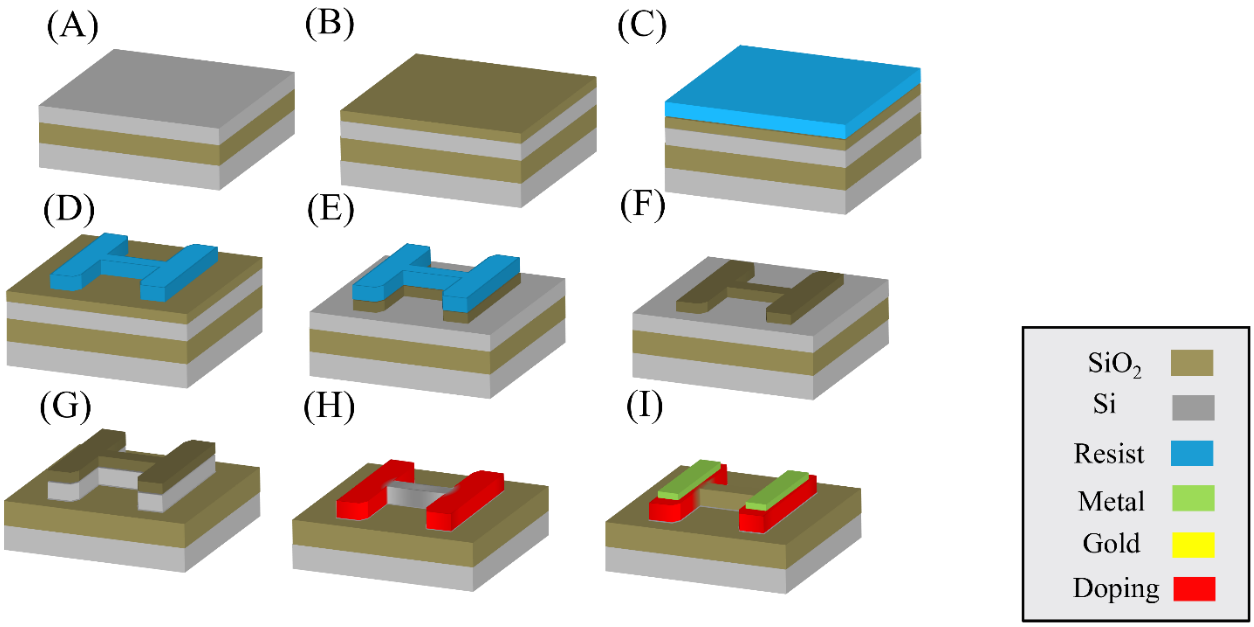

Figure 2.2 (a) Silicon on insulator substrate, (b) thermal oxidation, (c) spin coating resist, (d) define the nanostructure with exposure, (e) etch the silicon oxide layer to create a nanostructure, (f) remove resist, and (g) wet etch the silicon layer by 5% TMAH. (h) ion implantation and (i) metal deposition.

The low-resistivity (14 ÷ 18 Ω·cm) and low p-type boron-doped ($N_A = 10^{15}$ cm^{-3}) silicon layer with (100) crystallographic orientation of SOI substrate were used to fabricate FET transistors. The SOI wafer includes three parts: a ~100 nm top silicon layer, a ~150 nm buried SiO_2 layer (BOE), and high boron-doped (N_A = 10^{17} cm^{-3}) silicon substrates. An SOI wafer was purchased from SOITEC (France). Figure 2.2 indicates the major steps involved in fabricating FET devices in the cleanroom process.

2.1.3 The fabrication process of transistors

A. The fabrication of SiO_2 hard masks

High-quality hard mask SiO_2 plays an important role in uniform wet or dry etching and the precise definition of silicon nanowire structures. Therefore, we usually choose a ~20 nm silicon layer to cover the SOI surface as a hard mask via thermal oxidation. SiO_2 films can be deposited using various methods, including plasma-enhanced chemical vapor deposition (PECVD). However, SiO_2 grown by thermal oxidation exhibits better properties than that obtained using PECVD, particularly in terms of receiving a low-roughness edge on patterned thick silicon nanowires.

(1) Cleaning

A standard RCA cleaning process was performed to remove organic and inorganic residues from the SOI surface before initiating the thermal oxidation step.

(2) Thermal oxidation

Clean SOI samples were grown with high quality and uniform SiO_2 using a rapid thermal oxidation furnace at 900 °C for 40 min in a dry oxygen environment. An ellipsometer was used to measure the thickness of ~20 nm SiO_2 on the surface of the SOI substrate.

B. The fabrication of alignment marker

Alignment markers are crucial for the fabrication of high-quality nanowires with good shapes. Therefore, for EBL markers, we employed a pattern with four small squares with 20 µm sides and 100 µm spacing, located in the corners of each chip with an SOI structure. Meanwhile, optical lithography alignment markers were designed on the edge of the chips and included two scales for precise alignment with an error within 100 nm. Figure 2.3 depicts the two different patterns corresponding to the EBL markers and optical lithography markers.

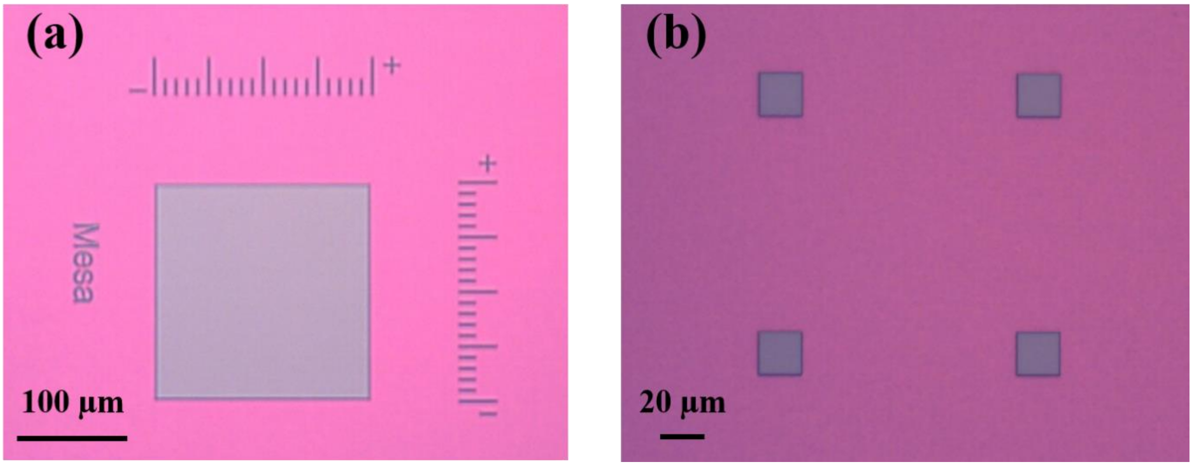

Figure 2.3 Alignment markers on the SOI sample for (a) optical lithography and (b) EBL.

(1) After growing a 20 nm SiO_2 layer as a hard mask, the SOI substrate was cleaned in acetone (ACE), isopropanol (IPA), and deionized water (DI) via 5 min of ultrasonication, followed by drying its surface with a nitrogen gun.

(2) Before starting the spin-coating process, the sample was heated in a hot place at 180 °C for 5 min to dry its surface. To improve the wettability of the SOI surface, the hexamethyldisilazane (HMDS) was treated at 130 °C.

(3) We used the negative photoresist AZ nLOF 2020 to cover the sample surface before starting spin coating at 4000 rpm for 45 s and then immediately placed it on a hotplate at 110 °C for 60 s.

(4) The Mask Aligner MA4 system comes from the German company Suss MicroTec with a UV light source wavelength of 365 nm to finish the alignment and exposure process. It should be noted that the mask was

better cleaned with IPA and DI water before and after exposure to ensure a good result. During the process, the exposure dose was kept constant at 40 mJ/cm^2 in the contact mode.

(5) Next, the sample needs to post exposure bake (PEB) at 110 °C for 60 s to guarantee a high-quality and high-resolution transfer of the structure from mask to photoresist.

(6) A solution of AZ 326 MIF was applied to develop the chip for 45 s, and then it was cleaned with DI water using a nitrogen gun to dry it.

(7) After development, there is a necessary post-exposure bake step at 120 °C for 120 s that hardens the developed markers in the resist layer. The final shape of the resist profile is determined using this step.

(8) Here, we selected RIE to etch the marker structures, which includes four main steps. First, CHF_3/Ar plasma was used to etch 20 nm SiO_2 for 60 s. Second, after opening the windows of the hard mask, the ~100 nm thick top silicon layer was etched using SF_6/O_2 plasma for 25 s. Next, the thickness of the ~150 nm BOE layer was etched for 7 min in CHF_3/Ar plasma. SF6/O2 plasma was then used to etch the silicon substrate for 21 s. Finally, the remaining resist in the exposed area was completely removed by O_2 plasma treatment for 120 s.

In short, both the EBL and optical lithography markers were tested using a Dektak device with a depth of ~600 nm. These markers were sequentially used in the alignment steps. According to the manufacturing process, the structures of the nanowires between the drain and source regimes should be defined by the EBL. More detailed information is provided below:

C. The fabrication of nanowires by EBL

After defining the alignment markers, the EBL technique was utilized to create nanowire structures using positive-resist PMMA (AR-P649.04K). The advantages of PMMA for silicon or silicon oxide substrates include high sensitivity, high resolution, and high-contrast lithographic performance. Thus, ~150 nm thick PMMA was covered on the sample surface by spin-coating at 4000 rpm for 45 s, followed by hot treatment at 180 °C for 5 min. Here, we used EBL to write nanowire structures in the PMMA layer. During EBL writing, we utilized a dose of 270 $\mu C/cm^2$ with a 5 nm beam step size. Subsequently, the exposure chip was developed in a solution of AR-P600-55 for 60 s, and then the sample was immersed in IPA to complete the process of development. Before using a nitrogen gun to dry the samples, their surfaces were cleaned with DI water. Subsequently, the nanowire structure was transferred from the PMMA layer to the SiO_2 layer via CHF_3/Ar plasma for 60 s during RIE. Wet etching using tetramethylammonium hydroxide (TMAH) was then utilized to create a nanowire structure on the silicon layer.

D. The fabrication of MESA structure

The MESA pattern was created in the hard-mask layer using optical lithography and RIE after transferring the nanowire structures to the SiO_2 layer. Here, we applied ACE, IPA, and DI water to clean the residual resist and particles on the surface of the sample, followed by drying the sample using a nitrogen gun and a hotplate at 180 °C for 5 min. A positive resist AZ 5214E was employed to cover the surface of the chip by spinning at 4000 rpm for 45 s. Then, hot treatment was performed at 110 °C for 60 s immediately afterward. For the lithography step, UV light and MESA markers were utilized to expose the sample to a constant dose of 75 mJ/cm^2. AZ 326 MIF solution was used as a developer to treat the sample for 60 s. Subsequently, a 60 s CHF_3/Ar plasma treatment was used to transfer the MESA structure from the resist layer to the SiO_2 layer. The final MESA and nanowire structures were presented on a hard mask layer, as shown in Figure 2.4.

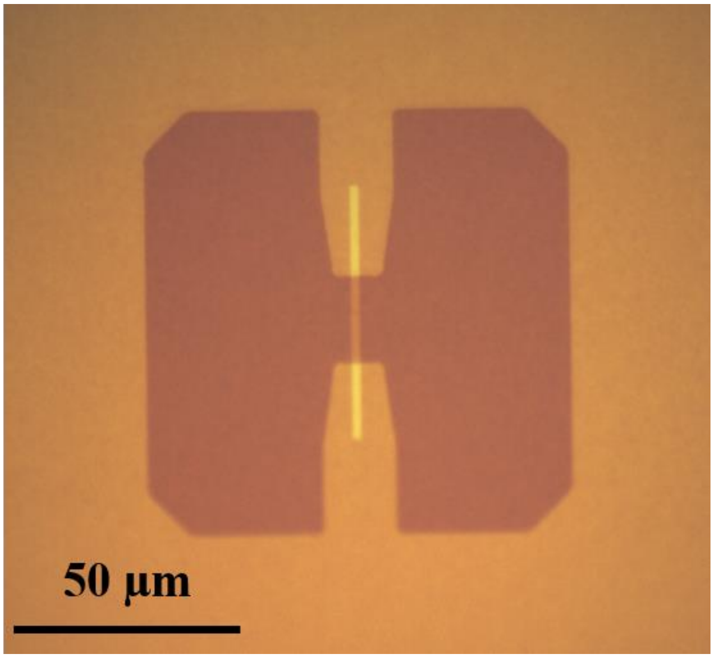

Figure 2.4 The optical image of MESA structure before wet etching.

E. The etching process of nanowire structure

To obtain a low-roughness surface and a reduced defect density nanowire structure, we utilized TMAH as wet chemical etching to transfer the designed patterns from SiO_2 to the silicon layer in an SOI substrate. To achieve uniform etching of the nanowire structure, the chip was first immersed in a 1% hydrogen fluoride (HF) solution for 30 s to remove the native oxide layer. DI water was then applied to rinse the sample surface for 60 s to ensure that it was cleaned. Next, a TMAH solution was employed to etch the silicon layer and create nanowire structures at 80 °C for 30 s. Finally, the sample was cleaned by rinsing it with DI water for 60 s. Figure 2.5 (a, b) shows the optical microscope image with a linear layout of nanowire structures and the scanning electron microscope (SEM) image of the nanowire channel.

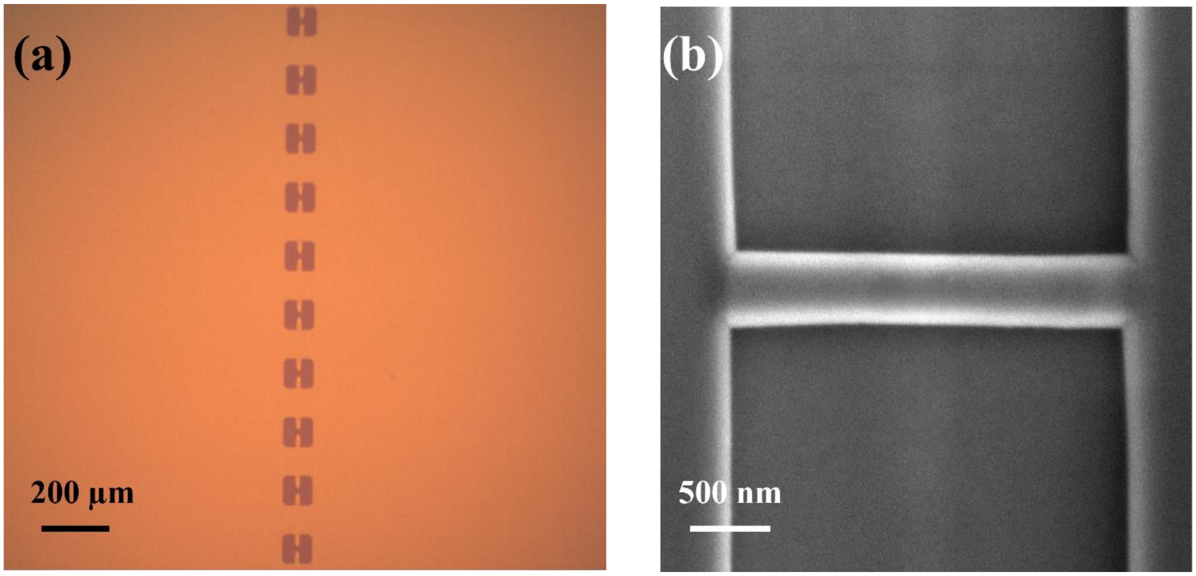

Figure 2.5 (a) Optical microscope image of linear nanowire arrays and (b) SEM image of nanowire channel.

Typically, for the preparation of ion implantation steps, a 1% HF solution was used to remove the native oxide layer for 30 s after TMAH etching. Immediately, 5 nm SiO_2 was formed by thermal oxidation at 900 °C to protect the designed patterned structure during the ion implantation process.

F. The fabrication of back gate structure

Generally, the source and drain of the biosensors are directly connected to the electrodes during the measurements. A liquid gate is used on top of the dielectric layer to control the channel state. However, during our fabrication process, we utilized a high-doped concentration of silicon substrate in the SOI as the back gate. For this type of structured device, the buried oxide layer SiO_2 serves as the gate oxide, and the current of the transistor can effectively flow through the channel, which is controlled by applying a voltage to the substrate. Therefore, a window was created for the back gate and then connected to the electrode, leading to a more precise control over the transport properties of the channel.

The sample used a positive resist AZ 5214E to cover the surface to define the pattern and was further annealed at 110 °C for 60 s. The development process employed AZ 326 MIF solution for 45 s after exposing the sample to UV light with a constant dose of 75 mJ/cm^2. Before opening the back-gate window, additional hot treatment was performed at 120 °C for 120 s to strengthen the resist. We chose a buffered oxide etch (BOE, 7:1) solution to transfer the pattern from the AZ 5214E layer to the silicon layer. It should be noted that the advantage of using a BOE solution to etch SiO_2 is its high selectivity. According to our experiments, the etch rate of BOE at room temperature is ~100 nm/min. In the BOE step, we immersed the sample in the solution for 2 min, which effectively removed all of buried SiO_2. The samples were then cleaned with ACE, IPA, and DI water. Figure 2.6 shows the optical microscope image of the back gate.

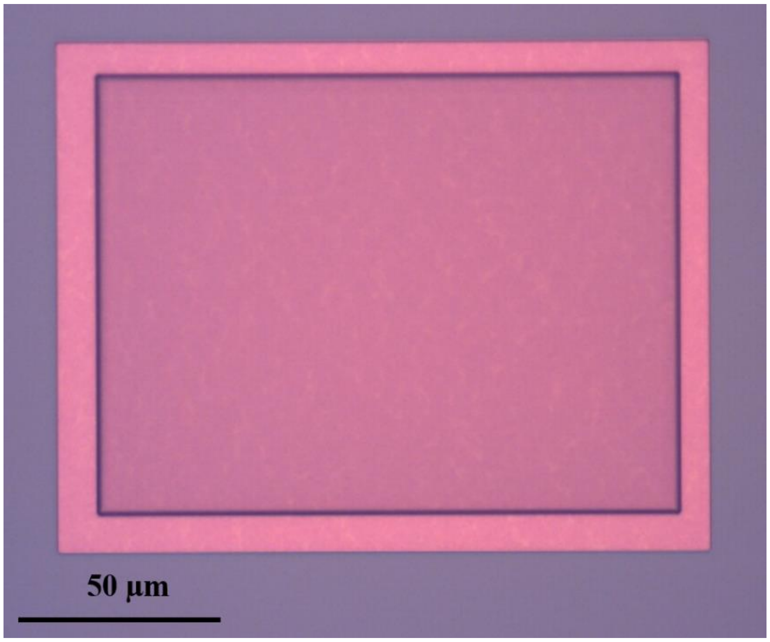

Figure 2.6 The optical microscope image of back gate

G. Ion implantation of drain and source contact

The drain and source regimes were successively defined by ion implantation using AZ 5214E at 4000 rpm for 45 s, followed by lithography with UV light after hot treatment at 110 °C for 60 s. Subsequently, boron (B) dopants were implanted into the sample with a 6 keV energy, a dose of 10^{15} cm^{-2}, and a tilt angle of 7 °. Finally, the sample was formed into an accumulation-mode P-type (P^+ - P - P^+) FET device. In contrast, for inversion-mode N-type (N^+ - P - N^+) channel structures, the arsenic (Ar) implantation parameters for energy, dose, and tilt angle were 8 keV, 10^{14} cm^{-2}, and 7°, respectively. Subsequently, the sample was immersed in ACE and IPA for 24 h to remove the residual resist on the surface. The intense high-energy ion bombardment and substrate heating during the implantation process resulted in strong molecular cross-linking of the resist. Consequently, a relatively extended cleaning time is necessary to eliminate the resist mark completely. In this thesis, p-type transistors were used to study electrical and noise properties.

Before proceeding to the next step, the chip was treated with 1% HF to remove the native oxide layer and a full RCA cleaning process was employed to clean the residual resist. To obtain good ohmic contacts, the implanted sample must undergo rapid thermal annealing (RTP). Therefore, both the P-type and N-type transistors were subjected to RTP annealing at 1000 °C for 5 s and 950 °C for 30 s. Meanwhile, the repair of crystal damage and activation of dopants occur during RTP processing.

H. Gate oxidation

After the ion implantation process, a 20 nm thick SiO_2 layer was grown using a thermal oxidation system at 900 °C. It should be noted that after HF treatment, the sample must be transferred immediately to the thermal oxidation chamber in an oxygen atmosphere. A high-quality dielectric layer is essential for applying a voltage at the top of the channel for device measurements in a liquid environment.

I. Metallization

The metallization process is crucial for the characterization of the sample. The drain and source regimes, feedlines, and pads were fabricated using lithography, deposition, lift-off, and annealing, respectively. Further details are as follows:

Here, the negative photoresist AZ nLOF 2020 and a dark mask were used to define the metallization area. AZ nLOF 2020 is a commonly used negative photoresist that is suitable for the lift-off step. Owing to its ability to obtain an undercut profile of the developed pattern, this resist prevents its sidewalls from being metalized, making the subsequent lift-off process faster and easier. AZ nLOF 2020 was spin-coated onto the sample surface at 4000 rpm for 45 s, followed by annealing at 110 °C for 60 s. For lithography, UV light was employed to expose the metallization area at a constant dose of 40 mJ/cm^2. A 1% HF dip was performed on the sample surface for 30 s to remove the native oxide layer before starting the metallization process. Prior to the deposition of 5 nm Ti and 200 nm Al, the contact area was cleaned using a Univex 400 metallization system with Ar plasma for 30 s. After the deposition process, the sample was immersed in ACE for 2 h for lift-off. Oxygen plasma was then applied to clean the sample and ensure that there was no residual resist on the surface. Subsequently, the metalized sample underwent RTP annealing at 450 °C for 10 min under a mixed-gas atmosphere to achieve a good ohmic contact. Figure 2.7(a, b) shows optical microscope images of the MESA structure and pad after RTP annealing.

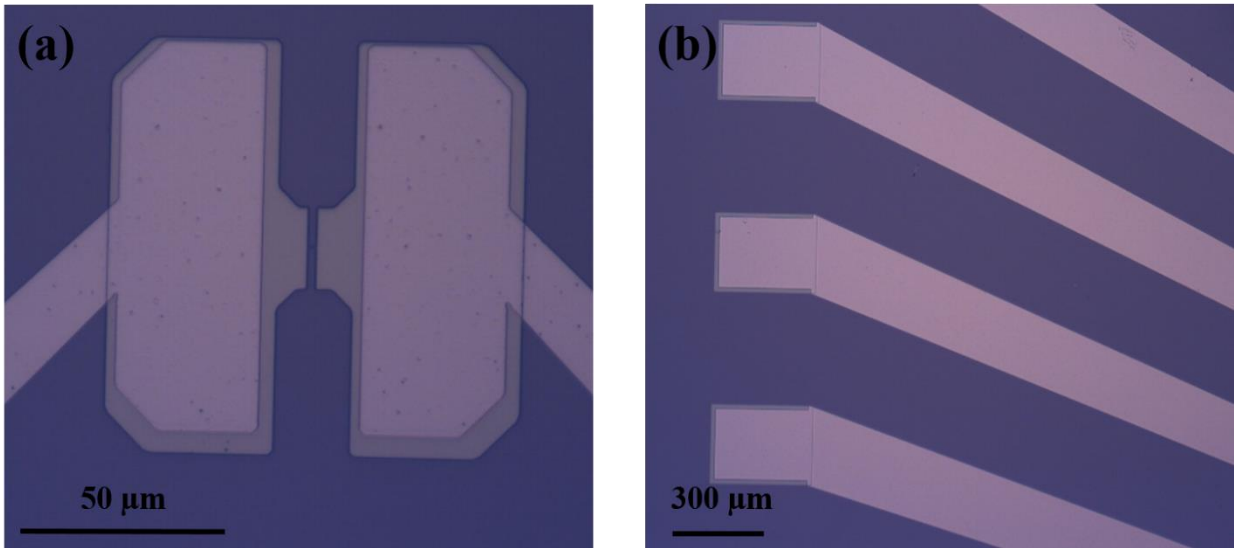

Figure 2.7 The optical microscope image of (a) MESA structure and (b) pad after RTP annealing.

J. Passivation

After the deposition process, a passivation layer was utilized to cover the metal area in order to protect the designed structure against liquid conditions during electrical and noise measurements. The windows for the nanowire channel and metal pads were exposed to a UV light with a negative resist. The metal pads were bonded to a sample carrier using a super-thin Al wire with a bonding system. The liquid came in contact with the nanowire surface during the measurements.

It should be noted that the passivation material employed was the polyimide (PI 2545) resist. Because PI 2545 is a highly biocompatible material, it not only exhibits outstanding stability in a liquid environment but also provides good protection against damage during dry and wet etching processes. First, the sample was placed under hot conditions at 180 °C for 5 min for dehydration before proceeding to the next step. VM 652 is an adhesion promoter material used in the process and was spin-coated onto the surface of the sample at 4000 rpm for 60 s. Subsequently, hot treatment at 110 °C for 60 s was performed to enhance the ability of the adhesive. Subsequently, PI 2545 was span-coated onto the surface of the chip at 4000 rpm for 60 s, followed by annealing at 140 °C for 6 min. Finally, the thickness of the passivation layer was measured using a Dektak, and was found to be ~1.5 µm. Here, AZ 5214 E was used to cover the passivation layer to create windows for the liquid measurements. For the lithography step, a bright mask was used to expose the pattern under UV light at a constant dose value of 25 mJ/cm^2, and a necessary flooding with 220 mJ/cm^2 was performed on the sample after baking it at 120 °C for 2 min. The recipe for AZ 326 MIF development was immersed in the sample for 40 s. The sample was placed in ACE for 2 h to remove the residual resist, and then dried with a nitrogen gun. In addition, an O_2 plasma treatment at a power of 200 W was employed to ensure that the sample was completely cleaned. Finally, the PI 2545 layer was placed in the furnace at 350 °C with a ramping speed of 8 °C/min for 30 min in a N_2 environment. The sample was then cooled to approximately 160 °C during 12 h. Simultaneously, the passivation changed to an insoluble film. An optical microscope image of the structure with the passivation layer is shown in Figure 2.8.

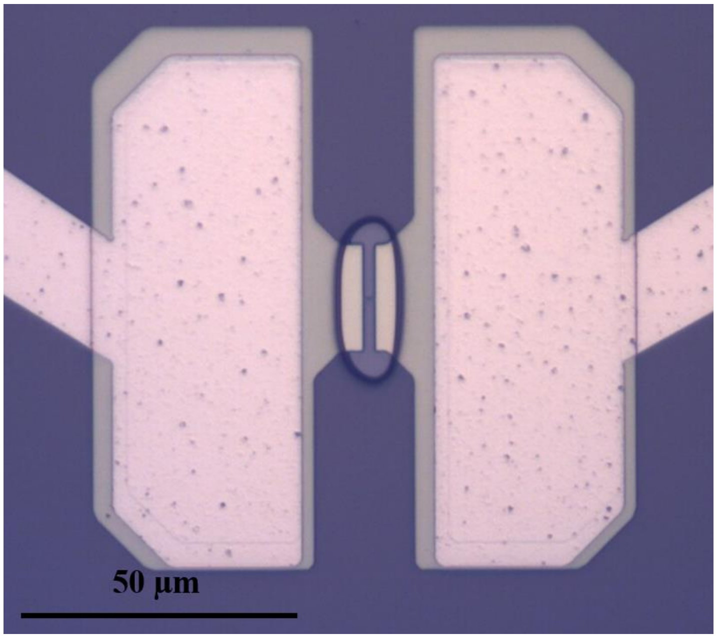

Figure 2.8 The optical microscope image of the MESA structure with passivation layer.

K. Bonding and encapsulation

After finishing all fabrication steps in the HNF clean room, the sample should be taken to the dicing process to obtain the right size of 11 × 11 mm, which is suitable for the next bonding and encapsulation processes. Before starting the bonding process, an 11 × 11 mm sample was attached to the center of the ceramic chip carrier using silver glue. For the bonding step, Al wires were used to establish a connection between the metal pad area of the device and the gold region of the chip carrier using a conventional ultrasonic method. To obtain more stable and reliable results, the transistor was encapsulated using polydimethylsiloxane (PDMS) and two rings of different sizes. First, an 8 nm inner diameter small glass ring was glued to the chip's center via PDMS to separate the nanowire area from the metal pad region. Second, a 20 nm inner diameter larger glass ring was glued to the periphery of the small glass ring to define the outer boundary of the space to be filled with PDMS. To obtain PDMS, 5 mL of curing agent was added to 45 mL of silicone-based elastomer at room temperature. A hot treatment at 120 °C for 15 min was employed to bond the two rings with the chip. Then, after filling the space between the bigger ring and the small ring with PDMS, the chip was treated at 120 °C for 1 h using a hotplate. It should be noted that during this step, it is important to carefully fill the PDMS to avoid the formation of air bubbles. PDMS is an ideal encapsulation material because of its superhydrophobic properties, high adherence, good biocompatibility, and excellent dielectric performance. Figure 2.9 shows the transistors after the encapsulation process.

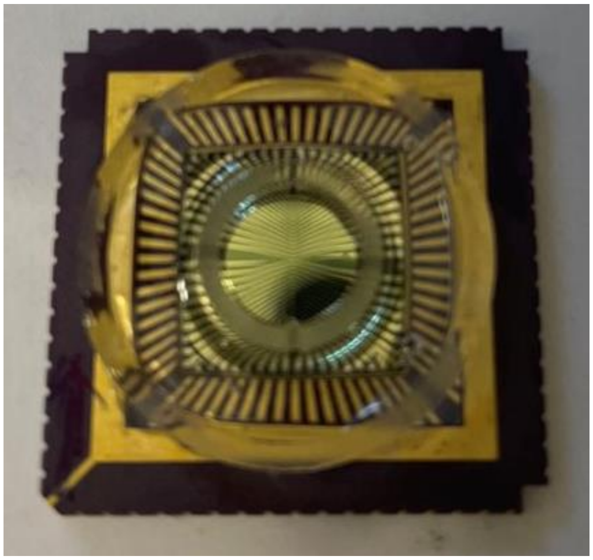

Figure 2.9 The optical microscope image of transistor after packaging.

2.2 Characterization of gate-all-around (GAA) Nanowire FET devices

The electrical and noise properties are the most useful and convenient methods for obtaining precise data on the behavior of ions near the liquid/solid interface. It should be noted that we constructed the I-V measurement system, noise setup, and C-V measurement equipment ourselves. Next, we introduce each of these.

2.2.1 Current-Voltage (I-V) measurement method

In general, our fabricated devices can be tested by adding voltage to both the metal and liquid gates. For metal gate testing, the back gate, drain contact, and source contact were connected during the measurement. However, for liquid measurements, a standard Ag/AgCl reference electrode needs to be immersed in the solution as a liquid gate. In the I-V test system, we used Keithley 2400 and 2430 source meter units (SMUs). All SMUs were capable of performing automated and precise electrical characterization of the device under test (DUT), providing a good resolution of 10 pA. Both the transfer and output curves can be observed using different modes of the measurement system. To avoid electromagnetic interference in all the measurements, it was necessary to use a Faraday box. To obtain the transfer curves, the drain-source current was investigated as a function of the gate voltage while maintaining a constant drain-source voltage. Meanwhile, for the output characteristics, the drain-source current is recorded as a function of the drain-source voltage at a constant back gate or liquid gate. All the biases must be applied to reference the grounded source electrode. To ensure transistor quality, the equipment also includes a measurement of the gate leakage current while recording the drain-source current. Usually, the gate leakage current is attributed to the degradation of the dielectric layer (i.e. SiO_2) or issues with the passivation material. It is worth mentioning that in this thesis, our focus was solely on further discussion of high-quality transistors that show no gate leakage current. To determine the electrical properties of the transistor, we added one more single-channel Keithley 2635 B SMU, which has a voltage measurement accuracy of approximately 1 µV. In short, the signals from the transistor were recorded using three SMUs in the I-V measurement, corresponding to the gate voltage, drain-source voltage, and back-gate voltage, respectively. Figure 2.10 shows a schematic diagram of the I-V system with the transistor. We used a GPIB-USB adapter to connect the computer with three SUMs.

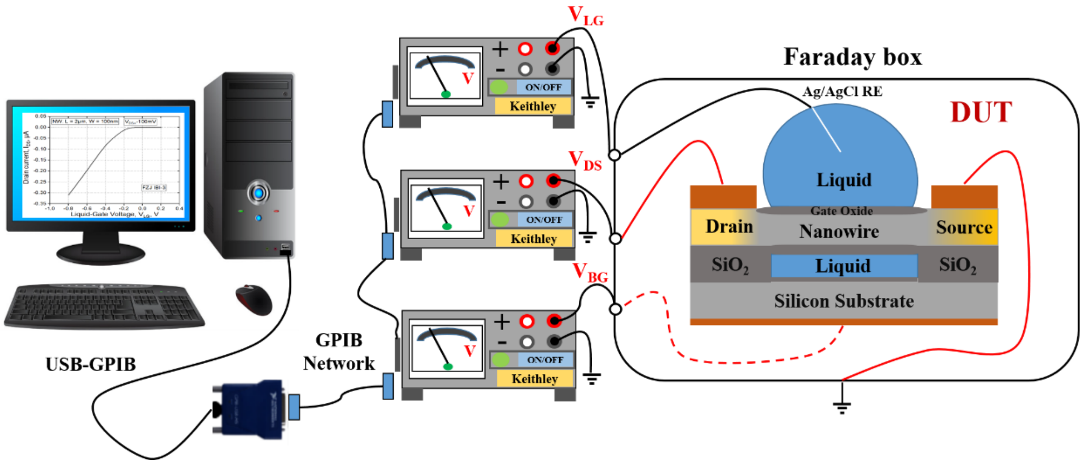

Figure 2.10 Schematic diagram of I-V characteristics test of silicon nanowire sensor.

Here, valuable data from I-V measurements were recorded and collected using software developed by our group, specifically created using PyIV. With the help of Dr. Ihor Zadorozhnyi, Dr. Nazarii Boichuk successively developed and optimized the Python scrypt. Finally, a more convenient version of the software was developed for the I-V test, allowing us to adjust a wide range of parameters such as voltage (i.e., V_{DS}, V_{LG}), sweep values, integration time, current compliance, measurement delay, averaging, and more. Moreover, this I-V program enables testing of the transfer and output curves in different modes, including forward and reverse cycling, to observe the phenomenon of hysteresis during the measurement.

2.2.2 Noise spectroscopy measurement method

Noise spectroscopy is a fundamental and effective method that is uniquely capable of detecting and characterizing the transport, quality, and reliability of electronic low-dimensional systems, including silicon nanowire transistors. Usually, trap and lattice damage in semiconductor devices of this type leads to electrical noise. This noise is caused by spontaneous fluctuations in voltage and current. Obtaining an extremely weak noise signal is a challenging task in the detection process. The noise characterization was subjected to interference from both internal factors and external environment. For internal factors, fluctuations in noise can be caused by components such as bias circuits, amplifiers, and other elements from the setup. In the external environment, noise amplitudes can be affected by electrostatic and electromagnetic irradiation, AC power lines, etc. Hence, a more carefully designed and optimized noise measurement system was utilized to avoid undesirable interference. This was performed to ensure the reception of reliable and precise data during the detection process, with minimal errors.

Figure 2.11 presents a schematic diagram of the homemade noise characteristic test system used to investigate the nanowire transistor. Initially, my previous colleagues, Dr. Viktor Sydoruk and scientist Dr. Mykhailo Petrychuk, along with my supervisor Prof. Svetlana Vitusevich, participated in the design and construction of this noise test setup. Subsequently, Dr. Ihor Zadorozhnyi and Dr. Nazarii Boichuk successively contributed to the maintenance of the measurement system and the optimization of the Python scrypt. This noise setup can be used to test the noise spectra of our transistor in the frequency range of 1 Hz – 250 kHz. Time traces of the voltage or current amplitude can be observed at a sampling rate of up to 500 kHz. A high sampling rate is necessary for precise analysis of single trap capture or emission of a single carrier, leading to the RTS phenomenon during the measurement. A brief introduction of the main parts of the noise system is provided.

First, attention should be paid to voltage supply systems. In this study, we applied a battery-operated circuit to counteract the parasitic amplitude caused by circuity. Meanwhile, two 6.7 V (6 V nominal) lead-acid batteries were employed to supply power for biasing bias on the contact areas of the transistor and setting the working points. BNC cables were used to connect the sample to the grounded source. However, two motorized potentiometers with a resistance of 2 kΩ were used to adjust the bias values of the drain-source and gate-source voltages. This adjustment was achieved by controlling the terminals using external voltage pulses. Therefore, the flexible operation of the test setup using the external voltage pulse method allows automatized and more precise measurement results to be obtained. Each parallel variable resistor was connected to a large shunting capacitance of 10 mF. This ensures stabilized voltages and serves as a part of the input for AC grounding purposes. In short, this convenient power supply system can receive a precise signal from the tested sample, with an error margin of ~1 mV.

Second, the DC characterization and noise measurement system play an important role in the detection process. The bias of V_{DS} is typically provided through the relevant circuit connection of the DUT and an additional load resistance (R_L). The R_L serves the purpose of maximizing the noise from the DUT to the output. Therefore, the value of R_L must be significantly larger than the channel resistance. Meanwhile, the thermal noise from R_L should be minimized. In tests, low-frequency noise from resistors in the metal film is usually eliminated using bias circuits to minimize interference. Here, a high-performance resistance box with a range between 1 Ω and 1 MΩ was utilized as the R_L, which plays an important role in the circuit. Considering that the DUT and R_L are connected in the same circuit, I_{DS} through the nanochannel should be considered along with V_M and V_S. The formula used is as follows:

$$I_{DS} = \frac{V_M - V_S}{R_L} \tag{2.1}$$

It should be noted that the bias voltage V_{LG} is directly connected to the gate contact area of the transistor without any additional elements. Simultaneously, voltmeter V_G was used to control the value of V_{LG} in the measurement. In Figure 2.11, all the voltmeters represent the voltmeter connected to the Agilent U2542A simultaneous data acquisition analog input channels. To obtain more reliable noise measurement results, it is necessary to switch off all the gates of the voltmeters (S_1, S_2, and S_3) to prevent any interference during the measurements. An analog input channel is used to measure the noise spectrum in the AC configuration.

Next, the amplification system played a critical role in noise signal processing during the test. The initial noise signal from the DUT was very weak, necessitating the use of an amplification system to amplify the tested noise signal. When designing a good amplification system, an important consideration is that the initial signal is mixed with the internal noise introduced by the amplification step during detection. This implies that the value of the internal noise signal should be minimized as much as possible in comparison to the desired noise signal. To achieve this objective, at the start of the measurements, the voltage fluctuations from the DUT in this equipment were preamplified using a custom-made preamplifier (k = 172) constructed by our group members. The intrinsic noise value of this preamplifier is $S_V = 10^{-17}$ V^2/Hz at a frequency of 100 Hz, which is the value of noise already one order of magnitude lower than the noise value of the Stanford SR560 amplifier. A homemade preamplifier with negligible internal noise, such as this, is crucial for subsequent signal processing. The noise signal is subsequently amplified using the ITHACO 1201 amplifier in the AC mode, which offers a variable gain from 1 to 10 k within the appropriate frequency range. In the final stage, the signal is directed to a low-noise general-purpose programmable gain amplifier PGA-103 (with gain options of 1, 10, and 100) and is further filtered using the digitally controlled antialiasing continuous-time filter LTC 1564 with a specifically chosen cut-off frequency of 100 kHz. To ensure that the valuable noise signal remains isolated from external interference, a metal Faraday cage is employed to enclose the circuit, the DUT, and the amplification system. Simultaneously, additional background noise from the entire noise system can be measured separately and subsequently subtracted.

The final component is the acquisition control system. Once the useful signal was recorded using the noise amplification system, it was recorded using an Agilent U2542A SDA device. The sampling rate was configured to a maximum value of 500 kHz, providing an optimal time resolution compatible with the hardware utilized. The voltage noise power density spectrum, $S_V(f)$, was computed using the time trace and Fast Fourier Transform (FFT), as follows:

$$S_V(f) = \frac{FFT^*(signal) \times FFT(signal)}{N^2} \tag{2.2}$$

where N and the symbol of "*" represent the number of points in the measured signal array and the complex conjugate, respectively. Equation (2.3) was used to recalculate the current noise power density spectrum ($S_I(f)$) based on the $S_V(f)$.

$$S_I(f) = \frac{S_V(f)}{R_{eqv}^2} \tag{2.3}$$

where R_{eqv} represents the equivalent resistance. It should be noted that the calculation of R_{eqv} using (2.4) is only applicable when the parasitic capacitance of the circuit and capacitance of the DUT are sufficiently small.

$$R_{eqv} = \frac{R_S R_L}{R_S + R_L} \tag{2.4}$$

where R_L and R_S are the load and transistor resistances, respectively. According to the noise measurements, the two possible boundary regimes are the constant-current and constant-voltage modes. In the constant-current mode, idle mode occurs when $R_L >> R_S$. Meanwhile, for the second constant-voltage mode, the short-circuit mode occurs when $R_L << R_S$. In fact, the real mode during noise detection is slightly more complex than the two modes mentioned above because it lies between two boundary regimes.

The PyFANS software used for noise measurement was developed by my former colleague, Dr. Ihor Zadorozhnyi. Python programming language was utilized in this software to control the main parts of the noise system, including voltage supply, data acquisition, and storage. At the same time, this noise system enables the measurement of low-frequency noise in silicon nanowire devices and similar nanostructure devices.

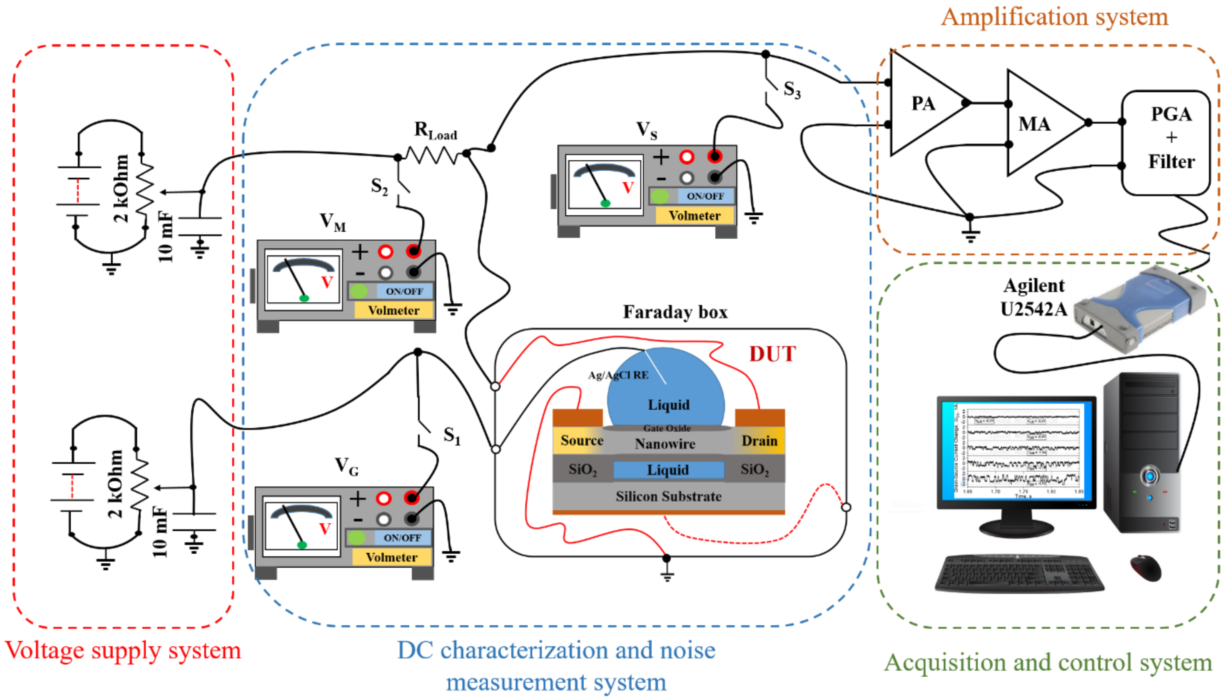

Figure 2.11 Schematic diagram of noise characteristics test of silicon nanowire transistor.

2.2.3 Capacitance-Voltage (C-V) measurement method

It is well known that the dielectric oxide layer plays an important role in the sensitivity and stability of the transistors. The C-V measurements were introduced to minimize the time and effort required for optimizing the preparation recipe. In general, the advanced design of an electrolyte insulator semiconductor structure (EIS) sample is considered one of the most effective approaches for investigating the interface between the dielectric oxide layer and liquid. This type of C-V measurement is widely conducted to estimate parameters such as the oxide layer thickness, oxide charges, ion mobility, and density of interface traps. Therefore, to further investigate the behavior of ions near the liquid/solid interface, a homemade C-V setup was utilized.

The homemade C-V system comprises two sample chambers (with each measurement using only one chamber), one reference electrode, one power supply setup, and two syringes for the electrolyte (one for injecting the liquid into the chamber and another for removing liquid from the chamber). For the power supply setup, Keithley 2400 was used to set the DC voltage (V_{DC}), while the Hioki 3532-50LCR HiTester was employed to measure the impedance of the sample by supplying AC voltage (V_{AC}) and measuring the responding AC current (I_{AC}). Figure 2.12 shows a schematic diagram of the homemade C-V characteristic test system used to investigate the EIS sample. During the detection process, a broad range of AC frequencies, from 100 Hz to 1 MHz, was used. It should be noted that the tested sample structure, from bottom to top, consisted of 200 nm Al, 10 nm Ti, a silicon substrate, and 20 nm SiO_2. When the liquid reached the surface of the sample, the effective area formed a circle with a diameter of ~0.7 cm at the center of the sample. To perform C-V measurements, CVIST software offers the capability to adjust various parameters. In particular, before starting measurements, the parameter frequency range, start and stop values of voltage, number of cycles and points for C-V curves, and speed of measurement can be applied. It should be noted that the temperature during C-V or impedance measurements will be recorded simultaneously with the testing.

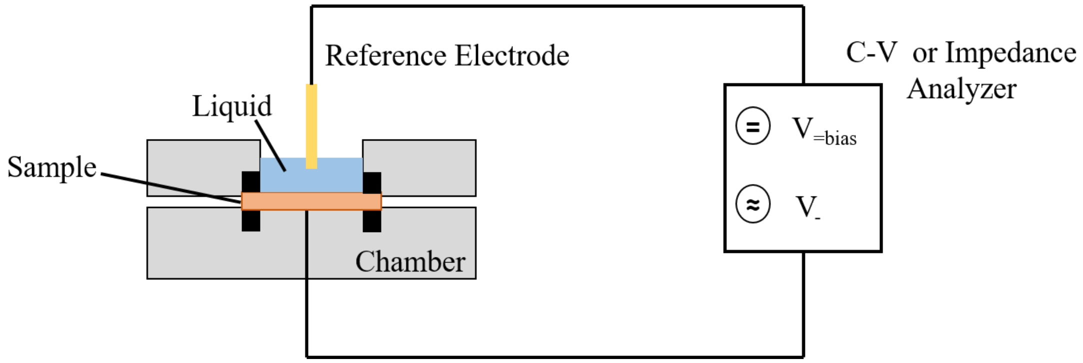

Figure 2.12 Schematic diagram of C-V characteristics test of the EIS sample.

3. Noise Spectroscopy Analysis of Ion Behavior in LGAA NW FET Biosensors

This investigation focused on the transport and noise characteristics of high-performance gate-all-around silicon liquid-gated nanowire field-effect transistor devices fabricated with various concentrations of $MgCl_2$ solutions. Through noise spectroscopy and capacitance-voltage measurements, the critical $MgCl_2$ concentration required for charge inversion at the solid-liquid interface was determined and validated. This study revealed that parameters such as the α_H and S_U serve as effective indicators of the ion behavior on the nanowire surface. The noise curves displayed distinct inflection points at concentrations of 10^{-4} M and 10^{-1} M, signifying peaks and valleys in α_H and S_U, respectively. These noise fluctuations were linked to the ion dynamics near the solid-liquid interface with varying $MgCl_2$ concentrations. These findings underscore the utility of noise spectroscopy for monitoring dynamic charge processes, particularly in biosensor research.

3.1 Ion behavior in liquid-gated FET biosensors

Field-effect transistors have garnered considerable interest due to their extremely high sensitivity, minimal detection threshold, and cost-effective fabrication techniques.[3, 54-57] Various types of FET biosensors have been utilized for disease detection, including heart and neurodegenerative diseases, aiming to safeguard human health. The detection mechanism of nanowire FET biosensors relies on the interaction of charged biomolecules with the nanochannel surface, leading to observable signals such as a shift in the threshold voltage. This shift occurred because of the alterations in the electrical potential of the nanochannel surface. Recently, a novel technique was introduced that leverages a single trap phenomenon within a dielectric layer to enhance the biosensor performance and sensitivity. [9, 58] The device has the flexibility to utilize various bioliquids, including PBS solution rich in monovalent ions, and $MgCl_2$ solutions containing divalent ions, serving as a liquid gate to regulate the surface charge density of the nanowires.[17, 58] To fabricate high-performance and durable FETs, it is essential to concentrate on the solid-liquid interface, particularly on the charge impact and dynamic processes occurring at this interface.

Currently, the detection mechanism of FET biosensors is similar to that of metal oxide semiconductor field-effect transistors, comprising a drain, source, nanowire channel, dielectric layer, and liquid gate, rather than a metal gate. Physiologically relevant liquids are typically utilized to dissolve target-charged biomolecules, thus creating liquid gates for molecular detection. To analyze the useful signal, which manifests as a potential change at the solid-liquid interface, different ion concentrations must be investigated. Typically, the presence of positive and negative charges near the solid-liquid interface is contingent upon the pH and ionic strength of the solution under examination. Kutovyi et al. noted that charged molecules interact with various ions in an electrolytic environment.[9] The Coulombic forces cause attraction between oppositely charged ions and repulsion between similarly charged ions. To explore the impact of ion composition at the solid-liquid interface at minimal solution concentrations, it is essential to develop recognition transducers capable of accurately recording electrical signals. This is particularly important because of the presence of various ions and molecules in biosensor solutions. Thus, expanding biosensor detection principles and ensuring the reliability of signal registration are critical for achieving high-performance devices.

The recent focus on charge inversion has garnered widespread attention owing to its significant role in diverse sensing applications. Li et al. conducted a comparison between monovalent ionic and $MgCl_2$ divalent ionic liquids at the solid/liquid interface within a microfluidic channel. They observed charge inversion within the microfluidic channel despite its small diameter.[59] Furthermore, it is essential to consider the contribution of counter ions [60] in influencing the compensation of surface charge at the solid/liquid interface. Although the charge inversion phenomenon has been noted in previous experiments, extensive discussions regarding its origin are prevalent in the literature. The authors of [61, 62] proposed that the inversion effect is likely explained by ion-ion correlations. Additionally, they suggested that the site-binding model, which is effective in calculating theoretical surface charge densities, could elucidate the mechanism of ion binding to surface groups of the dielectric layer.[63] The analysis involves multiple capacitors arranged in series, encompassing the establishment of a double-layer capacitance and the formation of Helmholtz planes at the solid-liquid interface during ion detection. This configuration consists of a double layer where negative (positive) ions initially reach the surface, forming the first layer, whereas positive (negative) ions create a distinct second layer. As the distance from the solid-liquid interface increased, the potential diminished owing to the diffusion process and alterations in the ion concentration.

The sensing capability is often a pivotal aspect in assessing the efficacy of a device. To enhance the sensitivity of FETs for pH sensing, an extra coating layer overlying the gate oxide layer may be utilized to mitigate the impact of other ions in concentrated electrolytes. Wipf et al. utilized a thin layer of gold film to alter the nanowires for surface functionalization to detect particular analytes. In their study, a response to Na^+ ions was observed to be approximately -44 mV per decade in NaCl solution.[64] Sivakumarasamy et al. fabricated a special 25 nm silicon nanostructure without implementing a selective layer onto the SiO_2 layer to investigate the ion–surface interaction.[33] They examined Na^+, K^+, Ca^{2+}, and Mg^{2+} ions present in blood serum using these transistors and proposed that strain might be a potential mechanism contributing to selectivity. Hence, it is imperative to further investigate the impact of ion interactions with semiconductor substrates on transistor structures for various biochemical sensor applications.

Previous research has indicated that the charge states formed near the surface of nanowires can profoundly affect the transport properties and notably enhance the sensitivity of device. Guo et al. examined ion-related phenomena in two-layer silicon nanowire FETs and observed the occurrence of the SCLC effect in liquid-gated nanochannels.[65] The SCLC is recognized as a valuable technique for investigating solid surface trapping processes. Many investigations have highlighted the significant contribution of SCLC in redistributing carriers within nanochannels, particularly in nanowire structures such as GaAs, CdS, GaN, InAs, and ZnO.[66-71]

Furthermore, Lemay et al. conducted a systematic investigation of charge inversion with multivalent ions in 2005.[72] They utilized atomic force spectroscopy (AFM) to directly assess the charge inversion by examining the dielectric constant and surface charge density of various liquids. This approach revealed alterations in the critical concentration under different conditions, with varying complex permittivities. The authors emphasized the importance of considering both physical and biochemical phenomena at the solid-liquid interface. In summary, further investigation of the double-layer capacitance near the nanochannel surface is imperative, particularly given the potential medical diagnostic applications of FET devices.

The C-V characterization is an effective method for examining the behavior of the diffuse double-layer capacitance at the solid/solution interface region. Additionally, multiple studies have affirmed that the potential diminishes with increasing distance from the surface in the context of the double-layer capacitance.

Christensen et al. emphasized the varied shapes of C-V curves observed across different concentrations of KCl solutions, indicating a clear correlation between the double-layer capacitance and ion behavior near this interface.[73] Moreover, Hlukhova et al. employed the electrolyte-insulator-semiconductor (EIS) structure, coated with a functional layer, to improve the selectivity and sensitivity when testing various concentrations of antigen, utilizing the C-V characteristic as an effective method. [74] C-V measurements have the potential to be utilized for investigating the behavior of different ions at the solid-liquid interface within a nanochannel.

Although advancements have been made in modeling to elucidate the phenomenon of inversion at the solid-liquid interface, the direct monitoring of processes at this interface remains a crucial aspect. Recent findings indicate that noise spectroscopy is a highly sensitive method for investigating the dynamic processes in nanodevices and hybrid materials. It is important to highlight that the fluctuation processes and dimensionless Hooge parameter [75-77] enable a quantitative comparison of the intensity of dynamic processes across various materials and devices. Meanwhile, investigations into Hooge parameters in scenarios involving the presence of divalent ions in dynamic processes at the solid-liquid interface, potentially including the inversion effect, have not been documented in the literature.

In this chapter, we manufactured and examined characteristics of LGAA nanowire FETs featuring a 20 nm SiO_2 dielectric layer. Our aim was to investigate the behavior of Mg^{2+} ions at the solid-liquid interface across a concentration range of 10^{-6} M to 1 M. Notably, $MgCl_2$ solutions play a crucial role in the human body. These solutions are involved in numerous enzymatic reactions and DNA folding processes, and their concentrations serve as indicators of the gastrointestinal tract health status. We illustrated a narrow V_{TH} range of -0.2 V to -0.3 V for the transistors, with several I-V curves observed across various concentrations of $MgCl_2$. Additionally, noise spectroscopy was utilized to examine the behavior of ions at the interface between the solid and liquid. The crucial α_H and S_U were examined to investigate the impact of surface properties. Initially, both α_H and the spectral density of S_U decreased with an increase in $MgCl_2$ concentration, reaching their minimum values at 10^{-4} M, and subsequently reaching maximum values at approximately 10^{-1} M. It was shown that the noise fluctuations stem from the ion behavior on the nanowire surface, aligned with the findings obtained using the C-V measurement technique.

3.2 Transport properties of LG GAA FETs

The schematic design of the LG GAA FET with a Si substrate/buried SiO_2/Si nanowire channel/gate SiO_2 is shown in Figure 3.1 (A). Nanowire channels, measuring 2 μm in length and featuring atomically flat surfaces, were fabricated from a silicon layer with a low doping concentration ($\approx 10^{15}$ cm^{-3}) on a SOI wafer. An scanning electron microscope (SEM) image of the nanowire cross-section was obtained after cutting the nanowire using focused ion beam (FIB) technology (Figure 3.1 (B)). One can observe that the nanowire has a trapezoidal cross-section with top- and bottom-base widths of 100 nm and 200 nm, respectively. The silicon nanowire was shielded by a 20 nm thick SiO_2 layer to prevent direct contact with the liquid. Our focus was on investigating the transport and noise properties of the fabricated devices under various $MgCl_2$ solutions with different V_{LG} and V_{DS} settings.

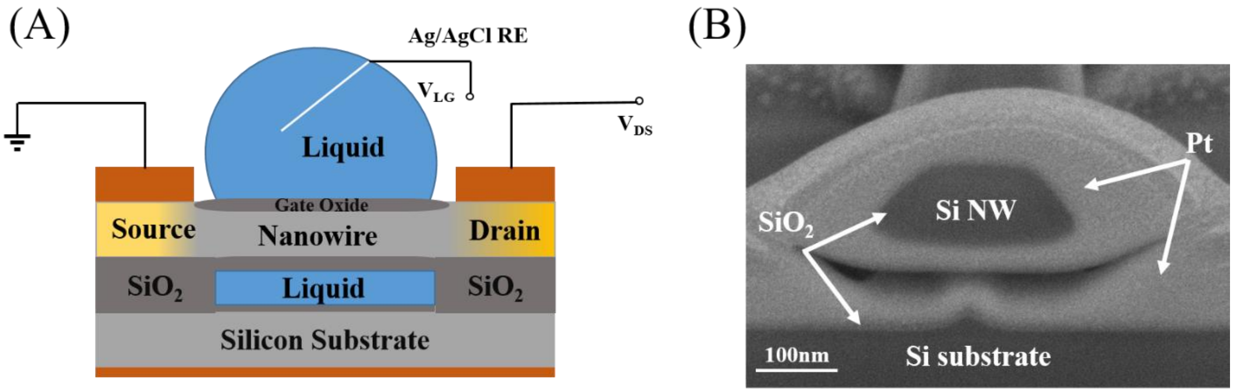

Figure 3.1 (A) Schematic depiction of the gate-all-around Si nanowire FET. (B) Scanning electron microscope (SEM) image of a nanowire cross-section, acquired using the focused ion beam (FIB) cutting method, with a Pt protective layer deposited on the nanowire. (Described in [78])

In this case, the LGAA structures were created using wet etching rather than RIE to produce a planar nanowire configuration. The electrical characteristics of all four devices exhibited identical behavior. As expected, the transistor featuring the GAA configuration demonstrates an improved pH response value of approximately 61 mV/pH compared to our previous report of approximately 54 mV/pH. [9] The corresponding shift of the transfer I-V curves is illustrated in Figure 3.2 (A, B). The enhanced sensitivity suggests that the surface-to-volume ratio of the GAA FET exceeded that of the planar-structured device. This implies that a greater number of proton charges reach the surface, thereby altering the potential.[79]

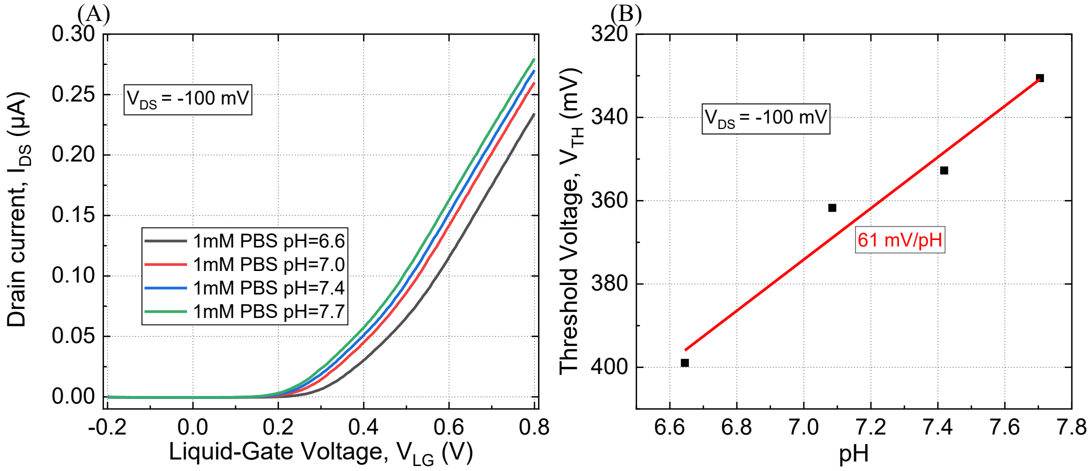

Figure 3.2 (A) Typical transfer characteristics of I_{DS} versus V_{LG} for various pH values of 1 mM PBS. (B) The V_{TH} exhibits a linear dependence on the pH values of the PBS solutions. (Described in [78])

The I-V characteristics of the GAA sensor structure were measured for different concentrations of $MgCl_2$ solutions ranging from 10^{-6} M to 1 M using an in-house developed system. It is worth mentioning that the leakage current was insignificantly low, at the nA currents level. A set of transistors, each with a length of 2 μm and varying widths (100 nm, 150 nm, 200 nm, and 300 nm), were analyzed. The findings of the examination of multiple transistors with channels of different sizes exhibited consistent patterns. Figure 3.3 (A) displays the typical transfer characteristics I_{DS}-V_{LG} of the liquid-gated NW FET measured in $MgCl_2$ solutions at V_{DS} = -100 mV for the nanowire channel with a width of 100 nm and a length of 2 μm. It is important to emphasize that the behavior of the transfer characteristics is typical for high-quality NW FET structures and is consistent with the common description of I_{DS} as a function of V_{LG} using formula (1.6).

I_{DS} decreased as the concentration of $MgCl_2$ increased. Essentially, the solid-liquid interface is altered when positive Mg^{2+} ions reach the nanowire surface. With higher concentrations of $MgCl_2$ solutions, the ion density in the solution also increased. Consequently, this alters the interaction processes of solution ions with the gate oxide surface, resulting in changes in surface charge density and electrical potential at the Si/SiO_2 interface. In turn, this affects the channel conductance and flow of the drain current. Figure 3.3 (B) shows the transfer characteristics on a semi-logarithmic scale, which is typical for field-effect transistors. This illustrates the effective control of current in the nano-channel through the application of a liquid gate voltage. The subthreshold slope was estimated to be approximately 72 mV/dec for all I-V curves of the transistor. Mobility of holes in GAA NW FET was estimated to be $\mu_p = 150$ $cm^2/V/s$ using equation for long-channel FETs at low drain-source voltage.[80] This value reflects the high-quality of liquid-gated nanowire devices. It is worth noting that the contact resistance, estimated using the transmission line model,[81] has a negligibly small value (approximately 4 kΩ after rapid thermal annealing), corresponding to about 1.2% of the total resistance of a GAA FET.

Figure 3.3 (C) illustrates the V_{TH} values, indicating the change in surface potential of the sensor in relation to molar ion concentration measured within the range of 10^{-6} M to 10^{0} M, which aligns with the previous publication. [65] The dependence exhibits slight variations from the linearly approximated segment within the range of 10^{-6} M to 10^{-1} M, showcasing a sensor sensitivity of approximately 41 mV/decade with a tendency towards saturation as the $MgCl_2$ concentration approaches approximately 0.1 M.

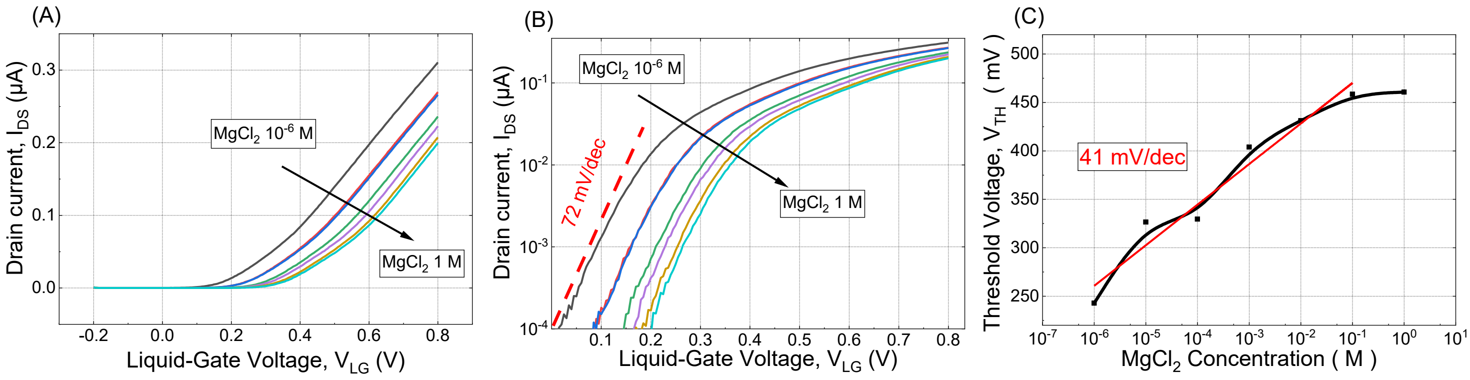

Figure 3.3 (A) Typical transfer characteristics of I_{DS}-V_{LG} for a GAA nanowire FET with a length of 2 μm and a width of 100 nm, measured in different concentrations of $MgCl_2$ solutions at V_{DS} = -100 mV. (B) The transfer I_{DS}-V_{LG} curves from (A), displayed on a semilogarithmic scale. (C) The V_{TH} extracted from (A) as a function of concentration in $MgCl_2$ solutions. (Described in [78])

Typically, the concentration of ions in the $MgCl_2$ solution dictates the quantity of ions that can be absorbed onto the gate oxide surface. Elevated ion concentrations result in heightened modulation of the surface charge, consequently inducing a more pronounced shift in V_{TH}. This implicit relationship between V_{TH} and the $MgCl_2$ $MgCl_2$ concentration can be observed as follows:

$$V_{TH} = V_{DS} - \psi_0(c_{MgCl2}) + \chi^{lq} - \frac{W_{si}}{q} - \frac{Q_{ox} + Q_{ss}}{C_{ox}} \tag{3.1}$$

where $\psi_0(c_{MgCl2})$ is surface potential modulated by concentration of $MgCl_2$, χ^{lq} is the surface dipole potential of the solution, W_{si} is the effect of the work function in the silicon layer, q is the elementary charge, Q_{ox} is the fixed charges in the oxide, Q_{ss} is the fixed charges at the oxide Si interface, and C_{ox} is the capacitance of gate oxide layer.

3.3 Surface charge characterization in GAA FETs

We conducted corresponding capacitance measurements of $MgCl_2$, which aligned well with this pattern. To gain further insight into the behavior of the double-layer capacitance, we examined a flat structure sample comprising Al/Si/20 nm SiO_2 using capacitance measurements across various concentrations of $MgCl_2$ solutions at a frequency of 1000 Hz, as depicted in Figure 3.4 (A). A shift was observed in all C-V curves with respect to $MgCl_2$ concentration. Furthermore, the minimum capacitance value (depicted as a valley in the C-V curve) was examined and found to occur within a voltage range of 0 V to 1 V, as illustrated in Figure 3.4 (B). The relationship exhibits a pattern similar to that of the dimensionless Hooge parameter (refer to Figure 3.6). These findings effectively validate the occurrence of the charge inversion phenomenon at the solid-liquid interface and lend support to the correlations mechanism in solutions containing charged ions. Subsequently, Figure 3.4 (C) illustrates the V_{FB} fluctuating between 0 mV and -200 mV, derived from the respective C-V curves using the Mott-Schottky plot, wherein the intersection of the linear portion of the ($1/C^2$) dependency with the voltage axis is identified. The figure distinctly displays two characteristic points at concentrations of 10^{-4} M and 10^{-1} M. It is noteworthy that at a concentration of 10^{-4} M, the flat-band voltage approaches zero voltage. This also indicates a significant correlation between the positive and negative contributors near the interface, resulting in a low value of the dimensionless Hooge parameter. It is important to emphasize that the observed behavior in the threshold voltage (Figure 3.3 (C)) exhibits a strong correlation with the data obtained for the dimensionless Hooge parameter (Figure 3.6).

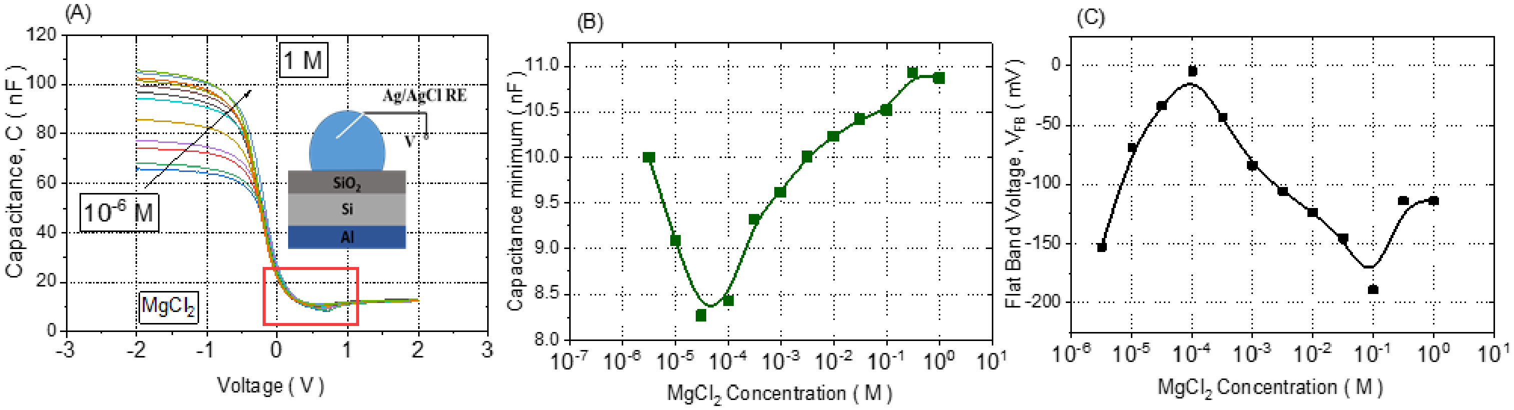

Figure 3.4 (A) Typical C-V dependencies for different concentrations of $MgCl_2$. The bottom of the right insert displays the structure of C-V samples. (B) Minimum capacitance in the voltage range between 0 V and 1 V. The data were extracted from the red rectangular area shown in Figure 3.4 (A). (C) V_{FB} as a function of $MgCl_2$ concentration. (Described in [78])

Further exploration of the charge inversion phenomenon at the interface between the nanowire channel and fluid involved examining the behavior of Mg and Cl ions in the electrolyte. Typically, when a charged molecule is immersed in a liquid environment containing various ions, Coulombic forces influence the interaction between the charged ion and oppositely charged ions (counterions) present in the electrolyte.[9] Initially, when a divalent ion approaches the neutral surface, the adsorbed ions are repelled, leading to a correlation hole effect.[61] Hence, the ions' behavior at the surface induces a negative chemical potential by attracting more counterions to the surface. This indicates the occurrence of charge inversion at a critical concentration of 10^{-4} M. Various phases of the alteration in charge states are depicted schematically in Figure 3.5 (A-D).

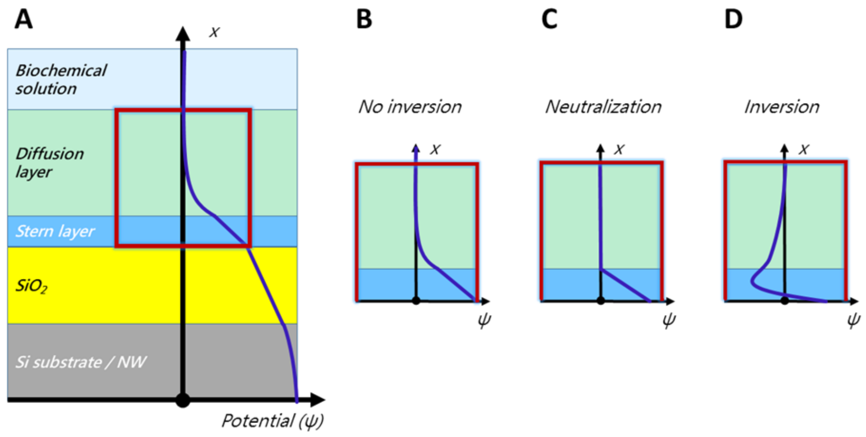

Figure 3.5 (A) Schematic illustration of potential distribution at solid-liquid interface for Si/SiO_2/liquid structures. This is depicted in both Si NW FETs and liquid-gated capacitance-voltage flat structures. It illustrates the formation of the electric double layer and the diffusion layer in the liquid under study. For divalent $MgCl_2$ solutions, three scenarios are considered: (B) no inversion; (C) neutralization; (D) inversion of the charge state at the solid-liquid interface. (Described in [78])

At low concentrations of $MgCl_2$ solution, the potential exhibits a monotonic decrease (Figure 3.5 (B)), resembling the behavior observed in solutions containing monovalent ions. However, as the concentration increased, the presence of counter ions [60] led to the neutralization of the surface charge (Figure 3.5 (C)) , followed by the inversion of surface potential (Figure 3.5 (D)), resulting in a reversible change in charge on the surface of the nanowire channel. This phenomenon of charge inversion has been documented in $MgCl_2$ solutions investigated in microfluidic channels [59] with small diameters. With increasing distance from the solid/liquid interface of the GAA FET, the potential redistribution did not follow a monotonous trend. Instead, it exhibited a decreasing tail as a result of ion diffusion.

3.4 Peculiarities registered in noise spectra of GAA FETs

When the nanowire size diminishes, traditional electrical characterization encounters significant signal fluctuations arising not only from internal transistor factors such as built-in potential, mobility degradation, and the hot-carrier effect but also from external sources such as the surrounding media. On the nanoscale, the analysis of electrical noise and fluctuations becomes a potent and effective method for precisely extracting valuable signals from the nanodevices under examination.[9, 17, 82, 83] The predominant component of the primary noise spectrum in any device structure is typically known as 1/f noise. In structures comprising semiconductor and dielectric materials, this type of noise is commonly attributed to the interaction between the charge carriers and traps at the Si/SiO_2 interface. It is important to highlight that the exchange of carriers between the nanowire channel and dielectric layer leads to fluctuations in the surface potential, thereby affecting the I_{DS} current flowing through the nanowire channel. Additionally, various noise signals manifest in GAA FETs, particularly during sensor measurements conducted with varying applied V_{LG} across different chemical solutions. Within the liquid medium, these noise signals stem from the exchange of charge carriers at the solid/liquid interface.[84] Hence, α_H and S_U were employed to study the noise characteristics of the FET.

The dimensionless Hooge parameter α_H serves as a crucial metric for evaluating transistor performance. Typically ranging between 10^{-2} and 10^{-6}, its value is indicative of device quality. In Figure 3.6, all data points fall below 10^{-3}, indicating a high-quality device consistent with previously reported values.[65, 81, 85] In this study, we employed α_H parameters acquired under various $MgCl_2$ concentrations with fixed voltages: V_{DS}= -20 mV and V_{LG}= -0.4 V, to delve deeper into the noise characteristics of GAA FETs relative to concentration. This trend reveals a decrease in α_H with increasing concentration, reaching its nadir at 10^{-4} M $MgCl_2$. Following this concentration level, α_H begins to rise, peaking at a value of 9.7×10^{-4} at a solution concentration of 10^{-1} M before declining again. Unlike monovalent ions such as K^+

and Na^+, divalent ions like Mg^{2+} may demonstrate a charge inversion phenomenon at the solid-liquid interface within a microfluidic environment filled with a solution.[75] We observed this effect in GAA FET devices filled with $MgCl_2$ solutions of moderate concentrations, indicated by a transition region (Figure 3.6) between low and high concentration solutions.

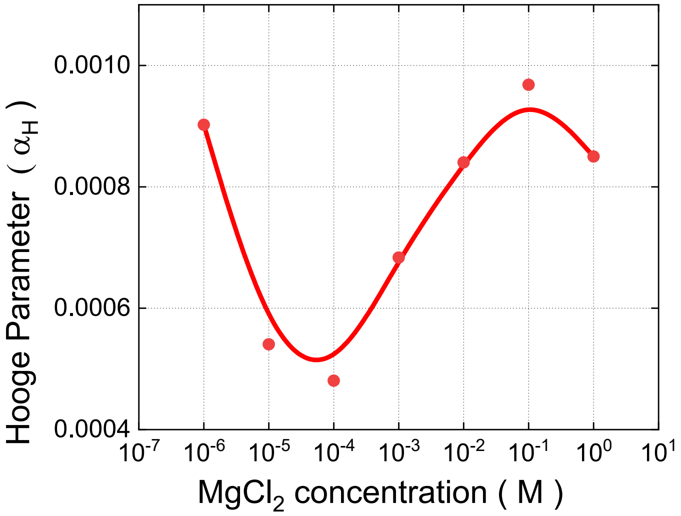

Figure 3.6 The Hooge parameter at 10 Hz was derived from the noise spectrum obtained from a GAA NW FET. The device had dimensions of 2 μm in length and 100 nm in width, with a V_{LG} of -0.4 V and V_{DS} of -20 mV. The measurement was conducted at a frequency of 10 Hz in various concentrations of $MgCl_2$ solution. A solid red curve was included as a visual reference. (Described in [78])

Two distinct regions were observed in the solutions containing varying concentrations of $MgCl_2$: the conductivity exhibited minor changes at low concentrations but increased proportionally at higher concentrations. The critical concentration observed in the 10^{-4} M $MgCl_2$ solution can be determined by examining the ion composition near the solid-liquid interface. Surface charge processes significantly affect the noise fluctuations of GAA FETs when the $MgCl_2$ concentration is below the critical level, indicating a minimal occurrence of the charge inversion phenomenon on the solid surface. After reaching the critical concentration, which coincides with the concentration-dependent conductivity, the conductivity of the divalent Mg^{2+} ions increases. This phenomenon explains the valley observed at a solution concentration of 10^{-4} M in Figure 3.6. An interesting observation was made where α_H reached its peak value at 10^{-1} M $MgCl_2$ due to the decrease in $MgCl_2$ conductivity at high concentration ranges.

The equivalent input noise, S_U, was calculated to analyze the dielectric layer-liquid interface. The presence of ions led to a notable increase in input-referred noise. Some subtle distinctions compared with the McWhorter model [82] arise because of the ion dynamic process from the solution side to reach the transistor surface. It is worth noting that the impact of V_{DS} on input-referred noise was negligible throughout this process. Usually, detectable current fluctuations in the biosensor channel are induced by a small flow of ions. In previous experiments, we observed that the amplitude and behavior of the input-referred noise increased in the bio-liquid containing troponin molecules, providing further validation of ion kinetic changes.[9] Meanwhile, we observed a slight correlation between the level of noise and the concentration of ions in a liquid environment. [86] Figure 3.7 illustrates that the S_U decreases with an increase of V_{LG} in a 10^{-3} M $MgCl_2$ under the measurement condition of V_{DS} = -20 mV. The decreasing trend of S_U reflects the effectiveness of additional V_{LG} in controlling the behavior of ions near the nanochannel surface. This indicates that the charged ions adhering to the nanowire surface not only impact the surface potential, but also alter the ion kinetics at the solid-liquid interface. Hence, it can be concluded that the sensitivity of noise characteristics can serve as a valuable tool for analyzing the dynamic behavior of ions in the tested solution, thereby enhancing the amplification of useful signals in the nanochannel compared to conventional current characterization methods. More detailed equations can be found in the subsequent statistical analysis section.

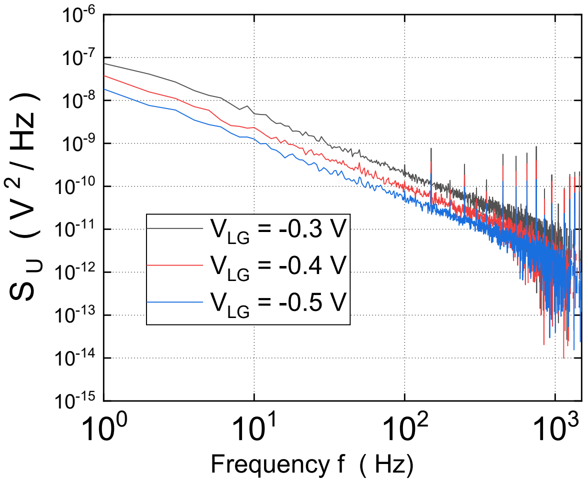

Figure 3.7. The equivalent input noise spectra S_U were recorded for $MgCl_2$ solutions with a concentration of 10^{-3} M, with varying V_{LG}. The measurements were conducted under a fixed condition of V_{DS} = -20 mV. (Described in [78])

The charge inversion phenomenon discussed above at the critical concentration of the solid-liquid interface can also be observed in the noise spectra depicted in Figure 3.8. A similar tendency was observed in the frequency dependencies of S_U measured under the same conditions V_{LG} = -0.4 V and within the range of $MgCl_2$ concentrations for two values of V_{DS}: (A) -20 mV and (B) -50 mV. It is apparent that in both Figure 3.8 (A) and 8 (B), the noise level of the S_U is within approximately the same magnitude range between 10^{-9} V^2/Hz and 10^{-7} V^2/Hz at frequencies below 10 Hz. Additionally, as the concentration of $MgCl_2$ increased, the intensity of S_U initially decreased within the range of 10^{-6} M to 10^{-4} M, then increases from 10^{-4} M to 10^{-1} M, before decreasing again. As expected, the lowest and highest S_U values were observed at $MgCl_2$ concentrations of 10^{-4} M and 10^{-1} M, respectively. This observation aligns well with the charge inversion phenomenon discussed above at the critical concentration interface. We also examined the fluctuation of the S_U at various V_{DS} values and observed that at lower voltages, the noise spectra were more susceptible to external signal interference, particularly in the frequency range of 100 Hz to 1000 Hz. Extracting valuable signals at lower V_{DS} values can be achieved by subtracting the dominant thermal noise values at high frequencies, as described in equation (3.2) in section "Statistical Analysis" below: $S_v(f > 1kHz) \approx 4KTR_{eq}$.

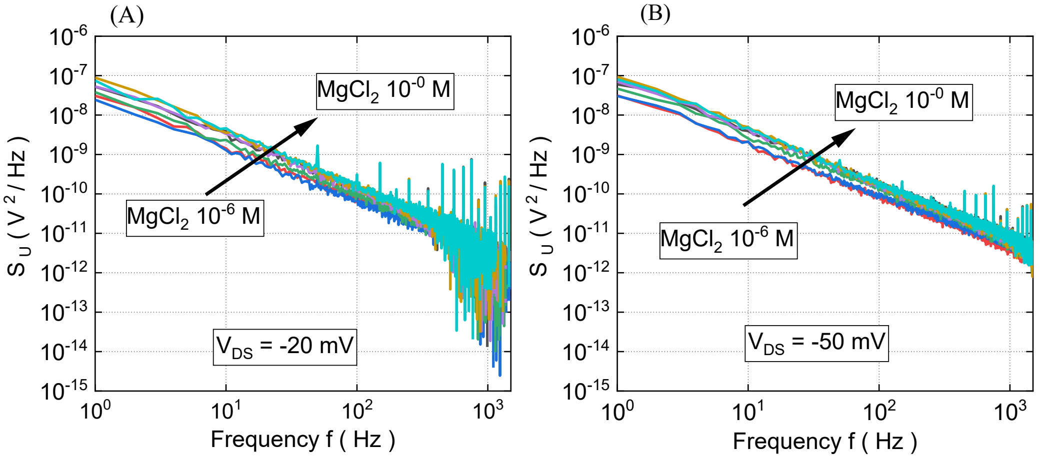

Figure 3.8 The input-referred noise spectra S_U were obtained from noise measurements of NW FETs featuring a nanowire channel measuring 2 µm in length and 100 nm in width. These measurements were conducted across various $MgCl_2$ solutions, including concentrations of 10^{-6} M, 10^{-5} M, 10^{-4} M, 10^{-3} M, 10^{-2} M, 10^{-1} M, and 1 M. The measurements were performed at a fixed V_{LG} of -0.4 V and at different drain-source voltages: (A) V_{DS} = -20 mV. (B) V_{DS} = -50 mV. (Described in [78])

To examine the behavior of ions at the solid-liquid interface, the noise level at 10 Hz points was extracted from the S_U spectra. Figure 3.9 (A) illustrates the S_U curves at 10 Hz with varying V_{LG} voltages, denoted as -0.3 V, -0.4 V, and -0.5 V, respectively. Each curve exhibits two turning points at concentrations of 10^{-4} M and 10^{-1} M, indicating a conductivity shift of the divalent Mg^{2+} ions at the critical concentration, as previously discussed. However, the S_U undergoes significant changes with an increase in V_{LG} voltage. This can be reasonably explained by the decrease in ion mobility resulting from Coulombic forces pushing ions towards the solid-liquid interface owing to an applied gate voltage on the surface of the nanowire. An interesting phenomenon is depicted in Figure 3.9 (B) (the dependence of S_U

values on V_{LG} for all concentrations of $MgCl_2$ solutions). This demonstrates that S_U decreases with increasing V_{LG}, reflecting the ability to control the interaction processes through surface Coulombic forces.

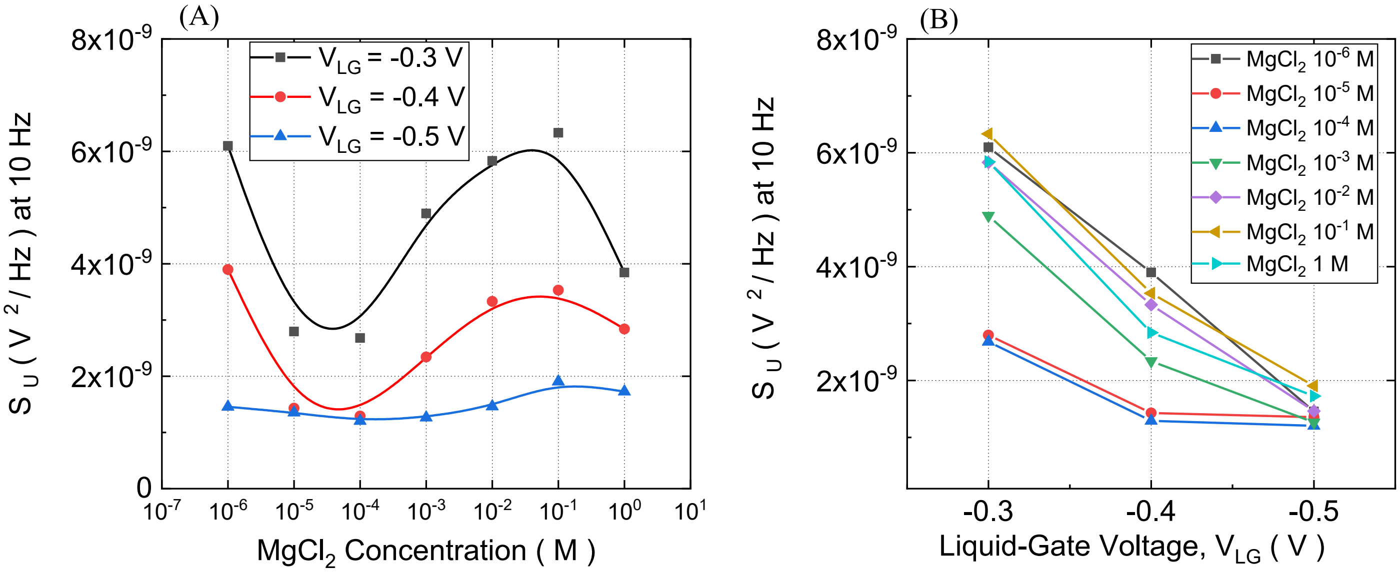

Figure 3.9 (A) The input-referred noise S_U at 10 Hz was measured for NW FETs featuring a nanowire channel measuring 2 µm in length and 100 nm in width. The measurements were conducted across various $MgCl_2$ solutions at a fixed V_{DS} = -20 mV. (B) The dependence of S_U on the V_{LG} is illustrated. (Described in [78])

The equivalent input noise S_U, recalculated from the originally measured noise spectra, is depends on the overdrive voltage V_{LG}-V_{TH} in different $MgCl_2$ solutions (Figure 3.10).

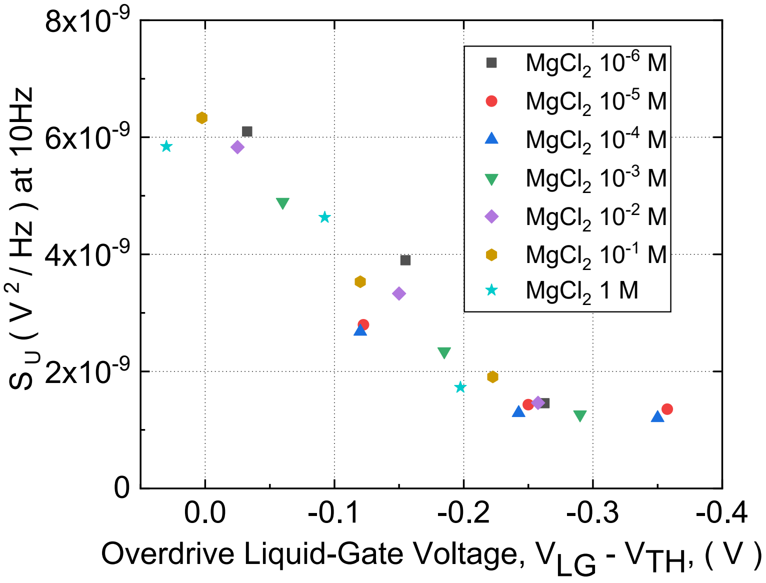

Figure 3.10. A graph illustrating the input-referred noise S_U at 10 Hz for various obtained V_{LG} across different concentrations of $MgCl_2$, plotted against the overdrive voltage (V_{LG}-V_{TH}), with a fixed V_{DS} of -20 mV. (Described in [78])

The S_U intensities exhibit a strong dependence and follow a decreasing trend with increasing overdrive voltage. This phenomenon cannot be attributed to fluctuations caused by traps in the SiO_2 layer. If channel noise were determined by charge fluctuations at the Si/SiO_2 interface, the value of S_U would remain unchanged.[87] The variation in capacitance of the structure (Figure 3.4 (B)) also cannot account for the alteration in S_U, given that S_U changes by a factor of 6, while the capacitance of the structure fluctuates within ±15%. Hence, this dependence of S_U (V_{LG}-V_{TH}) is associated with charge fluctuations at the Si/electrolyte interface, namely fluctuations in the ion concentration near the surface of the sub-gate dielectric. With an increase in the electric field within the interface layer of the electrolyte, ion mobility declines owing to heightened interactions along parallel pathways involving ions and charged channel carriers. Consequently, the accompanying reduction in noise attributed to mobile ions aligns well with the observed trend of decreasing S_U results relative to overdrive voltage, as reported in our prior publication detailing the binding of troponin antigen molecules on the surface.[9] This finding suggests that the variations and conduct of S_U within the charged ion solution provide additional support for alterations in the ion dynamics. Furthermore, the source of this noise was reinforced by the significant correlation between S_U values and the concentration of $MgCl_2$ (Figure 3.9). These noise features offer a promising avenue for exploring ion dynamics and the correlation between ions at the interface of a dielectric membrane within a biological liquid environment.

3.5 Statistical analysis

A series of FETs were analyzed to assess their electrical characteristics and noise behavior. An I-V system was employed to examine the transfer and output curves of the electrical properties. Noise spectral analysis was conducted using multiple nanowire biosensors, each measuring 100 nm wide and 2 μm long. The initial noise data consist of the voltage spectral density, $S_v(f)$, measured across varying frequencies:

$$S_v(f) = \lim_{\Delta f \to 0} \frac{(v - \bar{v})^2}{\Delta f} \tag{3.2}$$

where the mean square voltage fluctuation is $(v-\bar{v})^2$ in Δf of the frequency band.

The thermal noise resulting from the thermal excitation of the charge carriers and thermodynamic fluctuations was considered. The voltage variance per hertz of the bandwidth for thermal noise is given by:

$$S_{Thermal}(f) = 4KTR_{eq} \tag{3.3}$$

where K is the Boltzmann constant, T is the nonzero temperature, and R_{eq} is the equivalent resistance.

The spectrum of thermal noise was subtracted from the measured noise spectrum, and the formula for the analyzed portion of the noise is as follows:

$$S_{v,real}(f) = S_v(f) - 4KTR_{eq} \tag{3.4}$$

For further analysis, the spectral density of current fluctuation is adjusted using the following formula:

$$S_I(f) = \frac{S_{v,real}(f)}{R_{eq}^2}\left[\frac{1}{1+\left(\frac{f}{f_0}\right)^2}\right]^{-1} \tag{3.5}$$

where f_0 is the corner frequency which results from the presence of parasitic capacitance shunting the input of the preamplifier.

Usually, the dimensionless Hooge parameter is employed to assess the noise level for evaluating the performance of a sample, using the following formula:

$$\alpha_H(f) = \frac{S_I(f)}{V_{DS}^2}\frac{fL^2R}{q\mu_p} \tag{3.6}$$

where L is the length of the nanochannel, R is the resistance of the device, q is the elementary charge, and μ_p is the mobility of the major carrier (i.e. hole).

For additional discussion, the input-referred noise, S_U, was computed to depict the ion correlation at the liquid/solid interface across varying V_{LG} values, as follows:

$$S_U(f) = \frac{S_I(f)}{g_m^2} \tag{3.7}$$

where g_m represents the transconductance of the sample obtained from the measured transfer characteristics (I-V).

3.6 Summary

In summary, liquid gate-all-around nanowire FET sensors were developed to investigate the ion behavior at the interface between a dielectric layer covering a nanowire channel and $MgCl_2$ solutions by employing electrical and noise characterization methods. A series of noise characteristics indicated charge inversion with divalent Mg^{2+} ions at a critical concentration of 10^{-4} M. Both the Hooge parameter α_H and the equivalent input noise S_U illustrated an increase in conductivity within the solution concentration range of 10^{-4} M to 10^{-1} M. These findings align well with the results obtained using the C-V technique. The integration of noise spectroscopy offers opportunities for analyzing the dynamic processes of divalent and multivalent ions, as well as ion-ion correlation effects at the solid-liquid interface, particularly in biosensing applications.

4. SCLC effect revealed in LGAA NW FET Biosensors

We developed high-quality LGAA Si NW FET biosensors and examined their characteristics in a 1 mM PBS solution with pH = 7.4 using both transport and noise spectroscopy techniques. In the low V_{DS} regime, the conventional FET behavior displays a linear dependence on the output current-voltage ($I\text{-}V^M$) characteristics with an exponent M = 1. As V_{DS} exceeds 0.6 V, the I-V characteristics exhibit stronger power-law behavior with an exponent M. It was demonstrated that for small liquid gate voltages, the current in LGAA NW FETs follows a power-law dependence with an exponent of M = 4. Transport and noise spectroscopy analyses revealed that these findings can be attributed to the SCLC effect. Additionally, a pronounced two-level RTS was detected in the SCLC region at V_{DS} values above 0.6 V. This RTS, associated with single trap phenomena, manifests as a well-defined Lorentzian component in the noise spectra. These results indicate a correlation between SCLC and the two-level RTS phenomenon, underscoring their importance in the development of single-trap-based devices, including biosensors.

4.1 The SCLC effect features in device structure

The utilization of nanoscale biosensors across various domains has garnered increasing interest among researchers. NW FET sensors offer distinct advantages such as ultrahigh sensitivity and label-free sensing. These attributes enable the detection of diverse diseases, contributing significantly to disease prevention efforts and maintenance of human health.[3, 17, 56, 64, 88] To achieve dependable detection outcomes, the research community is actively advancing the technology for NW FET fabrication and striving to pinpoint precise parameters for analyzing test data. Valuable insights can indeed be obtained from the dynamic processes of ions at the liquid/solid interface under varying applied voltages during the measurements.[54, 62] Studying the peculiarities of the charge carrier behavior in physiological liquids is imperative to establish a high-performance operational regime for FET biosensors.[33, 63] For various applications, a detailed investigation of the SCLC and RTS induced by a trap near the nano-channel is essential. [17, 58, 68, 69, 85] The characteristic times associated with RTS are shown to be new parameters that should be considered to achieve enhanced sensitivity in biosensing applications.[5, 17, 81]

The SCLC regime is important in governing the carrier transport within NW FET structures, as has been extensively discussed in various reports. This regime has been identified in nano-channel structures composed of GaN, InAs, CdS, ZnO, and GaAs.[66-70] Typically, the SCLC phenomenon occurs because of variations in the concentration of charge carriers within the nanowires, changes in the concentration of active charge traps, or the decreased density of carriers in thermal equilibrium. This effect significantly affects the electrical properties of FET structures, resulting in superlinear behavior of the I-V curve, as described by the Mott-Gurney law. This law states that the current is proportional to the voltage raised to a power of 2, [66, 89-91] as observed in bulk materials, films, nanoribbons, and nanowire samples. The SCLC phenomenon not only affects the static electrical characteristics of transistors but also impacts the dynamic noise properties of devices.[65]

To analyze the SCLC effect, it is essential to consider the slope of the output I-V curve when plotted in double-logarithmic coordinates. Typically, a slope of approximately 1 suggests a linear ohmic behavior in a low-bias regime. Subsequently, a slope greater than or equal to 2 indicated the onset of the nonlinear SCLC regime. It has been demonstrated [16] that a slope of approximately 2 indicates the absence of active traps in the semiconductor or the presence of a single discrete trap level. However, a slope greater than 2 is attributed to the distribution of partially occupied trap states across a range of energies. Yu et al. discovered in their study on GaSb nanowire transistors that the slope of the I-V curve altered from 3.8 to 1.9 following annealing. This change was attributed to the occurrence of SCLC when the number of injected carriers exceeded that of the thermally generated carriers.[92] They demonstrated that thermally generated carriers govern the conduction, thereby mitigating the SCLC effect. Pehrsson et al. were the first to report on the conduction mechanism associated with SCLC in heterostructure nanowires, exhibiting an output I-V characteristic slope of 3.1 when plotted on logarithmic scales for analyzing the traps within the structure.[93] Furthermore, the results indicated that the traps were distributed across a range of energy levels and did not accumulate near a single energy level.

Noise spectroscopy serves as a potent technique for assessing transistor performance. Guo et al. utilized noise spectra analysis to show a distinct transition behavior from 1/f to $1/f^{1.5}$. This transition confirms the occurrence of the SCLC effect in biosensors, which reflects the dynamic processes of ions at the liquid/solid interface.[65] In nanoscale NW FETs, the presence of a Lorentzian component in the noise characteristics may correspond to RTS owing to the STP. Kutovyi et al. suggested that parameters associated with the RTS, observed as a consequence of a single trap capturing and emitting charge carriers near the Si/SiO_2 interface, could offer a novel approach. As the capture time to the trap is highly sensitive to alterations in the surface potential, this enables a notable enhancement in biosensor sensitivity compared to the conventional approach that relies on changes in the threshold voltage. [17] Hence, investigations into the parameters of STP in silicon nanowire-based biosensors exhibit significant potential for the development of single-trap-based devices and their utilization across diverse research domains, particularly in biomedical applications.

In this chapter, LGAA FETs were fabricated by employing NW channels 2 µm in length and 150 nm in width. The silicon NW channels were fabricated using SOI wafers with an impurity concentration of 1×10^{15} cm^{-3}. To obtain ohmic contacts, the source and drain regions were implanted with boron atoms (energy 6 keV, dose 1×10^{15} cm^{-2}), resulting in p-type transistor structures (P++-P-P++). The contact resistance, estimated using the transmission line model, [94] was found to be negligibly small (approximately 4 kΩ), corresponding to about 1.2 % of the total resistance of a GAA FET. The NW FETs were investigated in 1 mM PBS at pH = 7.4. Based on our experimental findings, the transistor current consists of the typical FET current component ($I \sim V^{M}$), where M = 1 and the SCLC-induced current components where M > 1. The SCLC-induced current observed at $|V_{DS}| > 0.6$ V was systematically analyzed in LGAA NW FETs using measured I-V curves, noise spectroscopy, and RTS fluctuations as a result of STP.

4.2 Transport and noise properties of LGAA NW FET

A schematic depiction of the LGAA NW FET devices investigated in this study is illustrated in Figure 4.1 (A). The I-V characteristics and noise spectra of LGAA NW FET were measured at different V_{DS} and different V_{LG} in 1 mM PBS solution. By utilizing a FIB cut, as depicted in Figure 4.2 (B), the free-standing state of the nanowire was confirmed, and the diameter of the NW channel was determined to be approximately 150 nm. It is important to note that for FIB cut studies, the nanowires were coated with a thin layer of Pt.

4.2.1 Deviation from standard behaviour in I-V characteristics of LGAA NW FETs

The typical output characteristics measured for the LGAA NW FET at low voltages ($|V_{DS}| <$ 0.6 V) are illustrated in Figure 4.1 (C). At low voltages, a conventional I-V characteristic for the NW FET was observed, featuring the linear behavior $I \sim V^M$, where M is equal to 1, followed by the saturation region. The conventional I_{DS} as a function of both the V_{LG} and V_{DS} of FET device was fitted in various operational regions using the Equation (1.6) mentioned in the previous chapter. The I_{DS} behavior results align well with I-V as described by equation (1.6). It is noteworthy that the output I-V curves exhibit symmetric with respect to the point $V_{DS} = 0V$, $I_{DS} = 0$ A, within the range from -0.1 V to 0.1 V, indicating well-fabricated ohmic contacts. Figure 4.1 (D) illustrates the typical fitted I-V characteristics obtained for several liquid-gate voltages. The fitting parameters are listed in Table 4.1.

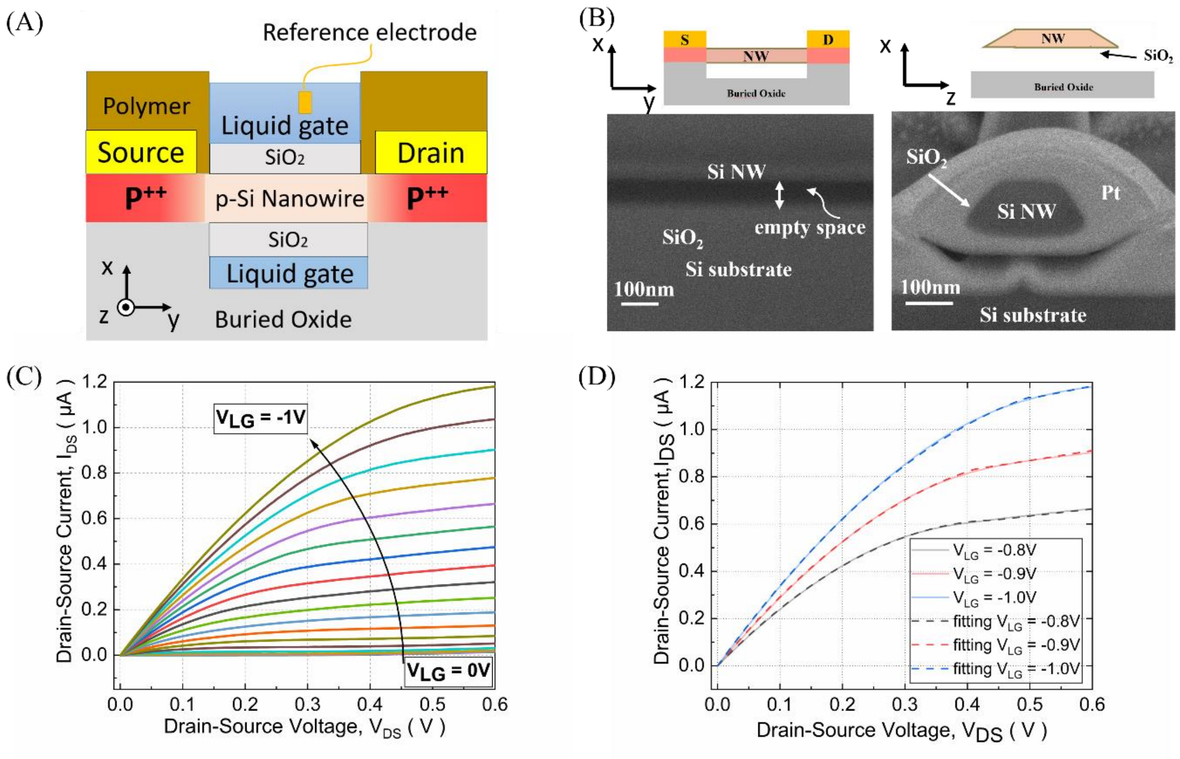

Figure 4.1. (A) A schematic representation showing the cross-section view of a LGAA NW FET. (B) A FIB cut image displaying the cross-section size of fabricated GAA nanowires, with insets illustrating schematic GAA FET post-fabrication, before introducing the liquid volume. (C) Typical output I-V characteristics obtained for a nanowire measuring 2 μm in length and 150 nm in width, in a 1 mM PBS

solution with pH = 7.4. The measurements were taken at ($|V_{DS}| < 0.6$ V) and $V_{LG} > V_{TH}$, with V_{LG} ranging from 0 V to -1 V at intervals of 50 mV. (D) The calculated I-V characteristics, derived from equation (1.6), confirm the conventional behavior observed in the measured output characteristics. The fitting parameters are listed in the accompanying table. (Described in [95])

Table 4.1. List of fitting parameters used for the analysis of conventional I-V output characteristics of LGAA NW FET with a 2 μm long and 150 nm wide nanowire. C_{OX} = 0.0017 F/m^2; μ = 50 cm^2/Vs, extracted directly from measured transfer characteristics similar as described in.[96]

V_{LG} (V)	V_{OD} (V)	V_{TH} (V)	λ	V_{DSsat} (V)
0.80	0.45	0.35	0.48	0.43
0.90	0.55	0.35	0.48	0.55
1.00	0.65	0.35	0.48	0.65

Here, V_{OD} represents the overdrive voltage, calculated as $V_{OD} = V_{LG} - V_{TH}$.

In the output I-V characteristics, interesting features were observed at relatively high drain-source voltages ($|V_{DS}| > 0.6$ V), as depicted in Figure 4.2 (A). A noticeable growth trend is observed beyond the saturation region. The I-V curves displayed alterations in their shape and slope with increasing V_{LG}, as depicted in Figure 4.2 (B), where the output I-V characteristics are plotted in a log-log scale. This phenomenon can be attributed to the critical characteristic voltage (V_C), which delineates the point at which the I-V curves transition from linear to superlinear behavior. When the V_{LG} is below the V_C, the I-V curve follows a conventional trend and can be described using standard equations for FET devices. Conversely, when V_{LG} is exceeds V_C, the I-V curve can be divided into two segments: the conventional FET curve and the subsequent rising segment, which are easily distinguishable. The rising component of current obtained at $V_{LG} = 0$ V is denoted as I_0. Consequently, subtracting I_0 from the remaining curves yields the conventional output curves.

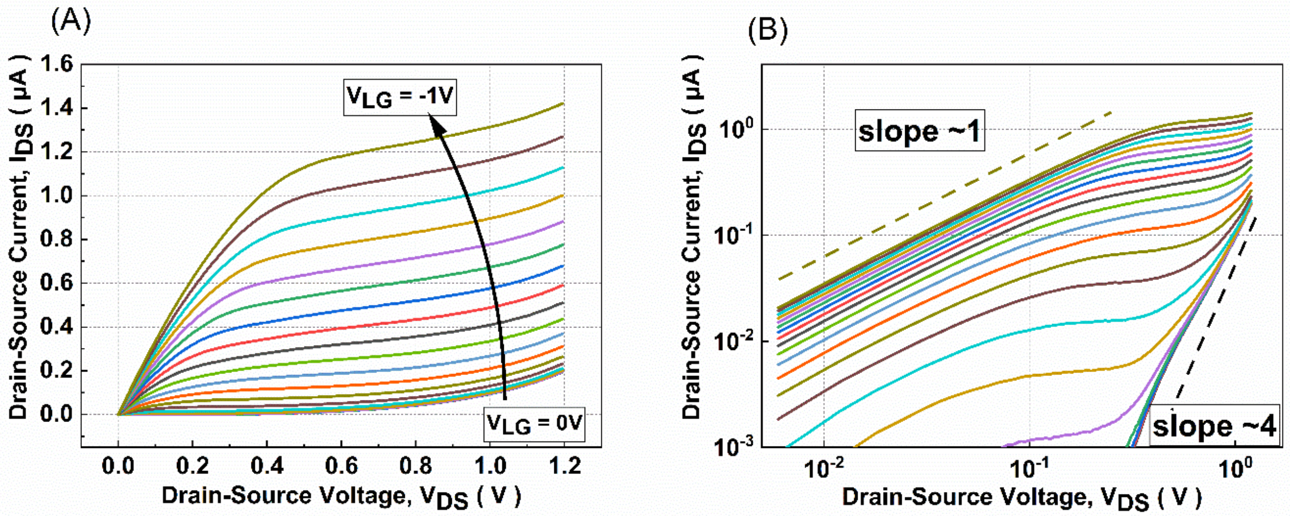

Figure 4.2. (A) Typical output I-V characteristics recorded across the entire V_{DS} range, encompassing $|V_{DS}| > 0.6$ V and $V_{LG} > V_{TH}$, obtained for a nanowire measuring 2 µm in length and 150 nm in width, immersed in a 1 mM PBS solution with pH = 7.4. The measurements were conducted with V_{LG} ranging from 0 V to -1 V at intervals of 50 mV. (B) The output I-V curves depicted in Figure 4.2 (A) exhibit two distinct slopes when plotted on a log-log scale, when slopes of 1 and 4, respectively. (Described in [95])

Analyzing the ascending segment of the output curves was facilitated by employing a double logarithmic scale for the I-V curves. Notably, when the liquid-gate voltage was zero, a significant increase in drain current was observed at a voltage of -0.4 V, exhibiting a slope of approximately 4. Typically, the I-V characteristics with a slope of 2 in bulk materials are associated with the SCLC effect. The occurrence of the SCLC effect can be attributed to carrier injection from the contact regions, not only in bulk materials but also in nanostructures, such as nanowires. The SCLC phenomenon can be described by the Mott-Gurney law [97] as follows:

$$I_D = \zeta \frac{\varepsilon \mu V_{DS}^2}{4\pi L} \tag{4.1}$$

where ζ is a coefficient typically of the order of unity, ε represents the permittivity, μ denotes the mobility of the free current carriers, and L denotes the length of the nanowire.

However, a significantly steep slope was observed in the trap-filling limit voltage regime [70]:

$$I \sim V_{DS}^{M} \tag{4.2}$$

with M significantly surpassing 2.

A. Rose discussed the SCLC effect, attributing it to the nonlinear shape of the I-V curve, which arises from traps present in insulators.[98] He illustrated that the I-V curve deviates from the ideal quadratic law and exhibits a much higher power dependence on the V_{DS}. The phenomenon of a higher power (> 2) dependence on voltage elucidated by the peculiarities in the energy distribution of the traps.[17] Saied et al. utilized the device structure composed of $Al_{0.3}Ga_{0.7}As/In_{0.15}Ga_{0.85}As/GaAs$ to investigate SCLC. They observed excess conduction under $V_{DS} > 2.5$ V and soft pinch-off at a high V_{DS} range measured at a temperature of 300 K.[99] It is noteworthy that the SCLC phenomenon can be influenced by traps [17] in the channel of the structures, leading to excess output conductance and a distinctive upward trend in the I-V curve. Typically, with an increase in V_{DS}, the traps in the nanochannel may become filled, resulting in an upward shift of the quasi-Fermi level. An evident increase in I_{DS} was demonstrated when the V_{DS} reached the trap-filling limit voltage regime. [70]

As illustrated in Figure 4.2 (B), our findings exhibit a resolved superlinear dependency on the applied voltage V_{DS}, with a slope of approximately 4. This slope is associated with the SCLC effect, as corroborated by other results. Notably, a slope exceeding 1 in the I-V curves can effectively enhance the sensitivity of LGAA NW FET biosensors [65] in the presence of the SCLC effect in the nanochannel. Meanwhile, the slope of the superlinear portion in the I-V characteristics gradually decreases from the initial value of approximately 4 as V_{LG} increases owing to the stronger contribution of the main current in the nanowire channel. Changes in V_{LG} alter the charge states on the surface of the LGAA channel, thereby influencing the interaction intensity of the nanochannel carriers with the traps. Traps in the SiO_2 layer near the Si/SiO_2 interface with a small channel diameter may contribute to the formation of a strong $I–V^M$ dependency with $M > 2$ in our NW FETs operating with a liquid gate, that is, when the nanochannel is immersed in a liquid.

4.2.2 Noise spectroscopy analysis of SCLC effect in LGAA NW FETs

Noise spectroscopy is a potent technique for analyzing trap centers in materials and devices [100]. Hence, we employed noise spectroscopy to investigate the enhanced section of the I-V characteristics associated with the SCLC effect in sensors operating in a liquid environment.

To explore the relationship between the SCLC-induced current and the dynamics attributed to traps in SiO_2 (gate oxide in contact with PBS solution) near the Si/SiO_2 interface in LGAA NW FETs, we conducted noise spectroscopy measurements in 1 mM PBS solution at pH = 7.4 under various voltages. Figure 4.3 (A) depicts the typical S_V of the drain voltage for a FET device with a nanowire length and width of 2 μm and 150 nm, respectively. The measurements were carried out at a constant V_{LG} = -0.2 V and different ranges of V_{DS} from -0.1 V to -1.2 V. Notably, a portion of the measured noise spectra corresponds to the conventional behavior of the I-V characteristics. However, noise spectra obtained for the voltage range above 0.6 V reveal additional Lorentzian peaks. This deviation in noise spectra correlates well with deviation in I-V characteristics from the linear dependence to a current proportional $I = V^M$, with $M > 1$ corresponding to the region reflecting the SCLC effect.

The Lorentzian peaks can be described by the following equation:

$$S_V(f) = \frac{S_V(0)}{1 + (2\pi f\tau)^2} \tag{4.3}$$

where $S_V(f)$ represents the voltage noise spectral density at frequency f, $S_V(0)$ denotes the same value at $f = 0$, and τ is the time constant of generation-recombination (GR) fluctuations.

By plotting S_V as a function of frequency f ((Figure 4.3 (B)), the Lorentzian component [17] can be examined by identifying its characteristic time constant in noise spectra, $S_V(f)$. In our cases, such Lorentzian peaks are well distinguished at V_{DS} values exceeding -0.6 V in the noise spectra. The time constant of GR fluctuations was estimated to be approximately 40 µs using Equation (4.3). It is worth noting that in the case of NW FET equipped with a liquid gate and a metal back gate, the channel position can be shifted away from the dielectric layer in contact with the liquid. This leads to a significant reduction in the noise level owing to alterations in the mechanisms governing the origin of noise.[101]

In nanoscale device structures, the Lorentzian peak is closely associated with RTS noise arising from the capture and emission of charge carriers by a single trap situated in the dielectric layer near the Si/SiO_2 interface. The RTS phenomenon manifests at the same voltages as the SCLC effect observed in the I-V characteristics, that is, at high V_{DS} values.

The time constant of the Lorentzian is connected to capture and emission time constants as follows:

$$\begin{cases} \tau = \dfrac{1}{2\pi f_0} \\ \dfrac{\tau_c}{\tau_e} = \dfrac{\text{Counts(capture)}}{\text{Counts(emission)}} \\ \tau = \dfrac{\tau_c \cdot \tau_e}{\tau_c + \tau_e} \end{cases} \tag{4.4}$$

where τ_c represents the capture time and τ_e denotes the emission constant in the channel of the LG NW FET structure, and f_0 is the noise corner frequency of two-level RTS from the Lorentzian-shaped data recorded via the noise system.

It is widely recognized that two-level RTS noise is an important method for investigating charge carrier dynamics in dielectric layers interfacing with liquid and STP.[58] The fluctuations of I_{DS} recorded at high values of V_{DS} using an in-house noise measurement system are depicted in Figure 4.3 (C). The amplitude of I_{DS} increases within a range of V_{DS} from -0.6 V to -1.2 V. It is noteworthy that the onset voltage was V_{DS} = -0.8 V when RTS was detected in PBS solution with pH = 7.4. This highlights the correlation between two-level RTS and the SCLC phenomena, where most of the traps are filled by carriers captured from the NW channel. Thus, the SCLC effect contributes to the relatively large amplitude of RTS at a higher negative V_{DS} (i.e. $V_{DS} < -0.6$ V).

The statistical histogram proved to be a highly effective approach analyzing two-level RTS noise. Figure 4.3 (D) shows I_{DS} histograms obtained from time traces. Two Gaussian peaks gradually become more distinguishable as V_{DS} increased. These were distinctly separated into two peaks at high voltages. These peaks correspond to the emission and capture states of the single trap.

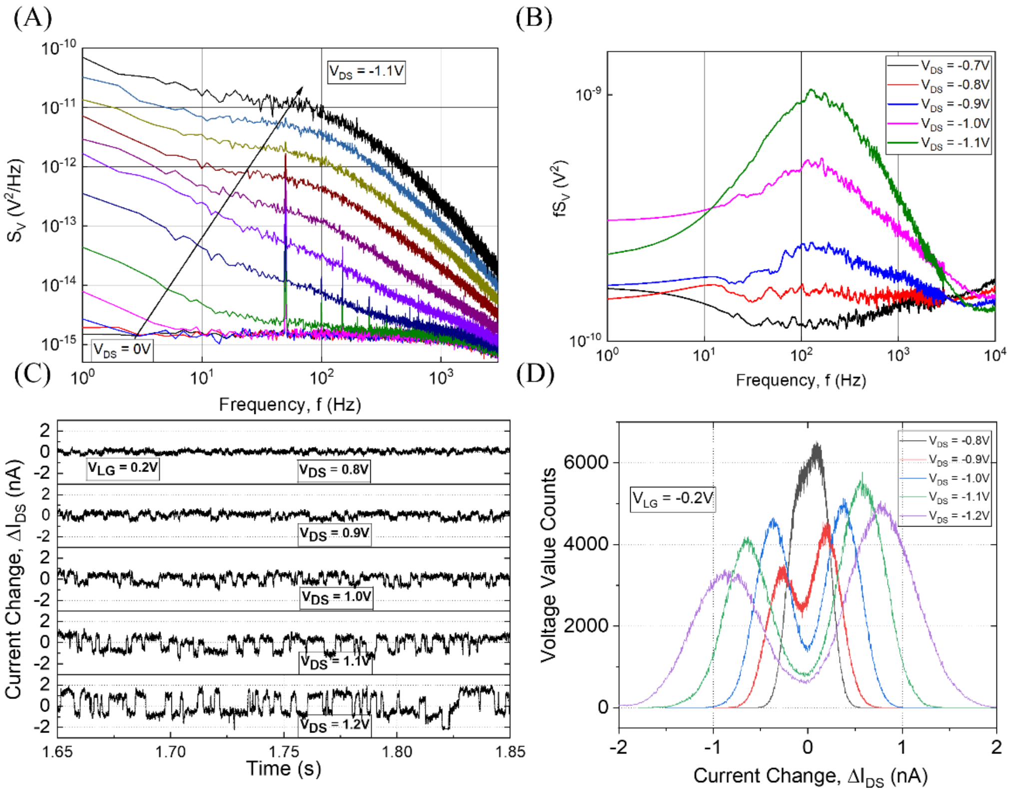

Figure 4.3. (A) The voltage spectral density measurements were conducted on a nanowire, featuring dimensions of 2 µm in length and 150 nm in width, at various V_{DS} with a step of 0.1 V, while maintaining a constant V_{LG} of -0.2 V in a PBS solution. (B) Normalized noise spectra density was observed at different V_{DS} values, with V_{LG} set to -0.2 V. Lorentzian noise components are evident at relatively high V_{DS} voltages. (C) The two-level RTS measured for a nanowire with a length of 2 µm and width of 150 nm in drain current I_{DS} are recorded at different V_{DS} at constant V_{LG} = -0.2 V. (D) Histograms generated from RTS time traces, showcasing the current amplitude, distinctly separated into Gaussian peaks due to STP. (Described in [95])

It is worth mentioning that the ratio between the capture time constant and emission time constant τ_e/τ_c represents the dimensionless parameter R. Figure 4.4 (A) illustrates the dependence of R-factor on V_{DS}, which can be converted into a function of I_{DS} (Figure 4.4 (A, B)). The R-factor changes by 30% as the V_{DS} applied to the LGAA NW FET structure increases. With an increase in V_{DS} or I_{DS}, the R-factor tends to decrease. This suggests potential accumulation of a higher concentration of charge carriers in the transistor nanochannel. The accumulation of charge in the nanowire channel may result in increased nonuniformity in the redistribution of carriers along the NW channel owing to the SCLC effect. With an increase in V_{DS}, significant charge redistribution in the nanochannel leads to an augmentation in the amplitude of the two-level RTS. This finding validates the correlation between the RTS phenomenon, and the SCLC observed for $V_{DS} = -0.6$ V.

Figure 4.4 depicts the amplitude of RTS (ΔI_{DS}) arising from the STP, derived from recorded time traces, as a function of I_{DS} currents, measured in the V_{DS} range from -0.8 V to -1.2 V at various V_{LG}. As I_{DS} current increased, all the curves exhibited a tendency to rise. This can be explained as following: the local charge density undergoes temporarily changes owing to the modulation of channel conductivity caused by an electron captured by the trap near the nanowire Si/SiO_2 interface.[58, 81, 85, 102, 103] These fluctuations in the electric field within the nanowire channel resulted in stronger I_{DS} fluctuations at large V_{DS} values.

It is important to highlight that SCLC-induced currents emerge at relatively high V_{DS}. At these voltages, the RTS phenomenon was observed in the biosensor. This suggests that the SCLC effect aids in detecting RTS at high V_{DS} voltages.

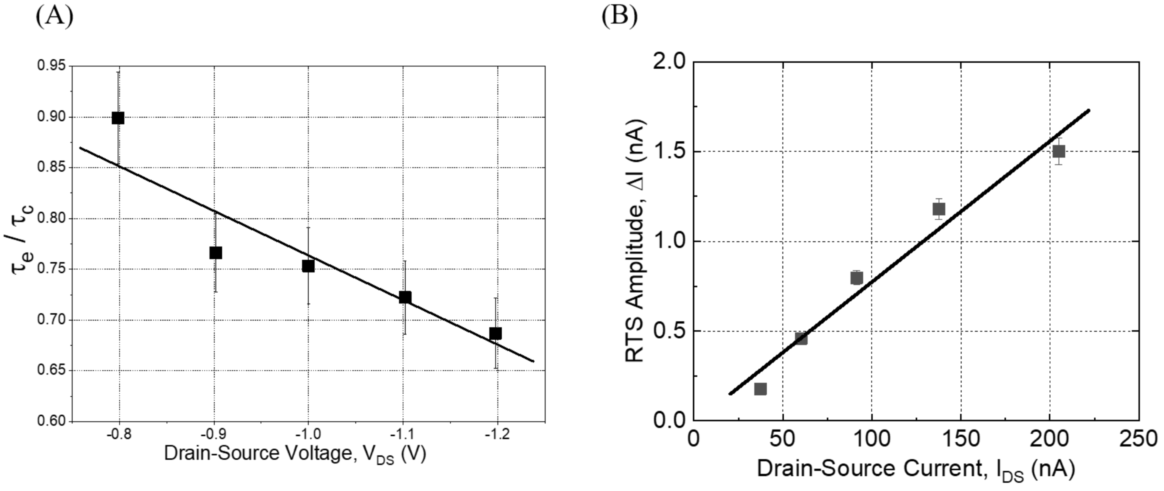

Figure 4.4. (A) Plot depicting the ratio of τ_e/τ_c against V_{DS} at a fixed V_{LG} value of -0.2 V, derived from measurements conducted on a nanowire measuring 2 µm in

length and 150 nm in width. (B) The relationship between the amplitude of RTS current and I_{DS} within the V_{DS} range of -0.8 V to -1.2 V at $V_{LG} = 0$, obtained for a nanowire measuring a 2 µm in length and 150 nm in width in a 1 mM PBS solution with a pH of 7.4. (Described in [95])

The specific characteristics of the STP-related components were scrutinized by analyzing the statistical properties of the RTS signals, as depicted in Figure 4.5.

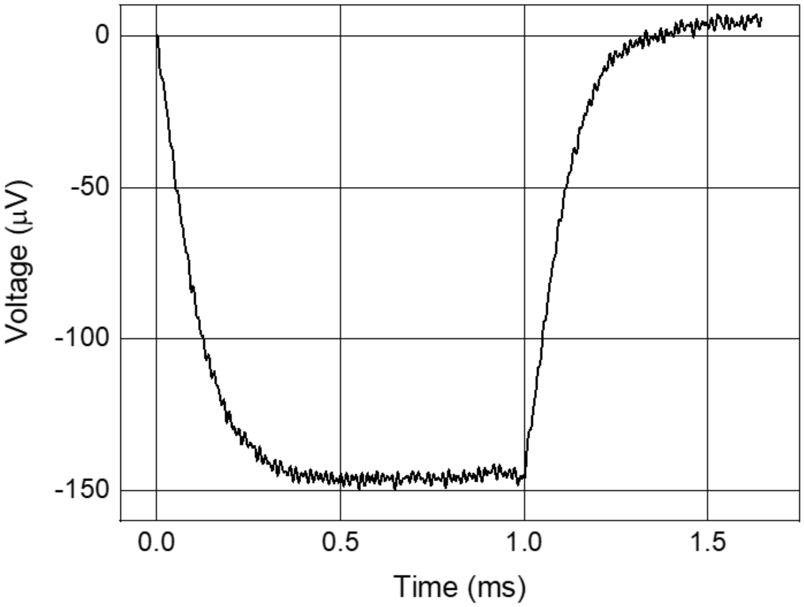

Figure 4.5. A representative time trace was generated by averaging 100 fluctuations of the RTS signal recorded for a nanowire measuring 2 µm in length and 150 nm in width at a V_{LG} of -0.2 V and a V_{DS} of -1.1 V. (Described in [95])

The data enable us to estimate the capacitance associated with the SCLC effect as follows: the relaxation time constant, τ, can be approximated by analyzing the fronts of the time trace pulses reflecting the two-level current fluctuations (Figure (4.5)) at the level of $1/e$ from the starting voltage of the pulse This value was estimated to be 113 µs. Subsequently, the capacitance of the LGAA NW FET device owing to carrier redistribution in the channel as a consequence of the SCLC effect can be estimated using the relaxation time constant as follows:

$$\tau = RC \tag{4.5}$$

where R represents the resistance of the device, which is estimated using the I-V characteristic at V_{LG} = -0.2 V and at V_{DS} = -1.1 V.

The capacitance of the LGAA NW FET was determined to be 22 pF. Here C represents the capacitance due to a single trap situated in SiO_2 layer near Si/SiO_2 interface.

Moreover, the noise characteristics serve as a valuable tool for investigating the behavior of charge carrier on the surface of a nanowire in a liquid environment. Hence, the normalized voltage spectral density S_V values corresponding to the flicker component of noise at 100 Hz, determined for different V_{LG}, were obtained using noise spectra measured in the PBS solution. Figure 4.6 illustrates S_V as a function of V_{DS} voltage, acquired at a frequency of 100 Hz, plotted on a semi-logarithmic scale. It is worth noting that the minimum level of noise (about $1.5 \cdot 10^{-15}\ \mathrm{V^2 s}$) corresponds to the thermal noise level described as Equation (3.3).

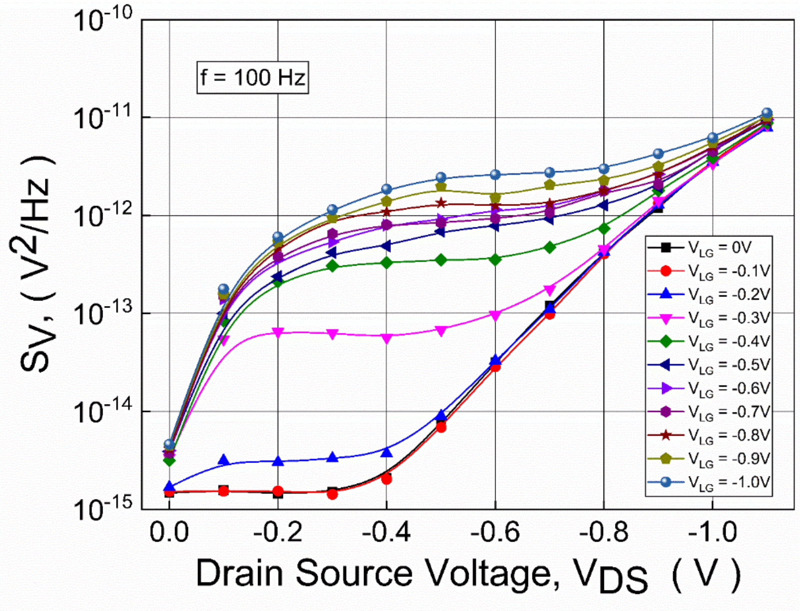

Figure 4.6. The flicker noise component, S_V, in the voltage spectral density plotted against V_{DS}, measured at 100 Hz from noise spectra recorded for a nanowire with

dimensions of 2 µm in length and 150 nm in width in a PBS solution with pH = 7.4 at various V_{LG} values. (Described in [95])

As shown in in Figure 6, the data reveal a pronounced dependence of S_V on V_{DS}, within the range of small V_{DS} values ($|V_{DS}| < 0.6$ V). However, for voltages exceeding 0.6 V, minimal changes (within one order of magnitude) were observed. The data presented in Figure 5 illustrate a significant redistribution of carriers along the channel owing to injected carriers, leading to the formation of a sharp step in carrier redistribution. This step determines the formation of capacitance, the value of which is determined to be 22 pF utilizing the exponential behavior of pulse fronts (Figure 4.5).

Additionally, when the current traverses the device nanochannel, the dynamic process of charge carriers elucidates the behavior of S_V.[9] These variations offer valuable insights into the sources of dynamic fluctuations extracted from the noise spectra. In the LGAA NW FET devices, two Lorentzian noise components were identified in the measured noise spectra. The fluctuations in two-level RTS corresponded to these Lorentzian noise components. The RTS was stimulated in the high electric field region, where the SCLC was observed. This suggests that nearly all traps are occupied, except for a single trap, which determines the RTS noise signal. The SCLC effect was observed with a slope M of approximately 3.6 in the output I-V curves on a double logarithmic scale at a high V_{DS} range from -0.6 V to -1.2 V. Consequently, the SCLC effect, which is crucial for biosensing applications, can be investigated using a novel approach represented by the RTS fluctuations and the corresponding Lorentzian components in noise spectra to identify more suitable parameters for biosensing detections. These findings underscore the importance of further exploration of the SCLC effect for the advancement of device structures and biosensor technologies.

4.3. Summary

In conclusion, our study investigated the electrical and noise characteristics of LGAA NW FET biosensors immersed in PBS solution. We observed that, at small voltages, the current behavior of the LGAA transistor conforms to conventional FET behavior. However, deviations from this behavior were noted at drain-source voltages ($|V_{DS}|$) exceeding 0.6 V. In the high V_{DS} voltage range and for small V_{LG} values, we determined the slope of the I-V characteristics to be 4 on double logarithmic scale. Our findings from the transport and noise property assessments of LGAA NW FET biosensors suggest the establishment of a transport regime indicative of the SCLC effect. Furthermore, noise measurement revealed the presence of a two-level RTS phenomenon within the same voltage range where the SCLC effect was resolved in I-V characteristics. We propose a novel approach for SCLC analysis that utilizes RTS characteristic times. Analysis of the RTS fluctuations shape enabled us to ascertain the characteristic capacitance resulting from the SCLC effect, which was estimated at 22 pF. The RTS associated with STP and noise spectroscopy offers valuable insights into the SCLC effect in LGAA NW FET. These findings are significant for the development of single-trap-based nanotransistor structures, particularly for biosensors.

5.Optical effects in LGAA FET Biosensors with Bowtie Antenna (BA)

5.1 Design and fabrication of LGAA NW FET devices with BA

In chapter 2, we extensively discuss the design and preparation process of LGAA NW FET devices. Therefore, I will not delve into the repetitive FET device preparation process; instead, the following section will focus on the components of bowtie-antenna preparation.

Considering our sample specifications, the preparation process of the bowtie-antenna should closely follow an Al metallization process, which involves annealing at 450 °C for 10 min to achieve ohmic contact. It is noteworthy that before preparing the bowtie-antenna on the SOI substrate, we conducted numerous experiments on the Si substrate in the preliminary stages to determine the process parameters. This included evaluating different resists and establishing the dose range. Ultimately, we opted for the CSAR resist, which involved spinning the sample at 4000 rpm for 45 s. Following spinning, the samples were promptly placed on a hot plate at 150 °C for 3 min. Subsequently, the heat-treated FET samples were exposed through EBL using a dose of 650 $\mu C/cm^2$ to define the shape of the bowtie-antenna. Developer AR600-546 was then used to develop FET devices after the EBL process. The next crucial step involves depositing 5 nm of Ti, typically done prior to depositing 40 nm of gold on the surface of the developed sample, to enhance the stability of the gold. Finally, the sample is immersed in acetone to remove excess metal from the surface of the FET devices through a lift-off process, followed by blowing the sample dry with nitrogen to obtain the LGGA NW FET with a bowtie-antenna. Subsequently, the passivation steps described in Chapter 2 were performed.

5.2 Light excitation on LGAA NW FET devices with BA

A high-quality bowtie antenna is implemented to enhance the efficiency of the LGAA FET device. Additionally, achieving a superior LGAA FET biosensor requires heightened attention to fabrication techniques and measurement protocols, beginning with the initial design of cleanroom preparation processes and extending to the thorough analysis of liquid/solid interactions during measurements. This is essential as significant signals typically arise from the dynamic ion processes at the liquid/solid interface.[5] The importance of investigating the conduct of charge carriers has been emphasized in many prior research endeavors. The α_H, [78, 104] the SCLC, [70, 71, 104] and the RTS [17, 95, 102] have been scrutinized to elucidate the dynamics of ions at the liquid/solid interface. Additionally, two-level RTS is pivotal in biological detection applications because it entails a solitary trap near the Si/SiO_2 interface that engages in the capture and release cycles of the charge carrier. Kutovyi et al. found that employing RTS as an innovative method led to a 300% enhancement in sensitivity compared to the conventional approach.[17]

A thorough investigation of RTS-related phenomena is warranted to improve the sensitivity of FET biosensors. Petrychuk et al. suggested that RTS manifests in nanotransistors featuring a polysilicon gate when stimulated by infrared light. [18, 19] Moreover, the biosensitivity in liquid-gated devices can be boosted by efficiently adjusting the parameters of single trap and interface phenomena through light manipulation.[105, 106] Optical radiation prompts reconfiguration in the distribution of discrete levels, enabling precise control over their energy attributes. Consequently, this can facilitate the establishment of optimal sensitivity thresholds. Pud et al. utilized a gold bowtie antenna on the sample surface to create nanopores in dielectric material via surface plasmon resonance induced by laser irradiation.[107] It was demonstrated that under high voltage conditions, the dielectric SiN layer underwent breakdown because of the hotspot of the intensified optical field at the center of the bowtie antenna induced by laser excitation. They achieved precise manipulation of the nanopore size and location and demonstrated the utility of these plasmon nanopores in analyzing single deoxyribonucleic acid (DNA) molecules traversing the pore. Our hypothesis involved employing a similar antenna-based approach to influence material structural properties using light but without inducing material damage. It is important to note that the breakdown of the dielectric material in our NW FET structures leads to leakage current and loss of biosensor functionality. Our concept aims to utilize an antenna approach to induce a minor perturbation and activate a single center to generate a two-level RTS signal with precise positioning.

5.3 FDTD Simulation of Bowtie Antenna plasmonic effect

Multiple LGAA NW FET samples were created, each featuring a Au antenna. We applied a 40 nm-thick layer of gold antenna to the surface of a 20 nm dielectric SiO_2 layer situated near the center of the nanowire. The antenna was split in the middle, with a 40 nm separation. Figure 5.1 (A) shows a schematic depiction of the examined antenna LGAA NW FET devices. The two yellow regions in the figure represent the 40 nm-thick gold bowtie antenna positioned in the center of the nanowire, aimed at exploring a novel approach to stimulating the STP under 940 nm infrared irradiation. We measured both the electrical characteristics and noise spectra of LGAA NW FETs at various V_{DS} and V_{LG} values in a 1 mM PBS solution under different intensities of 940 nm LED excitation, as well as without it. To minimize light scattering and eliminate the influence of meniscus geometry, the LED was submerged in a liquid during the experiment.

Using Ansys Lumerical FDTD software, we modeled the redistribution of the electrical field between the two triangular segments of the antenna. Figure 5.1 (B),

Figure 5.1 (C), and Figure 5.1 (D) depict the high electrical field formation between the two gold triangles, calculated for distances (d) of 60 nm, 40 nm, and 20 nm between the two antenna segments, respectively. Optical simulations revealed that the maximum value of the electrical field (E) increases as the distance between the two antenna segments decreases. The maximum electrical-field intensity for LED field strength of 100 V/m was approximately 44 kV/m for a distance of 20 nm, 31 kV/m for 40 nm, and 25 kV/m for 60 nm, corresponding to the LGAA NW FET samples with the fabricated antenna under study.

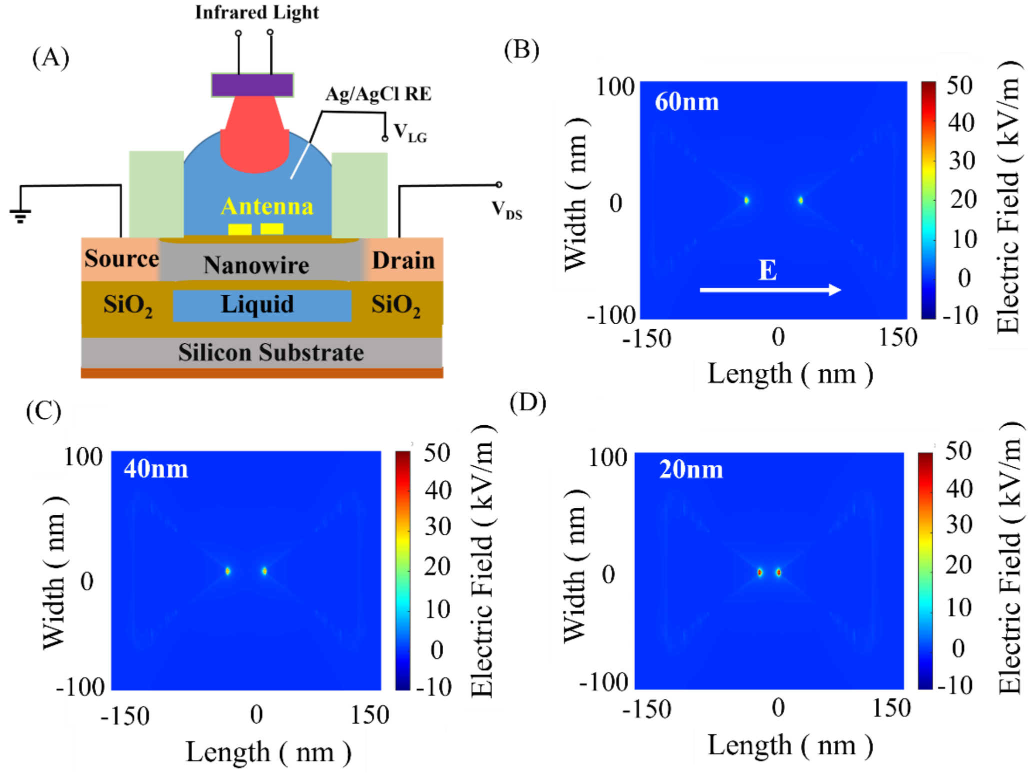

Figure 5.1. (A) Schematic illustration of an LGAA NW FET featuring a gold bowtie antenna subjected to 940 nm LED excitation; (B), (C), and (D) Modeling outcomes depicting the distribution of the electric field along the long axis of a bowtie antenna under 940 nm LED excitation, with antenna distances between two gold parts set at 60 nm, 40 nm, and 20 nm, respectively. (Described in [108])

SEM analysis (Figure 5.2 (A, B)) verified the nanoscale dimensions of the manufactured gold antennas attached to the nanowire surface. The optimized geometric shapes indicated a distance of approximately 40 nm between the two gold triangles.

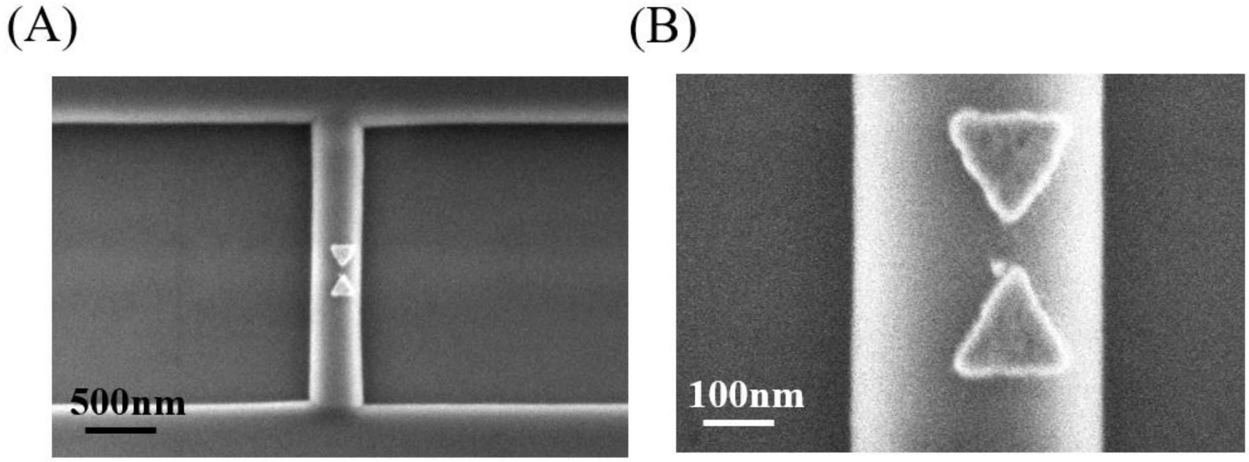

Figure 5.2. (A) SEM image shows the gold antenna positioned amid the GAA nanowires, fabricated between the source and drain regions, utilizing an SOI wafer. (B) Magnified view derived from Figure 5.2 (A) delineates the dimensions of the gold antenna, featuring two equilateral triangles, each with a side length of 120 nm. The distance between the two gold triangles is approximately 40 nm. (Described in [108])

Although the two pointed ends of the gold triangles are not perfectly aligned on a single line, an aspect that warrants improvement in future samples, our findings effectively show the induction of excited two-level RTS due to light stimulation, as elaborated below.

5.4 Transpor properties of LGAA FETs with BA under light excitation

Following the fabrication process, the electrical behavior of the LGAA NW FET device equipped with a gold bowtie antenna was assessed in a 1 mM PBS solution at pH = 7.4. Figure 5.3 (A) depicts a series of transfer characteristics examined for LGAA NW FET devices measuring 200 nm in width and 2 μm in length, featuring gold bowtie antennas across various V_{DS} values, without 940 nm infrared LED excitation. For comparison purposes, alterations in the transfer characteristics, as illustrated in Figure 5.3 (B), were observed compared to the curves displayed in Figure 5.3 (A) under the influence of a 5 mA forward-current-powered 940 nm LED excitation, measured across different drain-source voltages ranging from 10 mV to 100 mV. It is important to highlight that the intensity of the 940 nm LED was regulated by the current.

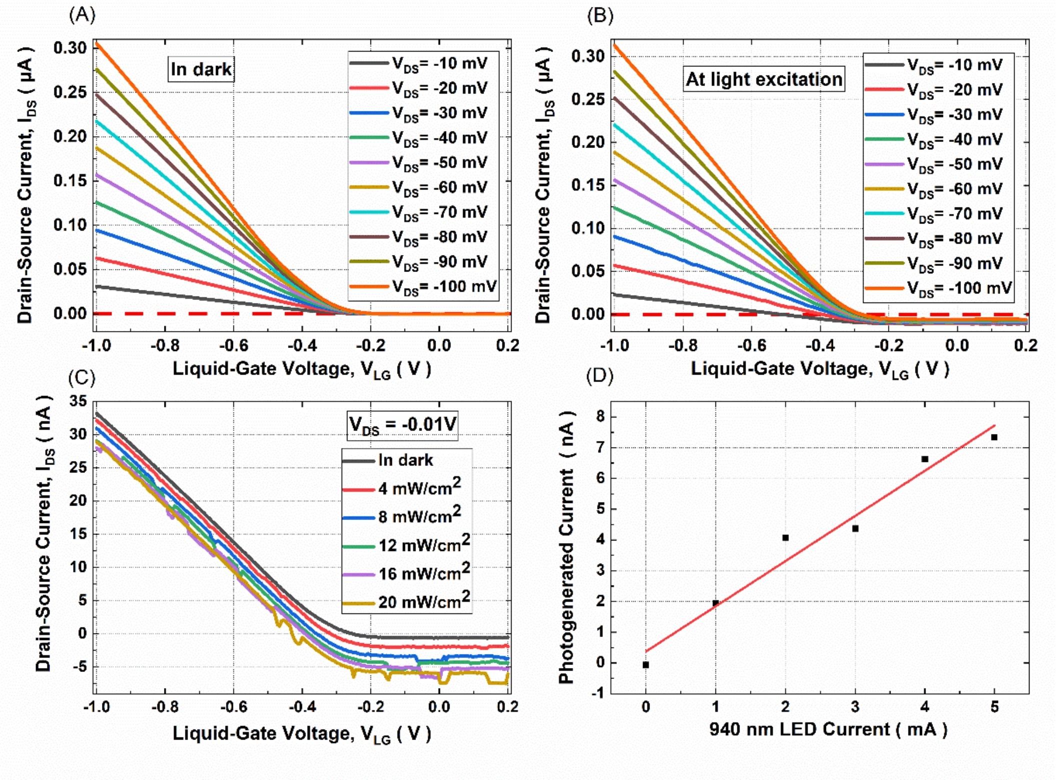

Figure 5.3. The transfer characteristics of LGAA NW FET devices with 200-nm-wide and 2-µm-long gold antennas were measured across various V_{DS} values ranging from -10 mV to -100 mV under two conditions: (A) in the absence of irradiation, that is, measured in the dark, and (B) with irradiation from a 5 mA 940 nm LED. The dashed red line at $I_{DS} = 0$ µA serves as a reference line in the dark to estimate the shifts observed in the I-V curves following optical excitation. (C) An enlarged view of the transfer characteristics of LGAA NW FET devices with 200-nm-wide and 2-µm-long gold antennas measured at V_{DS} = -10 mV under varying intensities of 940 nm LED excitation in a 1mM PBS solution at pH = 7.4.

(D) Displays the photogenerated current extracted from (C), demonstrating a linear relationship with the intensities of the 940 nm infrared LED. The red line represents the linear fitting of the recorded photogenerated current at $V_{LG} = 0$. (Described in [108])

In this context, 5 mA translates to 20 mW/cm^2 (optical power), representing the corresponding intensity, as shown in Figure 5.4 (A, B). As observed in Figure 5.3, under light excitation, the transfer I-V curves shift downward in comparison to the red dashed reference line measured in the dark. This shift in the I-V curves can be attributed to the generation of photogenerated current owing to the photovoltaic effect. [109] Nevertheless, analogous phenomena have been documented in various sources in the literature. Cho et al. investigated the photovoltaic effect in an ambipolar FET employing distinct electrodes (Au and Al as the source and drain, respectively). [110] This configuration generates a potential gradient owing to the variance in the work functions of the metals, enabling the device to demonstrate photovoltaic effects without any gate bias while simultaneously retaining the typical ambipolar FET characteristics under gate bias.

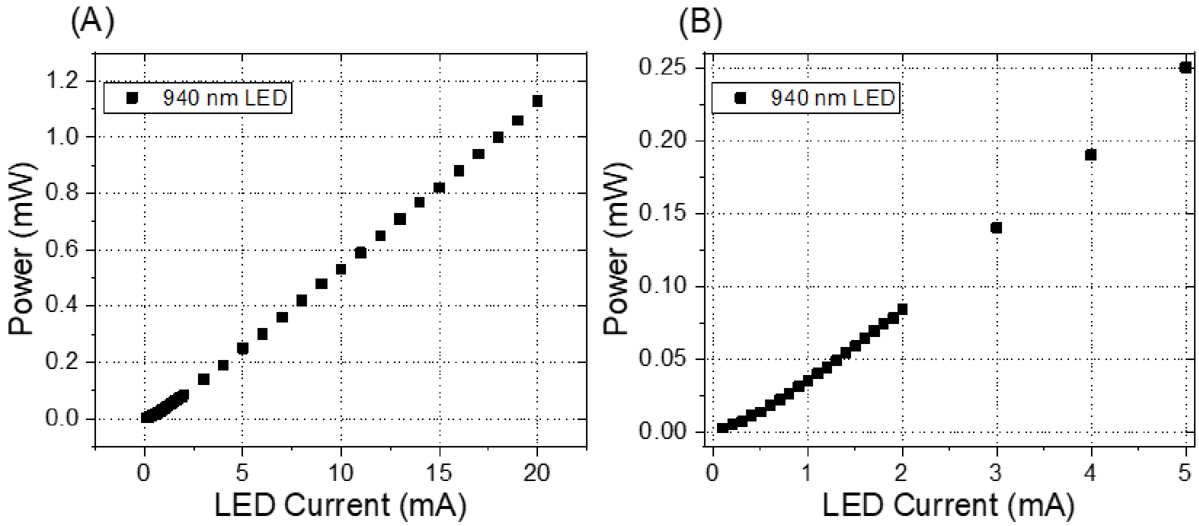

Figure 5.4. (A) The light power of the 940 nm LED plotted against the control current. (B) The magnified data from Figure 5.4 (A) illustrate a distinct correlation

between the power of the 940 nm LED and the current, spanning from 0 mA to 5 mA. (Described in [108])

To explore the effects observed in the transfer I-V curves under the influence of light, additional experiments were conducted using various intensities of the 940 nm LED. The I-V curves of the LGAA NW FETs with antennas subjected to infrared excitation at different intensities are shown in Figure 5.3 (C). The power output values (in mW/cm^2) of the 940 nm LED are 4, 8, 12, 16, and 20 corresponding to forward currents of the LED: 1 mA, 2 mA, 3 mA, 4 mA, and 5 mA, respectively. For these investigations, a small V_{DS} of -0.01 V was applied during the measurement of I-V characteristics for LGAA NW FET biosensors in 1 mM PBS solutions. The magnitude of the photogenerated current gradually increased with the light source intensity, resulting in a well-correlated shift in the I-V curves. This can be elucidated as follows: Figure 5.1 (B, C, D) illustrates the outcomes of calculating the electric field around the opposite sharp ends of the antenna under light excitation. The calculated potential distribution at the Si/SiO$_2$ interface in response to a point charge exhibits a significant potential alteration.[9] These findings indicate that at similar scales (several tens of nanometers), a pronounced peak is observed in the potential redistribution. In the case of a gold antenna, a notably steep potential gradient was established within the structure. This nanostructure, featuring a Schottky contact, triggers a photovoltaic effect, generating a potential contingent upon light intensity. Figure 5.3 (D) displays the photogenerated current values derived from the data presented in Figure 5.3 (C), measured at zero V_{LG}. The photogenerated current exhibited a linear relationship with light intensity.

Minor yet noteworthy peaks were noted in the I-V curves during the infrared treatment, indicating variations in the current (Figure 5.3 (C)). The findings reveal a noticeable increase in the frequency of current fluctuations as the intensity of the

940 nm LED increases. Our initial assumption was that these fluctuations are associated with the RTS, originating from the capture and release of carriers generated near the Si/SiO_2 interface due to optical excitation. This conjecture was substantiated through subsequent examination of the noise spectra and time trace experiments.

5.5 Noise spectroscopy of LGAA FETs with BA and revealed tunning effect allowing new amplification method for biosensors

To explore the relationship between the impact of the antenna on the nanowire surface and the dynamics attributed to traps in SiO_2 (gate oxide in contact with the PBS solution) near the Si/SiO_2 interface in LGAA NW FETs, we conducted noise spectrum measurements in a 1 mM PBS solution at pH = 7.4 under various intensities of 940 nm LED excitation. Figure 5.5 (A) shows the typical S_V of the drain voltage for an LGAA NW FET device with nanowire lengths and widths of 2 µm and 200 nm, respectively. These measurements were conducted at constant voltages: V_{LG} = -0.3 V and V_{DS} = -10 mV under different intensities of infrared treatment. Notably, the noise spectra measurements corroborate the earlier hypotheses regarding the behavior of the I-V characteristics. The observation of a Lorentzian peak under excitation with a 5 mA 940 nm LED in Figure 5.5 (A) supports our findings. The results suggest that under light excitation, LGAA NW FET devices with a bowtie antenna hold the potential to trigger a trap at the Si/SiO_2 interface, resulting in the occurrence of a STP.[58, 95]

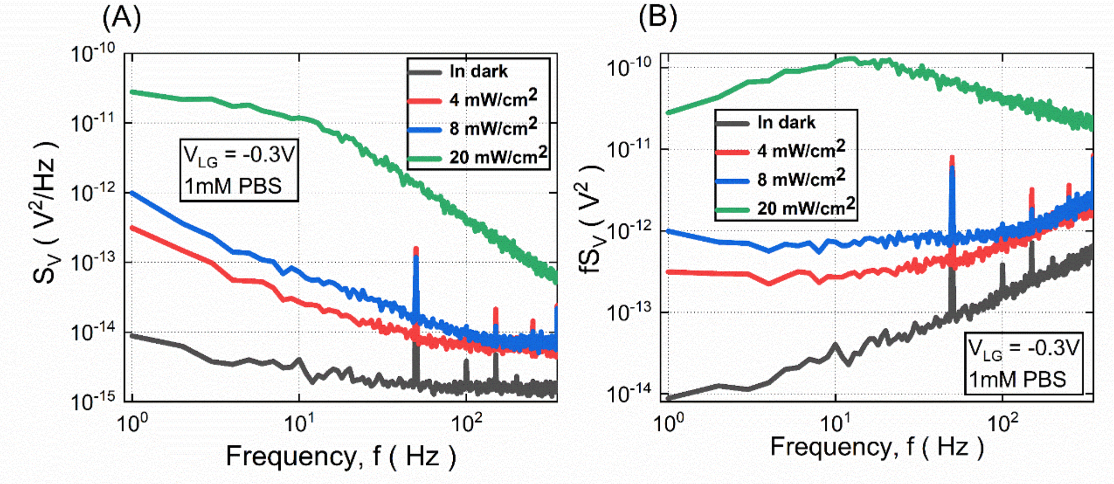

Figure 5.5. (A) Voltage spectral density measurements conducted on a nanowire measuring 2 μm in length and 200 nm in width under varying intensities of a 940 nm LED, maintaining a constant V_{LG} of -0.3 V and V_{DS} of -10 mV in a PBS solution. (B) Normalized noise spectra density measurements taken at constant V_{DS} and V_{LG}, showing prominent Lorentzian noise components that are particularly pronounced under infrared excitation. (Described in [108])

In Figure 5.5 (B), the S_V multiplied by f is plotted against f. [17] Through these plotted coordinates, the presence of a Lorentzian shape becomes more apparent in the noise spectra under infrared illumination. The morphology of the noise spectra appeared to be heavily influenced by light excitation. With increasing light intensity, the noise spectra exhibit Lorentzian-shaped characteristics, eventually leading to the formation of a well-defined Lorentzian shape when the intensity of the 940 nm LED reaches 5 mA.

In nanoscale FET device configurations, the presence of a Lorentzian shape is intimately linked to the manifestation of RTS noise, originating from the capture and release of charge carriers by a single trap situated in the dielectric layer near the Si/SiO_2 interface. In our investigation, the RTS phenomenon exclusively manifests when the LGAA NW FET is stimulated by a 940 nm LED.

The utilization of a two-level RTS is a well-established and valuable technique for investigating the dynamics of charge carriers within dielectric layers interfacing with a liquid, and for studying the STP. [17] It is noteworthy that in our NW structures, the emergence of a single trap under light excitation can be attributed to a significant electric field generated in the region between the two segments of the gold bowtie antenna on the device surface. Figure 5.6 illustrates the amplitude of RTS recorded in the measured V_{DS} under 940 nm LED illumination using an in-house noise measurement system, maintaining a constant V_{LG} = -0.5 V and V_{DS} = -10 mV. The fluctuations of V_{DS} increased across the range of infrared intensities from 0 mA to 5 mA. The onset of RTS in the PBS solution with pH = 7.4 occurred under light excitation. It is crucial to emphasize the correlation between this initial condition of light excitation and the occurrence of a two-level RTS in a sample with an antenna. Consequently, infrared contributes to a relatively larger amplitude of RTS at high light intensities, particularly at 20 mW/cm^2 for the 940 nm LED.

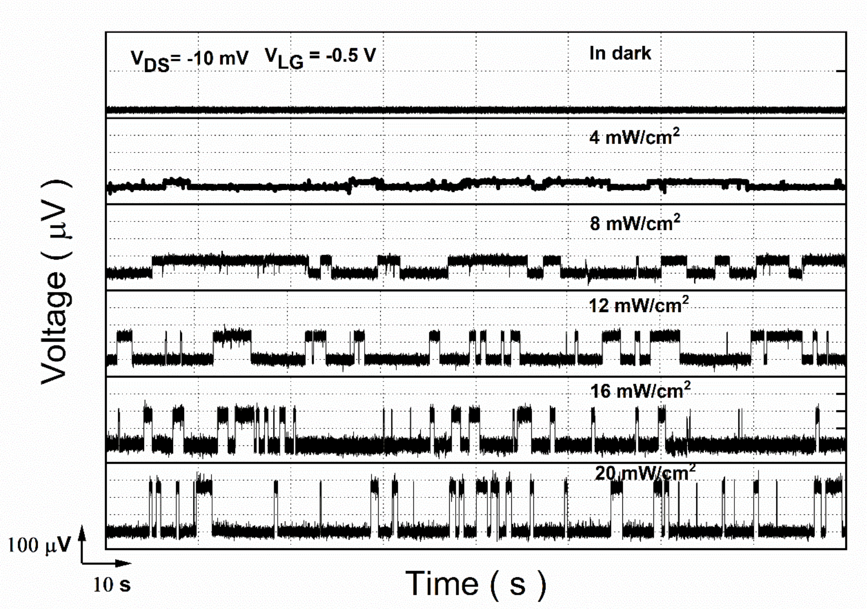

Figure 5.6. The two-level RTS observed in LGAA NW FETs with a nanowire with a length of 2 μm and a width of 200 nm in drain voltage V_{DS} recorded at constant

V_{LG} = -0.5 V and V_{DS} = -10 mV under different intensities of a 940 nm LED. (Described in [108])

For a more thorough understanding of RTS, it is essential to use statistical histogram analysis. Figure 5.7 illustrates the V_{DS} histograms acquired through time traces. In the context of the RTS phenomenon, the amplitude of the Gaussian peaks or the area beneath their curves corresponds to the emission and capture states of a single trap. As the light intensity increases, the two Gaussian peaks gradually become more discernible. This observation indicates that under light excitation, adjustable and enhanced conditions for analyzing the characteristic time constants for biosensing applications can be attained.

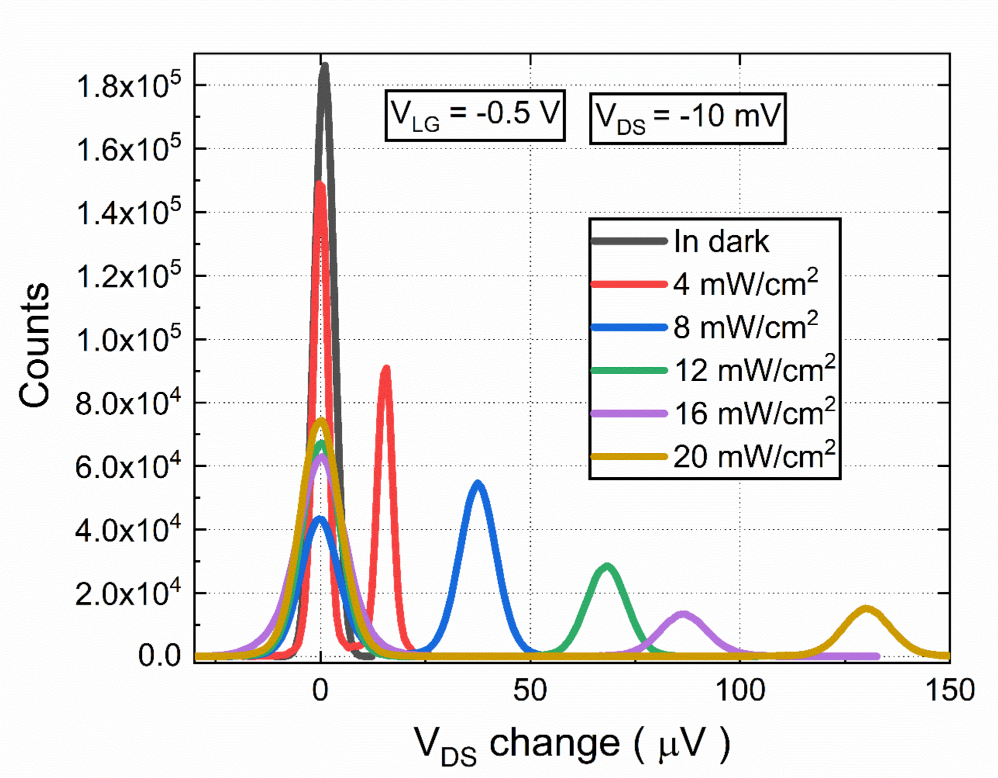

Figure 5.7 Histograms derived from time traces of two-level RTS distinctly portray separated Gaussian peaks, with the gap between them widening in tandem with the rise in RTS amplitude, which is attributed to the occurrence of STP. (Described in [108])

The histogram data can be described as follows. Under light excitation, the electric field of the electromagnetic wave is amplified by the gold antenna, leading to a redistribution of the potential in the Au/SiO_2/Si nanowire structure. The slopes of the conductance and valence bands in the SiO_2 dielectric layer underwent significant changes with increasing light intensity. A comparison between the black (dark) and red (light excitation) slopes in the SiO_2 dielectric layer is shown schematically in Figure 5.8, illustrating the band structure of the LGAA FET with a gold antenna (with energy levels represented by yellow lines). Under light excitation, the trap center located in the SiO_2 layer shifted its level position accordingly. As the center level approaches the energy of the Fermi level in the semiconductor, the trapping and detrapping processes of a carrier from the channel become more favorable.

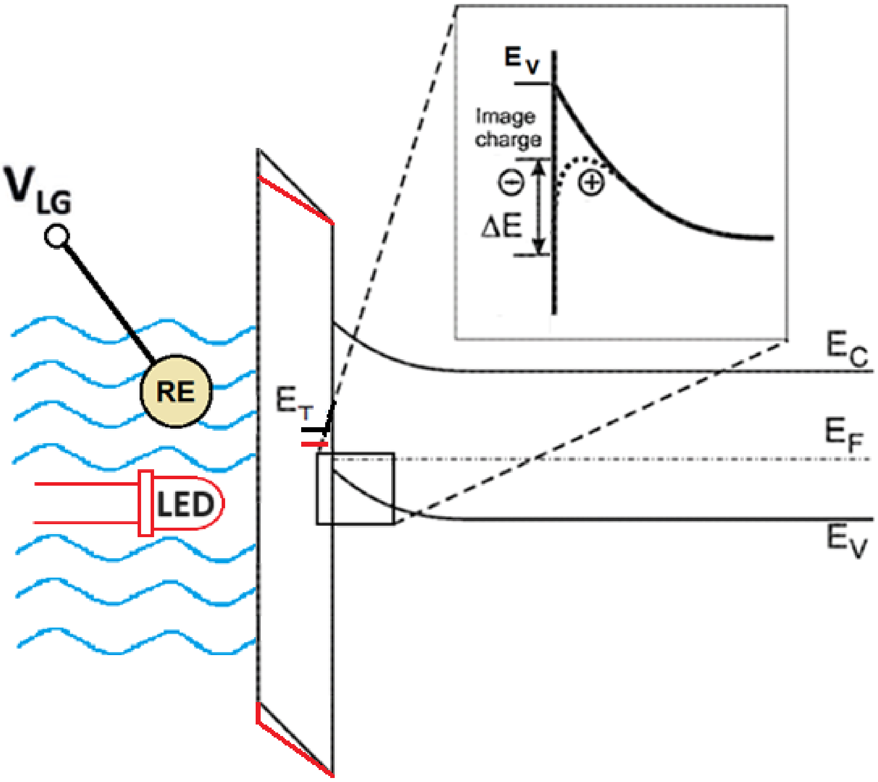

Figure 5.8. A schematic representation of the energy profile for an LGAA NW FET with a gold antenna is depicted, with the antenna represented by a yellow line. A trap

located at the Si/SiO_2 interface is denoted by a black dot (indicating the trap level, E_T, under dark conditions) and a red dot (under light excitation using LED of varying intensities). The blue waves represent the PBS solution. The inset shows an additional energy barrier for a hole in a p-type semiconductor before it is captured by a trap. E_C denotes the conductance band, and E_V denotes the valence band. (Described in [108])

The results of the RTS analysis are shown in Figure 5.9 (A). As shown in Figure 5.9 (A), the time constant τ_e remained constant regardless of the infrared intensity, indicating that carriers were excited in the nanowire with the same time constant under varying infrared excitation intensities. Conversely, the time constant τ_c exhibits dependence on the intensities of the 940 nm LED, with a slope of - 0.37 s/mA. The observed behavior of the characteristic times suggests that different intensities of infrared light can activate trapping centers, resulting in a reduction in the capture time with an increase in light intensity. The disparity between the capture and emission time constants was corroborated by the histogram data shown in Figure 5.7. Furthermore, the discussion regarding the time constants (τ_c and τ_e) strongly aligns with previous findings (in Figure 5.3 (C)), wherein the minor peaks in the current fluctuations within the I-V curve in response to light are indicative of RTS. This outcome further validates our discussion on a single trap. Under light excitation, a trap is formed by the high electric field generated in the middle part between two segments of the gold bowtie antenna.

In Figure 5.9 (B), the amplitude of RTS (ΔV_{DS}) attributed to the STP, derived from recorded time traces, is depicted as a function of 940 nm LED intensities, measured at a constant V_{DS} = -10 mV and V_{LG} = -0.5 V. As the intensity of the 940 nm LED increased, the RTS voltage amplitude tended to increase.

This can be explained as follows: a single trap activated by the antenna becomes more adept at capturing a carrier, leading to a significant modulation of an additional barrier near the Si/SiO$_2$ interface (as schematically illustrated in the inset of Figure 5.8).

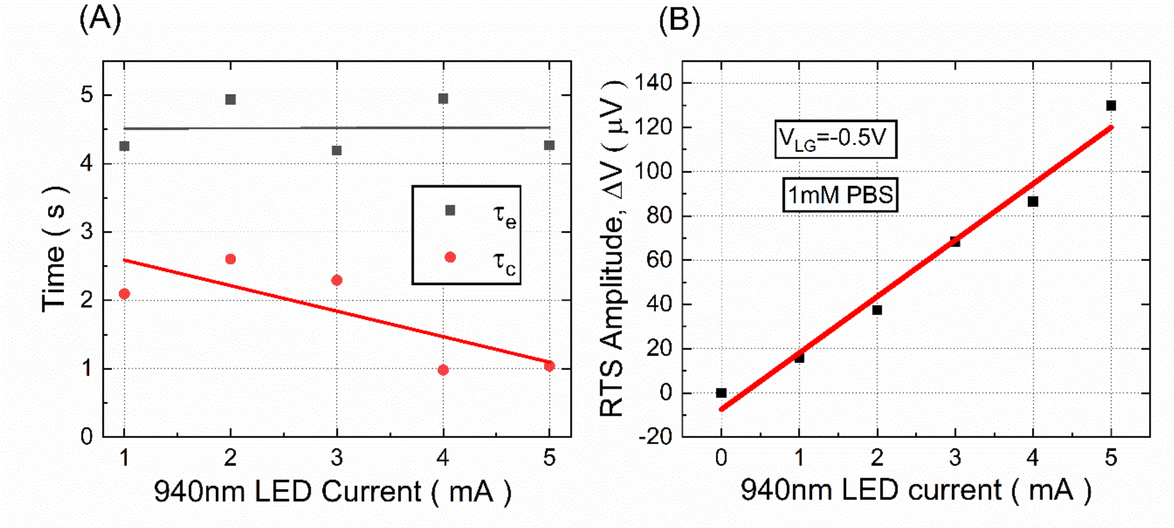

Figure 5.9. (A) The time constants τ_e and τ_c, varying with intensities controlled by the current of a 940 nm LED at V_{LG} = -0.5 V and V_{DS} = -10 mV, acquired for LGAA NW FETs with antennae on a nanowire measuring 2 µm in length and 200 nm in width. (B) The amplitude of the RTS voltage, corresponding to the range of 940 nm LED light intensities from 0 mA to 5 mA (0 mW/cm^2 to 20 mW/cm^2), obtained for a nanowire with a length of 2 µm and width of 200 nm in a 1 mM PBS solution at pH = 7.4. (Described in [108])

Additionally, the RTS amplitude increased with an increase in photocurrent, exhibiting a clear linear correlation with the infrared intensities. Figure 5.10 illustrates the alterations in the amplitude of RTS (ΔI_{DS}) resulting from the capture and emission processes of the carrier, deduced from recorded time traces at various photocurrents (refer to Figure 5.3 (C)).

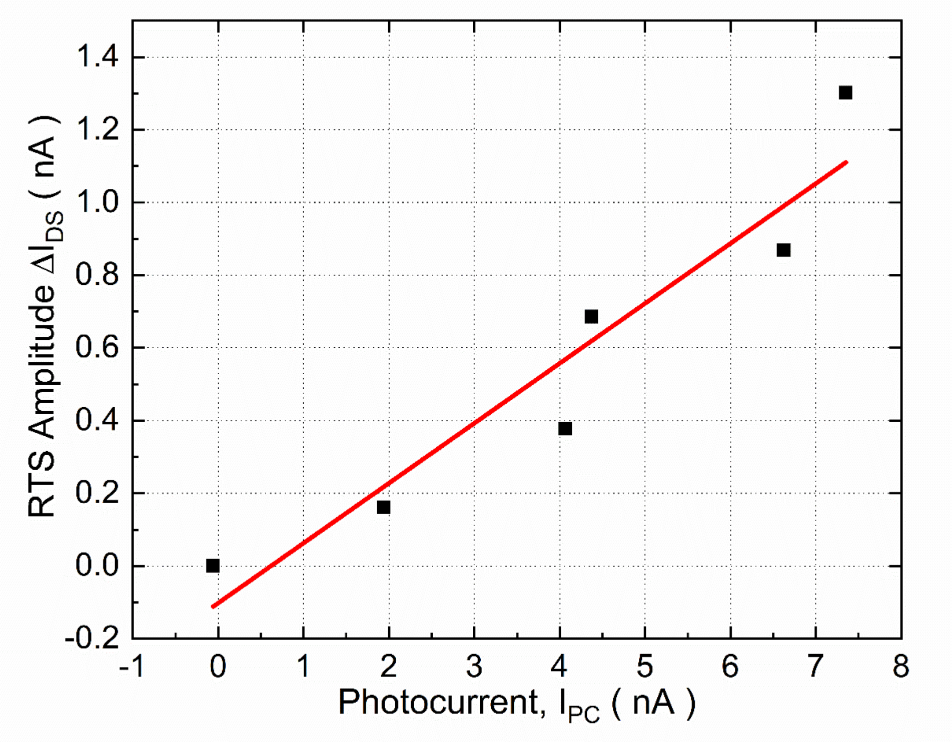

Figure 5.10. The RTS current amplitude is obtained as a function of the photogenerated current, I_{DS}, at V_{DS} = -10 mV and V_{LG} = -0.5V. These findings were derived for LGAA NW FETs with antennae on a nanowire measuring 2 µm in length and 150 nm in width, conducted in 1 mM PBS solution at pH 7.4. (Described in [108])

Notably, RTS was not detected at zero photocurrent in the dark. This suggests that a single trap was exclusively excited at the Si/SiO$_2$ interface within the area defined by the antenna of the LGAA FET device only under light excitation. The increase in the photogenerated current in the LGAA NW FETs indicates a trend towards an increased RTS current amplitude. This observation confirmed the presence of a two-level RTS induced by the photogenerated current under infrared excitation conditions. This phenomenon holds significance for achieving ultrahigh sensitivity in biosensors.

5.6 Summary

In summary, our studies of transport and noise characteristics of fabricated LGAA NW FET biosensors underline the pivotal role of the bowtie antenna excited at various 940 nm LED intencities. Regarding the electrical performance, we registered a shift in the I-V curves of the LGAA transistor under light treatment compared to the reference line recorded without optical excitation in a 1 mM PBS solution. Additionally, we identified photocurrent in liquid-gated device structures at the gate voltage equal to zero and detected small-amplitude peaks in the photocurrent of I-V characteristics, indicating current fluctuations induced by the RTS phenomenon. With regard to noise performance, we analyzed Lorentzian components in the voltage spectral density, confirming RTS excitation in LGAA NW FET biosensors with antennas under infrared applications. Under infrared excitation, the gold antenna effectively activated a single trap near the Si/SiO_2 interface, giving rise to a two-level quasi-digital RTS, as evidenced by time trace measurements and plotted histograms. Analysis of the characteristic time constants revealed a robust linear correlation between the time constants τ_c and light intensity, underscoring the significant potential of light to enhance the sensitivity of FET devices with antennas. These results were further supported by statistical analyses using histograms. The data obtained suggest promising applications for LGAA FETs with antennas in future biomonitoring applications.

6. Conclusions and outlook

6.1 Conclusions

This thesis describes new features and peculiarities registered in transport and noise properties of nanowire FET biosensors. The advanced technology for the fabrication of biosensors is developed and devices demonstrate high-quality characteristics. Electrical and noise characterization allows us to analyze the behavior of ions near the liquid/solid interface to study the performance of biosensors.

More detailed conclusions summarizing the main results described in the chapters of this thesis are as follows:

We designed and fabricated several liquid-gated FET devices highlighting the importance of the continuous development and improvement of FET-related technologies. Furthermore, studies of transport properties of FET devices allow us to demonstarate that liquid-gated FET structures play an important role in biosensing applications. Moreover, analysis of noise spectra and fluctuation phenomena highlight the significance of noise spectroscopy in the study of ion behavior at liquid/solid interfaces.

We reported a comprehensive overview of the layout design and cleanroom preparation process for the FET devices discussed. Using the Clewin 4 software, the layout design encompasses both the EBL and MA layouts. Furthermore, the chapter 2 outlines the optimized parameters of each crucial preparation step, serving as a roadmap for the future optimization of FET devices. Subsequently, detailed descriptions of the I-V, C-V, and noise spectroscopy methods as well as models, which were applied for detailed comparison of experiment with modeling data establishe the basis for testing and understading the developed FET biosensors.

We revealed that dimensionless α_H parameters and S_U characteristics act as effective indicators of ion behavior on the nanowire surface in FET-based biosensors. The charge inversion phenomenon at the solid/liquid interface was investigated in a divalent $MgCl_2$ electrolyte solution. Remarkably, the noise curves manifested two inflection points at concentrations of 10^{-4} M and 10^{-1} M, corresponding to the peaks and valleys of α_H and S_U, respectively. These inflection points reveal the trend of charge state transformation induced by ion competitive behavior near liquid/solid interface in solutions with different $MgCl_2$ concentrations (Chapter 3). In our case, the charge inversion phenomenon occurred at 10^{-4} M $MgCl_2$, which reflects that peculiarities of surface charged states should be taken into account by studies of biomolecules in divalent solutions. Such revealed features underscore the high potential of noise spectroscopy as a method of observing charge dynamic processes in biosensors and selection of their optimal working regimes and parameters.

We reported on features in transport regimes registered in LGAA NW FET biosensors in 1 mM PBS solution of pH =7.4. Our experimental data show that the transistor current contain not only a typical FET current component ($I \sim V^M$) with M equals 1, but also component with M exceeding 1 identified in this thesis as the SCLC effect. Moreover, the SCLC effect at $| V_{DS} | > 0.6$ V found in LGAA NW FET in the I-V curve with M equals 4, was confirmed by noise spectroscopy studies and RTS fluctuations associated with different charge states of the traps (Chapter 4). These findings reflect that it is essential to consider the SCLC phenomenon in FET devices alongside the utilization of the RTS method to enhance detection sensitivity for future applications in bio-detection fields of research. Moreover the SCLC phenomenon in FET devices and utilizing the RTS method allow to enhance the detection sensitivity of the biosensors.

We introduced and demonstrated the high potential of gold bowtie antennas in biosensor technology. By adjusting the intensity of the light source, we successfully initiated the activation of a single center at the dielectric/silicon interface, exciting the RTS phenomenon. LGAA FETs with fabricated gold bowtie antenna were studied in a 1 mM PBS solution of pH = 7.4, utilizing infrared 940 nm LED excitation (Chapter 5). Our electrical characeterization data revealed that the current in I-V curves increases proportionally to the LED intensity, indicating photocurrent generation. It should be emphasized that not only photocurrent was registered under LED illumination, but also a small amplitude fluctuation appeared in the I-V curves, which is attributed to the activation of a single trap center at the dielectric/silicon interface. Notably, we observed distinct Lorentzian-shaped noise when the LGAA NW FET was exposed to LED illumination. These findings highlight a correlation between the Lorentzian peaks in the noise spectra and the onset of the RTS by LED illumination of the device structures. Furthermore, we demonstrated that the amplitude of the fluctuation associated with the two-level RTS can be effectively controlled by increasing infrared intensity. These findings underscore the substantial potential of gold antenna for initiation of STP to exploit RTS to enhance biosensor sensitivity.

6.2 Outlook

Currently, there is a high demand for developing of compact and reliable point-of-care devices, which are driving rapid growth in the biosensor industry. Despite the recent emergence of several promising prototypes of nano biosensors for sophisticated in vivo sensing applications, the biosensor community continues to seek advanced biosensing technologies that will enable personalized healthcare and revolutionize medical services in the coming years. To address these challenges, the traditional concepts and conventional biosensing approaches must be redefined and redesigned. Consequently, it is anticipated that this new technology will allow innovative, user-friendly, high-sensitivity, and high-quality device structures that can guide personalized medicine and deliver healthcare in a fast, reliable, and relatively inexpensive manner. In this context, miniaturized nano biosensors have garnered significant attention because they have the potential to serve as a complete "lab-on-chip" biosensing platform, offering a new paradigm for early disease diagnosis and monitoring human health status.

To further explore the potential of single traps in LGAA NW FETs for biosensing, it is essential to consider the correlation effects among different traps in NW devices. We anticipate that investigating the strong coupling between individual charged traps or trap states, such as a closely interacting cluster of localized electronic trap states in the gate dielectric layer, will reveal novel effects that facilitate enhanced signal transduction from the target analyte. The enhancement may occur as a result of several traps, which can be activated simultaneously or one by one. Additionally, the analytical model developed in our group for explaining enhanced STP dynamics in LGAA NW FETs can be expanded by considering quantum tunneling and strain effects, which affect capture and emission processes in nanoscale devices. Understanding and incorporating these effects could provide valuable insights into enhancing the sensitivity of nanoscale devices that utilize STP. From the perspective of characterizing STP-based devices, designing and assembling a portable noise measurement setup will enable labor-independent low-frequency noise spectroscopy. This tool will enable the characterization of nano biosensors using the STP approach to enhance sensitivity of biosensors for development of predictable biomedical analysis. We anticipate that the proposed roadmap for future investigations will strengthen the innovative STP-based biosensing strategy outlined in this study, and facilitate the development of powerful, effective, and commercially viable single-trap-based devices for personalized healthcare services in the near future.

List of Abbreviations

AC alternating current

BA bowtie antenna

BOE buffered oxide etch

BOX buried oxide

CMOS complementary metal oxide semiconductor

CRP C-reactive protein

cTnl cardiac troponin I

C-V capacitance voltage

DC direct current

DNA single stranded deoxyribonucleic acid

DUT device under test

EIS electrolyte insulator semiconductor

FET field effect transistor

FIB focused ion beam

GAA gate all around

HMDS hexamethyldisilazane

IPA isopropanol

ISFET ion-sensitive field effect transistor

I-V current voltage

LG liquid gate

LGAA liquid gate all around

MOS metal oxide semiconductor

NW nanowire

PBS phosphate buffered saline
PDMS polydimethylsiloxane
PECVD plasma enhanced chemical vapor deposition
PI polyimide
PMMA poly(methyl methacrylate)
RIE reactive ion etching
RTS random telegraph signal
RTP rapid thermal annealing
SCLC space-charge-limited-current
Si silicon
SMU source measurement unit
SOI silicon on insulator
ssDNA single stranded deoxyribonucleic acid
STP single trap phenomenon
TMAH tetramethylammonium hydroxide

References

1. P. Bergveld. “Thirty years of ISFETOLOGY: What happened in the past 30 years and what may happen in the next 30 years”. Sensors and Actuators, B: Chemical 88.1 (2003), pp. 1–20.
2. A. Tarasov et al. “Understanding the Electrolyte Background for Biochemical Sensing with Ion-Sensitive Field-Effect Transistors”. Nano Letters 6.10 (2012), pp. 9291–9298.
3. N. Clément et al. “A silicon nanowire ion-sensitive field-effect transistor with elementary charge sensitivity”. Applied Physics Letters 98.1 (2011), pp. 96–99.
4. S. Chen et al. “Al_2O_3/silicon nano ISFET with near ideal nernstian response”. Nano Letters 11.6 (2011), pp. 2334–2341.
5. J. Li et al. “Monitoring of Dynamic Processes during Detection of Cardiac Biomarkers Using Silicon Nanowire Field-Effect Transistors”. Advanced Materials Interfaces 2000508.15 (2020), pp. 1–11.
6. K. Bedner et al. “pH Response of Silicon Nanowire Sensors: Impact of Nanowire Width and Gate Oxide”. Sensors and Materials 25.8 (2013), pp. 567–576.
7. F. Patolsky, G. Zheng, and C. M. Lieber. “Fabrication of silicon nanowire devices for ultrasensitive, label-free, real-time detection of biological and chemical species”. Nature Protocols 1.4 (2006), pp. 1711–1724.
8. K. Kim et al. “Silicon nanowire biosensors for detection of cardiac troponin I (cTnI) with high sensitivity.” Biosensors & bioelectronics 77 (2016), pp. 695–701.
9. Y. Kutovyi et al. “Origin of noise in liquid-gated Si nanowire troponin biosensors”. Nanotechnology 29.17 (2018), 175202.
10. A. de Moraes and L. Kubota. “Recent Trends in Field-Effect Transistors-Based Immunosensors”. Chemosensors 4.4 (2016), p. 20.
11. M. S. Makowski and A. Ivanisevic. “Molecular analysis of blood with micro-nanoscale field-effect-transistor biosensors”. Small 7.14 (2011), pp. 1863–1875.
12. B. C. Cheah et al. “An Integrated Circuit for Chip-Based Analysis of Enzyme Kinetics and Metabolite Quantification”. IEEE Transactions on Biomedical Circuits and Systems 10.3 (2016), pp. 721–730.
13. J. M. Rothberg et al. “An integrated semiconductor device enabling non-optical genome sequencing”. Nature 475.7356 (2011), pp. 348–352.

14. G. S. Kulkarni and Z. Zhong. “Detection beyond the Debye screening length in a high-frequency nanoelectronic biosensor”. Nano Letters 12.2 (2012), pp. 719–723.
15. E. Stern et al. “Importance of the Debye Screening Length on Nanowire Field Effect Transistor Sensors”. Nano Letters 7.11 (2009), pp. 3405–3409.
16. V. Pachauri and S. Ingebrandt. “Biologically sensitive field-effect transistors: From ISFETs to NanoFETs”. Essays in Biochemistry 60.1 (2016), pp. 81–90.
17. Y. Kutovyi et al. “Amyloid-beta peptide detection via aptamer-functionalized nanowire sensors exploiting single-trap phenomena”. Biosens Bioelectron, 2020. 154: p. 112053.
18. Y. Kutovyi et al. “Highly Sensitive and Fast Detection of C-Reactive Protein and Troponin Biomarkers Using Liquidgated Single Silicon Nanowire Biosensors”. MRS Advances, 2020. 5(16): p. 835-846.
19. T. Goda et al. “DNA Biosensing Using Field Effect Transistors”. Current Physical Chemistry, 2011. **1**(4): p. 276-291.
20. Baraban L, Ibarlucea B, Baek E, et al. “Hybrid silicon nanowire devices and their functional diversity”. Advanced Science, 2019, 6(15): 1900522.
21. A. Heinzig, S. Slesazeck, F. Kreupl, et al. “Reconfigurable silicon nanowire transistors”. Nano Lett., 2012, 12(1): 119-124.
22. G. J. Zhang, L. Zhang, M. J. Huang, et al. “Silicon nanowire biosensor for highly sensitive and rapid detection of Dengue virus”. Sensors and Actuators B: Chemical, 2010, 146(1): 138-144.
23. X. Duan, Y. Li, N. K. Rajan, et al. “Quantification of the affinities and kinetics of protein interactions using silicon nanowire biosensors”. Nat. Nanotechnol, 2012, 7(6): 401-407.
24. P. Namdari, H. Daraee, A. Eatemadi. “Recent advances in silicon nanowire biosensors: synthesis methods, properties, and applications”. Nanoscale Res Lett., 2016, 11(1): 1-16.
25. P. Bergveld, et al. “The operation of an ISFET as an electronic device”. Sensors and Actuators, 1981, 1: 17-29.
26. H. Cho, K. Kim, J. S. Yoon, et al. “Optimization of signal to noise ratio in silicon nanowire ISFET sensors”. IEEE Sensors Journal, 2017, 17(9): 2792-2796.
27. S. Kim, T. Rim, K. Kim, et al. “Silicon nanowire ion sensitive field effect transistor with integrated Ag/AgCl electrode: pH sensing and noise characteristics”. Analyst, 2011, 136(23): 5012-5016.
28. Y. Cui, Q. Wei, H. Park, et al. “Nanowire nanosensors for highly sensitive and selective detection of biological and chemical species”. Science, 2001, 293(5533): 1289-1292.

29. F. Patolsky, G. Zheng, O. Hayden, et al. “Electrical detection of single viruses”. Proceedings of the National Academy of Sciences, 2004, 101(39): 14017-14022.
30. G. Zheng, F. Patolsky, Y. Cui, et al. “Quantitative Real-Time Measurements of DNA Hybridization with Alkylated Nonoxidized Silicon Nanowires in Electrolyte Solution”. Nat. Biotechnol, 2005, 23: 1294-1301.
31. J. Schütt, B. Ibarlucea, R. Illing, et al. “Compact nanowire sensors probe microdroplets”. Nano Lett., 2016, 16(8): 4991-5000.
32. C. C. Hsu, Y. C. Liao, Y. T. Tsai, et al. “Multiple silicon nanowires with enzymatic modification for measuring glucose concentration”. Micromachines, 2015, 6(8): 1135-1142.
33. R. Sivakumarasamy, R. Hartkamp, B. Siboulet, et al. “Selective layer-free blood serum ionogram based on ion-specific interactions with a nanotransistor”. Nat. Mater., 2018, 17(5): 464-470.
34. H. P. Soroka, A. Pevzner, G. Davidi, et al. “Optically-gated self-calibrating nanosensors: monitoring pH and metabolic activity of living cells”. Nano Lett., 2013, 13(7): 3157-3168.
35. B. Ibarlucea, T. Rim, C. K. Baek, et al. “Nanowire sensors monitor bacterial growth kinetics and response to antibiotics”. Lab on a Chip, 2017, 17(24): 4283-4293.
36. F. Patolsky, B. P. Timko, G. Yu, et al. “Detection, stimulation, and inhibition of neuronal signals with high-density nanowire transistor arrays”. Science, 2006, 313(5790): 1100-1104.
37. J. F. Eschermann, R. Stockmann, M. Hueske, et al. “Action potentials of HL-1 cells recorded with silicon nanowire transistors”. Applied Physics Letters, 2009, 95(8): 083703.
38. D. P. Tran, M. A. Winter, B. Wolfrum, et al. “Toward intraoperative detection of disseminated tumor cells in lymph nodes with silicon nanowire field effect transistors”. ACS Nano, 2016, 10(2): 2357-2364.
39. J. Wang, F. Shen, Z. Wang, et al. “Point Decoration of Silicon Nanowires: An Approach Toward Single-Molecule Electrical Detection”. Angewandte Chemie, 2014, 126(20): 5138-5143.
40. A. Gao, N. Lu, P. Dai, et al. “Silicon-nanowire-based CMOS-compatible field-effect transistor nanosensors for ultrasensitive electrical detection of nucleic acids”. Nano Lett., 2011, 11(9): 3974-3978.
41. P. R. Saulson. “Thermal noise in mechanical experiments”. Physical Review D, 1990, 42(8): 2437.
42. R. Aguado, T. Brandes. “Shot noise spectrum of open dissipative quantum two-level systems”. Phys. Rev. Lett., 2004, 92(20): 206601.

43. A. V. D. Ziel. " Flicker noise in electronic devices". Advances in electronics and electron physics. Elsevier, 1979: 225-297.
44. L. Vandamme, F. Hooge. "On the additivity of generation-recombination spectra Part 3: The McWhorter model for 1/f noise in MOSFETs". Physica B: Condensed Matter, 2005, 357(3-4): 507-524.
45. N. Clément, K. Nishiguchi, A. Fujiwara, et al. "One-by-one trap activation in silicon nanowire transistors ". Nat. Commun., 2010, 1(1): 1-8.
46. K. Bedner, V. A. Guzenko, A. Tarasov, et al. "Investigation of the dominant 1/f noise source in silicon nanowire sensors". Sensors and Actuators B: Chemical, 2014, 191: 270-275.
47. C. Jakobson, I. Bloom, Y. Nemirovsky. "1/f noise in CMOS transistors for analog applications from subthreshold to saturation". Solid-State Electronics, 1998, 42(10): 1807-1817.
48. F. Hooge. "Discussion of recent experiments on 1/*f* noise". Physica, 1972, 60(1): 130-144.
49. P. Gaubert, A. Teramoto, T. Ohmi, et al. "1/f Noise of accumulation mode p- and n-MOSFETs"; proceedings of the 2013 22nd International Conference on Noise and Fluctuations (ICNF), F, 2013. IEEE.
50. P. Gaubert, A. Teramoto, S. Sugawa. "1/f Noise Performances and Noise Sources of Accumulation Mode Si (100) n-MOSFETs"; proceedings of the Proceedings of the International Conference on Solid State Devices and Materials, Sapporo, Japan, F, 2015.
51. P. Gaubert, A. Teramoto, S. Sugawa. " Impact of doping concentration on 1/f noise performances of accumulation-mode Si (100) n-MOSFETs". Japanese Journal of Applied Physics, 2016, 55(4S): 04ED08.
52. D. M. Kim, Y. H. Jeong. "Nanowire field effect transistors: Principles and Applications". Springer, 2014.
53. A. R. Wagner, S. W. Ellis. "Vapor-liquid-solid mechanism of single crystal growth". Applied Physics Letters, 1964, 4(5): 89-90.
54. P. Bergveld, "Development of an Ion Sensitive Solid State Device for Neurophysiological Measurements". IEEE Trans. Biomed. Eng., 1972. **19**(342).
55. F. Patolsky, G. Zeng, O. Hayden, et al. "Electrical detection of single viruses". Natl. Acad. Sci., 2004. **101**(4017).
56. Y. Cui, Q. Wei, H. Park, et al. "Nanowire Nanosensors for Highly Sensitive and Selective Detection of Biological and Chemical Species". Science, 2001. **293**(1289).
57. H. S. Song, T. H. Park, "Integration of biomolecules and nanomaterials: towards highly selective and sensitive biosensors". Biotechnol J, 2011. **6**(11): p. 1310-6.

58. Y. Kutovyi, I. Zadorozhnyi, V. Handziuk, et al. “Liquid-Gated Two-Layer Silicon Nanowire FETs: Evidence of Controlling Single-Trap Dynamic Processes”. Nano Lett., 2018. **18**(11): p. 7305-7313.
59. S. X. Li, W. Guan, B. Weiner, et al. “Direct Observation of Charge Inversion in Divalent Nanofluidic Devices”. Nano Lett., 2015. **15**(8): p. 5046-51.
60. K. B. Parizi, “ ISFET pH Sensitivity: Counter-Ions Play a Key Role”. Sci. Rep., 2017. **7**: p. 41305.
61. B. I. Shklovskii, “Screening of a macroion by multivalent ions: Correlation-induced inversion of charge”. Phys. Rev. E, 1999. **60**(5802).
62. E. Wernersson, R. Kjellander, J. Lyklema, “Charge Inversion and Ion-Ion Correlation Effects at the Mercury/Aqueous $MgSO_4$ Interface: Toward the Solution of a Long-Standing Issue”. J. Phys. Chem. C, 2010. **114**(1849).
63. D. E. Yates, S. Levine, T. W. Healy, “Site-binding Model of the Electrical Double Layer at the Oxide/Wat er Iiiterface”. J. Chem. Soc. 1973. **70**(1807).
64. M. Wipf, R. L. Stoop, A. Tarasov, et al. “Selective Sodium Sensing with Gold-Coated Silicon Nanowire Field-Effect Transistors in a Differential Setup”. ACS Nano Lett., 2013. **7**(5978).
65. Y. Guo, D. Pustovyi, Y. Kutovyi, et al. “Noise Spectroscopy of Transport and Ion-Related Phenomena in Silicon Nanowire Field-Effect Transistor Biosensors”. Adv. Mater. Interfaces, 2022. **9**(32).
66. A. A. Talin, F. Léonard, B. S. Swartzentruber, et al. “Unusually strong space-charge-limited current in thin wires”. Phys Rev Lett., 2008. **101**(7): p. 076802.
67. A. A. Talin, F. Leonard, A. M. Katzenmeyer, et al. “Transport characterization in nanowires using an electrical nanoprobe”. Semiconductor Science and Technology, 2010. **25**(2).
68. Y. Gu, L. J. Lauhon, “Space-charge-limited current in nanowires depleted by oxygen adsorption”. Applied Physics Letters, 2006. **89**(14).
69. A. D. Schricker, F. M. Davidson, R. J. Wiacek, et al. “Space charge limited currents and trap concentrations in GaAs nanowires”. Nanotechnology, 2006. **17**(10): p. 2681-2688.
70. P. Zhang, “Space–charge limited current in nanodiodes: Ballistic, collisional, and dynamical effects”. Journal of Applied Physics, 2021. **129**(10).
71. S. Alagha, A. Shik, H. E. Ruda, et al. “Space-charge-limited current in nanowires”. Journal of Applied Physics, 2017. **121**(17).
72. K. Besteman, M. A. G. Zevenbergen, S. G. Lemay, “Charge inversion by multivalent ions: dependence on dielectric constant and surface-charge density”. Phys. Rev. E Stat. Nonlin. Soft Matter. Phys., 2005. **72**(6): p. 061501.
73. P. A. Christensenand, A.Hamnett, Techniques andMechanisms in Electrochemistry, Blackie Academic & Professional, An Imprint Of Chapman & Hall, Kluwer Academic Publishers, Glasgow 1994, 379.

74. H. Hlukhova, “Highly Sensitive Aptamer-Based Method for the Detection of Cardiac Biomolecules on Silicon Dioxide Surfaces”. MRS Advances, 2018. **3**(27): p. 1535-1541.
75. F. N. Hooge, “1/f noise is no surface effect”. Phys. Lett., 1969. **29**(3): p. 139-140.
76. M. Hartman, M. Östling, Low-Frequency Noise in Advanced MOS Devices. 2007: Springer.
77. J. Lee, I. Han, B. Y. Yu, et al. “Physical Understanding of the Hooge Parameter in ZnO Nanowire Devices”. Journal of the Korean Physical Society, 2008. **53**(1): p. 339-342.
78. Y. Zhang, N. Boichuk, D. Pustovyi, et al. “Noise Spectroscopy Analysis of Ion Behavior in Liquid Gate-All-Around Silicon Nanowire Field-Effect Transistor Biosensors”. Advanced Materials Interfaces, 2023. **10**(36).
79. E. Niklas, I. Sychugov, T. Engfeldt, et al. “Surface Charge Sensitivity of Silicon Nanowires: Size Dependence”. Nano Lett., 2007. 7(9).
80. J. Li, S. Pud, D. Mayer, et al. “Advanced fabrication of Si nanowire FET structures by means of a parallel approach”. Nanotechnology, 2014. **25**(27): p. 275302.
81. J. Li, et al. “Advanced performance and scalability of Si nanowire field-effect transistors analyzed using noise spectroscopy and gamma radiation techniques”. Journal of Applied Physics, 2013. **114**(20).
82. M. J. Kirton, M. J. Uren, “Noise in solid-state microstructures: A new perspective on individual defects, interface states and low-frequency (1/*f*) noise”. Advances in Physics, 1989. **38**(4): p. 367-468.
83. Y. Shen, J. Cui, S. Mohammadi, “An accurate model for predicting high frequency noise of nanoscale NMOS SOI transistors”. Solid-State Electronics, 2017. **131**: p. 45-52.
84. M. Kuscu, O. B. Akan, “Modeling and Analysis of SiNW FET-Based Molecular Communication Receiver”. IEEE Transactions on Communications, 2016. **64**(9): p. 3708-3721.
85. M. Petrychuk, I. Zadorozhnyi, Y. Kutovyi, et al. “Noise spectroscopy to study the 1D electron transport properties in InAs nanowires”. Nanotechnology, 2019. **30**(30): p. 305001.
86. Y.Kutovyi, H.Hlukhova, M.Petrychuk, et al. “Low frequency noise in Si NW FET for electrical biosensing”. IEEE, 2017. **pp.**(1-4).
87. E. Simoen, N. Garbar, et al. “Flicker noise in submicron MOSFET with 3.5 nm nitrided gate oxide”. ICNF 2001, Geinesville, USA, 2001.
88. T. Sakata, R. Shiratori, M. Kato, “Hydrogel-Coated Gate Field-Effect Transistor for Real-Time and Label-Free Monitoring of beta-Amyloid Aggregation and Its Inhibition”. Anal. Chem., 2022. **94**(6): p. 2820-2826.

89. N. F. Mott, R. W. Gurney, Electronic processes in ionic crystals, 2nd ed, Clarendon Press, Oxford 1948.
90. M. A. Lampert, P. Mark, Current Injection in Solids, Academic Press New York 1970.
91. A.A.Grinberg, S. Luryi, M. R. Pinto, et al. "Space-charge-limited current in a film". IEEE Trans. Electron Devidces 1989, 36, 1162.
92. W. Xu, A. Chin, L. Ye, et al. "Charge transport and trap characterization in individual GaSb nanowires". Journal of Applied Physics, 2012. **111**(10).
93. B.S. Simpkins, M. A. Mastro, C. R. Eddy, et al. "Space-charge-limited currents and trap characterization in coaxial AlGaN/GaN nanowires". Journal of Applied Physics, 2011. **110**(4).
94. S. Pud, J. Li, V. Sibiliev, et al. "Liquid and back gate coupling effect: toward biosensing with lowest detection limit". Nano Lett, 2014. **14** (2): p. 578-84.
95. Y. Zhang, N. Boichuk, D. Pustovyi, et al. "Peculiarities of the SCLC Effect in Gate-All-Around Silicon Nanowire Field-Effect Transistor Biosensors". Advanced Electronic Materials, 2024, 2300855.
96. V. Handziuk, Y. Kutovyi, H.Hlukhova, et al. "Nanoimprint Technology for Liquid-Gated Si Nanowire FET Biosensors: Noise Spectroscopy Analysis" ICNF 2019, 2019, 269199, 1-4.
97. V. A. Sydoruk, I. Zadorozhnyi, H. Hardtdegen, et al. "Electronic edge-state and space-charge phenomena in long GaN nanowires and nanoribbons". Nanotechnology, 2017. 28(13): p. 135204.
98. A. Rose, "Space-Charge-Limited Currents in Solids". Physical Review, 1955. **97**(6): p. 1538-1544.
99. S. Tehrani, H. Goronkin, M.M. Hoogstra, et al. "Excess Drain Current in Heterojunction FET's due to Substrate Space-Charge-Limited Current". IEEE, 1989. 36: p. 1591-1596.
100. N. B. Lukyanchikova, Noise Research in Semiconductor Physics, 1997, London.
101. S. Pud, J. Li, V. Sibiliev, et al. "Liquid and Back Gate Coupling Effect: Toward Biosensing with Lowest Detection Limit". Nano Lett. 2014, 14, 578.
102. Y. Kutovyi, I. Madrid, N. Boichuk, et al. "Single-trap phenomena stochastic switching for noise suppression in nanowire FET biosensors". Japanese Journal of Applied Physics, 2021. **60**, 1-5.
103. I. Zadorozhnyi, et al. "Effect of Gamma Irradiation on Dynamics of Charge Exchange Processes between Single Trap and Nanowire Channel". Small, 2018. **14**(2), 1702516.
104. Y. Guo, D. Pustovyi, Y. Kutovyi, et al. "Noise Spectroscopy of Transport and Ion-Related Phenomena in Silicon Nanowire Field-Effect Transistor Biosensors". Advanced Materials Interfaces, 2022. **9**(32).

105. M. Petrychuk, A. Fujiwara, D. Pustovyi, ey al. “Optically Controlled Nano FET Toward Advanced Biosensing Applications”. IEEE, Editor. 2023.
106. M. Petrychuk, D. Pustovyi, N. Boichuk, et al. “New Approach for Enhancing Sensitivity in Liquid-Gated Nanowire FET Biosensors Under Optical Excitation”. Advanced Materials Technologies, 2024. 2301303.
107. S. Pud, D. Verschueren, N. Vukovic, et al. “Self-Aligned Plasmonic Nanopores by Optically Controlled Dielectric Breakdown”. Nano Lett., 2015. **15**(10): p. 7112-7.
108. Y. Zhang, N. Boichuk, D. Pustovyi, et al. “Impact of Light Excitation on Liquid Gate ‐ All ‐ Around Silicon Nanowire Field ‐ Effect Transistor Biosensors with Bowtie Antenna”. Advanced Electronic Materials, 2024.. Advanced Materials Technologies, 2024, 2400747.
109. N. Marjanović, T. Singh, G. Dennler, et al. “Photoresponse of organic field-effect transistors based on conjugated polymer/fullerene blends”. Organic Electronics, 2006. **7**(4): p. 188-194.
110. S. Cho, J. Yuen, J. Y. K. Lee, et al. “Photovoltaic effects on the organic ambipolar field-effect transistors”. Applied Physics Letters, 2007. **9**(6): p. 063511.

Personal publication list

Peer-Reviewed journals

1.**Yongqiang Zhang**, Kai Li, Nazarii Boichuk, Denys Pustovyi, Valeriia Chekubasheva, Hanlin Long, Mykhailo Petrychuk, and Svetlana Vitusevich*. Silicon Nanowire Field-Effect Transistor Biosensors with Bowtie Antenna. Solid State Electronics.2025. (DOI:https://doi.org/10.1016/j.sse.2025.109230)

2.**Yongqiang Zhang**, Nazarii Boichuk, Denys Pustovyi, Valeriia Chekubasheva, Hanlin Long, Mykhailo Petrychuk, and Svetlana Vitusevich*. Noise Spectroscopy of Liquid-Solid Interface Processes in Adjusted Physiological Solutions using GAA Si Nanowire FET Biosensors. Adv.Sensor Res. 2025.(DOI:10.1002/adsr.202500101)

3.**Yongqiang Zhang**, Kai Li, Nazarii Boichuk, Denys Pustovyi, Valeriia Chekubasheva, Hanlin Long, Mykhailo Petrychuk, and Svetlana Vitusevich*. Impact of Light Excitation on Liquid Gate-All-Around Silicon Nanowire Field-Effect Transistor Biosensors with Bowtie Antenna. Adv. Mater. Technol. 2024, 2400747. (DOI: 10.1002/admt.202400747)

4.Mykhailo Petrychuk, Denys Pustovyi, Nazarii Boichuk, **Yongqiang Zhang**, Hanlin Long, and Svetlana Vitusevich*. Random Telegraph Signal Noise Spectroscopy: Challenges and Opportunities for Biosensing Applications. Fluct. Noise Lett. 2024. (doi.org/10.1142/S021947752440056X)

5.**Yongqiang Zhang**, Nazarii Boichuk, Denys Pustovyi, Valeriia Chekubasheva, Hanlin Long, Mykhailo Petrychuk, and Svetlana Vitusevich*. Peculiarities of the SCLC Effect in Gate-All-Around Silicon Nanowire Field-Effect Transistor Biosensors. Adv. Electron. Mater. 2024, 2300855. (DOI: 10.1002/aelm.202300855)

6.Mykhailo Petrychuk, Denys Pustovyi, Nazarii Boichuk, **Yongqiang Zhang**, Hanlin Long, and Svetlana Vitusevich*. New Approach for Enhancing Sensitivity in Liquid-Gated Nanowire FET Biosensors Under Optical Excitation. Adv. Mater. Technol. 2024, 2301303. (DOI: 10.1002/admt.202301303)

7.**Yongqiang Zhang**, Nazarii Boichuk, Denys Pustovyi, Valeriia Chekubasheva, Hanlin Long, Mykhailo Petrychuk, and Svetlana Vitusevich*. Noise Spectroscopy Analysis of Ion Behavior in Liquid Gate-All-Around Silicon Nanowire Field-Effect Transistor. Biosensors. Adv. Mater. Interfaces 2023, 2300585. (DOI: 10.1002/admi.202300585)

8.Nazarii Boichuk, Yurii Kutovyi, Denys Pustovyi, **Yongqiang Zhang**, Volker Weihnacht, and Svetlana Vitusevich*. High Performance of Liquid-Gated Silicon Nanowire FETs Covered with Ultrathin Layers of Diamond-Like Tetrahedral Amorphous Carbon. Phys. Status Solidi A 2023, 2300024. (DOI: 10.1002/pssa.202300024)

9.Yangyan Guo, Denys Pustovyi, Yurii Kutovyi, Nazarii Boichuk, Mykhailo Petrychuk, **Yongqiang Zhang**, and Svetlana Vitusevich*. Noise Spectroscopy of Transport and Ion-Related Phenomena in Silicon Nanowire Field-Effect Transistor Biosensors. Adv. Mater. Interfaces 2022, 9, 2201142. (DOI:10.1002/admi.202201142)

Articles in conference journals

1.Denys Pustovyi, Mykhailo Petrychuk, Fujiwara Akira, **Yongqiang Zhang,** Hanlin Long, Valeriia Chekubasheva, and Svetlana Vitusevich*. Quantum Channel FETs for Advanced Biosensors. Proceedings of 27th International Conference on Noise and Fluctuations (ICNF 2025), June 17-20, Taormina, Italy. pp. 83-84.

2.**Yongqiang Zhang**, Kai Li, Nazarii Boichuk, Denys Pustovyi, Valeriia Chekubasheva, Hanlin Long, Mykhailo Petrychuk, and Svetlana Vitusevich*. Silicon Nanowire Field-Effect Transistor Biosensors with Bowtie Antenna. 2025 11th Joint EUROSOI workshop and international conference on ultimate integration on silicon (EUROSOI-ULIS) pp.78-79, (2025)

3.Mykhailo Petrychuk, Akira Fujiwara, Denys Pustovyi, **Yongqiang Zhang**, Hanlin Long, and Svetlana Vitusevich*. Optically Controlled Nanoscale FET Toward Advanced Biosensing Applications. 2023 International Conference on Noise and Fluctuations (ICNF) pp.1-4, (2023).

4.Mykhailo Petrychuk, Denys Pustovyi, Nazarii Boichuk, **Yongqiang Zhang**, and Svetlana Vitusevich*. New approach for enhancing sensitivity in nanowire FET biosensors.33rd Anniversary World Congress on Biosensors, Biosensors 2023, Busan, South Korea, 5 Jun 2023 - 8 Jun 2023.

Attended Schools & Invited talks

1. Talk at Winterschool 2022 in Hirschegg

2. Ningbo Institute of Materials Technology & Engineering, P. R. China: The 6th "Materials+" World Young Scholars Academic Forum, 2023.

3. Talk at Summer school 2024 in Aachen

4. Talk at Winter School 2025 in Hirschegg

Awards

1. China Scholarship Council (CSC) 2021-2025.